Chim, Ya Hua (2017) *Probing mechanical properties to study cancer cell migration.* PhD thesis, University of Glasgow.

https://theses.gla.ac.uk/7901/

# Probing mechanical properties to study cancer cell migration

---

**Ya Hua Chim**

A thesis submitted for the degree of

Doctor of Philosophy

School of Engineering,

College of Science and Engineering

University of Glasgow

2016

# Abstract

To best comprehend cellular behaviour and how it determines cell migration in metastatic cancer, the research described here has focused on cell mechanics. The signalling pathway involving Rho-associated kinase (ROCK) has emerged as being the main regulator for the cellular cytoskeleton and actomyosin contractility that play key roles in metastatic cancer formation. In this thesis, an examination is made of how the cellular properties intertwine as ROCK is overexpressed. In research towards being able to measure and describe the viscoelastic properties of a cell that are associated with cell mechanics, over a wide range of timescales, a novel AFM force indentation data analysis method was applied.

In particular, as part of this study, pancreatic ductal adenocarcinoma (PDAC) cells were overexpressed with ROCK, and the influence of ROCK activity on cell's elastic and viscoelastic properties were quantified. It was found that when ROCK activity was overexpressed in cells, their elasticity decreased while their viscosity remained unchanged. These properties had a direct correlation with the activity of ADF/cofilin - the proteins downstream of ROCK. This meant that with overexpression, more stable actin bundles were present along with their inward stresses generated by the actomyosin contraction. This is consistent with an increased level of compressive forces within cells. Collective compressive forces between cell-cell are associated with the packing of cells that decreases cellular response.

To further understand the role of ROCK activity in cancer invasion, a microfluidic device was created to mimic cell migration through tissue. The device consists of precisely defined microchannels with dimensions chosen to hinder and confine the cells in a manner similar to that found in a physiological environment. It was found that overexpressed ROCK1 cells in the confinement had notable decrease in cell size and motility. Along with this decrease in mechanical properties, observations also gave rise to questions about the connection between these properties that remain to be answered.

# List of publications and conferences

## Publications

- Chim YH, Tassieri M, Rath N, Olson MF, Yin H. *Probing viscoelastic properties of cells by atomic force microscope: a continuous frequency spectrum "in a step".* (submitted)
- Chim YH, Rath N, Rudzka D, Olson MF, Yin H. *Investigate the mechanical response of ROCK activity on cell migration.* (under preparation)
- Cameron JM, Gabrielsen M, Chim YH, Munro J, McGhee EJ, Sumpton D, Eaton P, Anderson KI, Yin H, Olson MF. *Polarized Cell Motility Induces Hydrogen Peroxide to Inhibit Cofilin via Cysteine Oxidation.* Current Biology; 2015;25(11):1520–11525.
- Gorman M, Chim YH, Hart A, Riehle MO, Urquhart AJ. *Poly(N-acryloylmorpholine): A simple hydrogel system for temporal and spatial control over cell adhesion.* Journal of Biomedical Material Research Part A; 2013;00A:000–000.

## Conferences

- Poster presentation, titled *Advancement in mechanobiology with atomic force microscopy.* BSR Winter Meeting 2015, Glasgow, December 2015. Awarded joint first prize.
- Poster presentation, titled *The Role of Cell Mechanics in Cancer Invasion*. CellMech2015, Barcelona, May 2015.
- Oral presentation, titled *AFM-based microrheology on individual cells.* DTC Symposium, Glasgow, March 2015.
- Oral presentation, titled *Single cell elasticity of pancreatic cancer cells: a new insight into ROCK activation.* MMC2014, Manchester, July 2014.
- Yuan X, Chim Y, Yin H. *Linking cell shape, elasticity and fate: in vitro re-differentiation of chondrocytes.* SPIE Proceedings, 2014.
- Poster presentation, titled *Mechanical properties of single cells in seeking tumour diagnostics and therapies. TCES*, Cardiff, July 2013.

# Contents

Abstract ..... i

List of publications and conferences ..... ii

- Publications ..... ii
- Conferences ..... ii

List of figures ..... vii

List of tables ..... xiii

Acknowledgements ..... xiv

Author's declaration ..... xv

Abbreviations ..... xvi

Chapter 1 Introduction ..... 1

- 1.1 Early cancer diagnostics ..... 1
- 1.2 Cellular mechanics in cancer ..... 2
  - 1.2.1 Cell structure ..... 2
  - 1.2.2 Mechanical properties of cancer cells ..... 4
- 1.3 Rho-associated protein kinase (ROCK) ..... 5
- 1.4 Review of techniques for characterising cell mechanics ..... 7
  - 1.4.1 Micropipette aspiration ..... 7
  - 1.4.2 Magnetic particle microrheology ..... 8
  - 1.4.3 Optical tweezers ..... 8
  - 1.4.4 Micro-particle stretcher in microfluidic device ..... 9
  - 1.4.5 Particle tracking microrheology ..... 10
- 1.5 Atomic force microscopy (AFM) force spectroscopy ..... 10
  - 1.5.1 Operational principle ..... 11
  - 1.5.2 Elasticity calculation ..... 13
  - 1.5.3 Applications of AFM methods to cell mechanics ..... 15

1.6 Cancer cell migration ........ 16
1.6.1 Boyden chamber ........ 16
1.6.2 Gel invasion assay ........ 17
1.6.3 3D tumour spheroid invasion assay ........ 18
1.6.4 Oris 3D embedded invasion assay ........ 18
1.6.5 Microfluidic methods ........ 19
1.7 Aims and objectives ........ 20
1.8 Thesis outline ........ 21
Chapter 2 Effect of ROCK Activation on Cell Elasticity ........ 23
2.1 Abstract ........ 23
2.2 Introduction ........ 23
2.3 Materials and Methods ........ 25
2.3.1 Materials ........ 25
2.3.2 Cell culture ........ 26
2.3.3 Atomic force spectroscopy ........ 28
2.3.4 Actin staining ........ 34
2.3.5 Statistics ........ 34
2.4 Results and Discussion ........ 35
2.4.1 Effect of overexpression of ROCK on elastic modulus ........ 35
2.4.2 Cell activation in relation to ROCK ........ 43
2.5 Conclusions ........ 50
Chapter 3 Cell Viscoelasticity ........ 51
3.1 Abstract ........ 51
3.2 Introduction ........ 52
3.3 Approaches to describe viscoelastic behaviour ........ 54
3.3.1 Spring and dashpot models ........ 56
3.3.2 Power-law models ........ 58
3.3.3 Frequency dependent stress-strain representation ........ 59

3.4 Fourier transform-AFM-microrheology .......... 60
3.5 Materials and Methods .......... 63
  3.5.1 Samples .......... 63
  3.5.2 Fabrication of cell pattern .......... 63
  3.5.3 Immunofluorescence staining .......... 65
  3.5.4 Stress relaxation .......... 65
  3.5.5 Bulk rheology .......... 67
3.6 Results and Discussion .......... 67
  3.6.1 Establishment of FT-AFM-M .......... 67
  3.6.2 Effect of cell morphology on viscoelasticity .......... 78
  3.6.3 Effect of deleted p53 gene on viscoelasticity .......... 81
  3.6.4 Effect of ROCK activation on viscoelasticity .......... 84
3.7 Conclusions .......... 87
Chapter 4 Cancer Cell Migration .......... 88
4.1 Abstract .......... 88
4.2 Introduction .......... 88
4.3 Materials and Methods .......... 91
  4.3.1 Cells .......... 91
  4.3.2 Transwell assay .......... 91
  4.3.3 Microfluidics design and fabrication .......... 92
  4.3.4 Cell loading and imaging in microfluidic device .......... 94
4.4 Results and Discussion .......... 95
  4.4.1 Invasiveness versus cell migration ability .......... 95
  4.4.2 Cell migration through microfluidic device .......... 98
4.5 Conclusions .......... 114
Chapter 5 Conclusions and Future Work .......... 116
5.1 Abstract .......... 116
5.2 Overall findings and conclusions .......... 116

5.3 Future work .......... 118

  5.3.1 Mechanical properties .......... 118

  5.3.2 Microfluidic device .......... 118

Chapter 6 References .......... 120

## List of figures

Figure 1.1│Schematic diagram of a typical eukaryotic cell with its subcellular elements. 2
Figure 1.2│Schematic diagram of (A) active and inactive ROCK with its structure and (B) a collective of ROCK signalling to promote actomyosin contractile force generation along with Rac signalling to promote actin dynamics. 6
Figure 1.3│Schematic diagram of the set-up for atomic force microscope (AFM), highlighting spherical probe indentation on a cell. 11
Figure 1.4│Typical force-distance curve on a cell computed out from AFM NanoWizard II (JPK Instruments). 12
Figure 1.5│Sketch of the cantilever probes. 14
Figure 2.1│A schematic diagram of the ROCK signalling pathway once activated. 24
Figure 2.2│ The effect of pH change according to the HEPES concentration in DMEM media, over 8 hours. The highest concentration of HEPES gave the lowest pH value for a longer period of time, and vice versa for low concentrations. 30
Figure 2.3│ Analysed force-indentation result off cell measurement, using our in-house made algorithm. 33
Figure 2.4│Images of QKR:ER and QKK:ER cells in the absence and presence of estrogen (4HT) treatment. All scale bars are 30 μm. 36
Figure 2.5│Elasticity change of QKR:ER relative to QKK:ER following 4HT treatment (n = 80 cells), expressed as mean ± SD. QKR:ER +4HT became softer in reference to the QKR:ER-4HT and QKK:ER+4HT ($p < 0.0001$). 37
Figure 2.6│Images of modified PDAC p53 fl cells in the absence and presence of estrogen (4HT) treatment. All scale bars are 30 μm. 38
Figure 2.7│Elasticity change of ROCK1:ER and ROCK2:ER relative to EGFP:ER following 4HT treatment (n = 80 cells), expressed as mean ± SD. Both ROCK1:ER and ROCK2:ER cells were softer in reference to the EGFP:ER cells ($p<0.0001$). 39

Figure 2.8│Comparison between untreated ROCK1:ER cells grown independently or in clusters. Cells in (A) clusters or are (B) isolated. All scale bars are 30 µm. (C) Representative force-indentation approach curves of cells in condition (A) and (B). (D) Box and whiskers plot of elasticity values measured from clustered and isolated cells. n=17 (p= ns; non-significant). .......... 41

Figure 2.9│Comparison between the actin filaments of modified PDAC cells in the presence and absence of 4HT treatment. The fluorescent cells showing nucleus (blue) and F-actin (green). All scale bars are 50 µm. Red arrows indicate dense actin bundles. Overexpression of ROCK led to fewer bundles of stress fibres, and none at the centre of the cell compared to the control. .......... 42

Figure 2.10│Average elasticity measurements of PDAC p53 fl ROCK1:ER: mcherry; control, and cofilin cells (n = 80 cells), expressed as mean ± SD. All scale bars are 30 µm. Cofilin activated cells presented to be significantly stiffer compared to the control ($p < 0.0001$). .......... 44

Figure 2.11│Average elasticity measurements of PDAC p53 fl+ ROCK1:ER relative to GFP:ER following 4HT and BMS-5 treatment (n = 80 cells), expressed as mean ± SD. Although activated ROCK1:ER cells were softer compared to EGFP:ER ($p < 0.0001$), the cells returned to its original stiffness with LIM kinase inhibitor. .......... 46

Figure 2.12│Average elasticity measurements of PDAC p53 fl+ ROCK1:ER MLC and counterpart MLC AA cells following 4HT or ethanol treatment (n = 80 cells), expressed as mean ± SD. MLC on overexpressed ROCK1 caused an increase in stiffness though similar effect was seen in ethanol and MLC AA cells ($p < 0.0001$). .......... 47

Figure 2.13│Fluorescent image of PDAC p53 fl+ mcherry MLC and MLC AA cells showing the amount of expressed mcherry. Scale bar showing 100 µm. The red arrows indicating the mcherry expressed. .......... 48

Figure 2.14│The comparison between PDAC p53 fl+ ROCK1:ER relative to EGFP:ER cells in the presence of blebbistatin treatment. All scale bars are 30 µm. The graph was expressed as mean ± SD from 80 cells. Both EGFP:ER and ROCK1:ER cells exhibited decrease in elasticity with blebbistatin treatment ($p < 0.0001$). .......... 49

Figure 3.1│Sketches of the spring and dashpot models. .......... 57

Figure 3.2│Schematic diagram of the experimental procedure carried out for FT-AFM-M. .......... 66

Figure 3.3│Front panel of the Labview (National Instruments) algorithm that implements the analytical method to calculate the Fourier transforms of both measured force and indentation functions in Equation 3.19. .......... 68

Figure 3.4│Viscoelastic properties of 30 kPa complex gel analysed with Labview program from initial approach segment. At the high-end frequencies, a lot of noise present in the data, which made it difficult to establish *G'* (white) and *G''* (red). .......... 69

Figure 3.5│The effect of indenter diameter on the viscoelastic properties of 20:1 PDMS at a loading rate of 3 μm/s (n = 9 measurements), expressed as mean ± SD. The frequency sweeps below 10 Hz showed that there were differences in *G'* between 4.74 μm/ 10 μm and 20 μm probe geometries ($p < 0.04$), though *G''* did not change. .......... 70

Figure 3.6│Various approach ramp speeds applied to gels. The stress relaxation curves for (A) 30 kPa and (C) 100 kPa gels showed that speeds > 70 μm/s the force overshot, otherwise no difference. The frequency sweep for (B) 30 kPa and (D) 100 kPa gels displayed speeds > 70 μm/s, *G'* and *G''* were lower compared to other speeds. .......... 71

Figure 3.7│Overlay rheology measurements from compact rheometer against FT-AFM-M for a range of materials; (A) 30 kPa gel, (B) 100 kPa gel, (C) multi-purpose tac and (D) 20:1 PDMS. The measurements obtained from both techniques were in good agreement with each other, on both *G'* and *G''*. .......... 73

Figure 3.8│Comparison between the short-relaxation and long-relaxation carried out on PDAC p53 R172H cells (n = 50 cells), expressed as mean ± SD. The cells' viscoelasticity was measured with (A) t = 1 s and (B) t = 30 s holding times. Both relaxations displayed similar trends in (C) *G'* and (D) *G''* properties. .......... 75

Figure 3.9│Young's modulus measured using the common AFM indentation method and the new FT-AFM-M method on PDAC p53 R172H at $f$ = 2400 Hz (n = 50 cells). A good agreement with the two methods; the points lying within y = x line of best fit. .......... 77

Figure 3.10│Fluorescent images of PDAC p53 R172H cells cultured on different surfaces, stained for F-actin (green) and DAPI (blue). The cells were presented in (a) pattern; t = 4 hours, (b) non-pattern; t = 4 hours, and (c) non-pattern; t > 18 hours. All scale bars are 50 μm. 78

Figure 3.11│Frequency sweep of the PDAC p53 R172H cells cultured on different surfaces (n = 50 cells), expressed as mean ± SD. Cells (t = 4 hours) on pattern and non-pattern surfaces were displayed as (A) *G'* and (B) *G"*. At high-end frequencies, the non-patterned cells were softer and fluid-like compared to patterned cells ($p < 0.04$), whilst at low frequencies, both cells exhibit similar properties. Cells on pattern (t = 4 hours) and non-pattern (t > 18 hours) surfaces were displayed as (C) *G'* and (D) *G"*. For t > 18 hours, the non-patterned cells were stiffer and more liquid-like than patterned cells ($p < 0.0001$). 80

Figure 3.12│Comparison between the cell morphology of PDAC p53 R172H and PDAC p53 fl cells. The cells were stained with DAPI to show nucleus (blue) and phalloidin to show F-actin (green). All scale bars are 30 μm. 82

Figure 3.13│Stress relaxation carried out on PDAC mutant p53 and deleted p53 cells (n = 50 cells), expressed as mean ± SD. Frequency sweeps of (A) *G'* and (B) *G"*. Over the frequency range, mutant p53 cells displayed stiffer properties compared to deleted p53 cells ($p < 0.01$), while their fluid-like properties remained the same. 83

Figure 3.14│H&E-stained sections of modified PDAC cells with 4HT treatment cultured on organotypic matrix (8 days) and their cell morphologies. Activated ROCK cells displayed its invasiveness through the matrix whilst the control cells remain on the surface. All scale bars are 100 μm. (Data obtained from Dr. Nicola Rath) 84

Figure 3.15│Frequency sweep of the modified PDAC cells following +/- 4HT treatment (n = 50 cells), expressed as mean ± SD. Over the frequency range, treated ROCK1:ER and ROCK2:ER cells were more compliant relative to EGFP:ER cells ($p < 0.0001$), while their viscous properties were unchanged. 85

Figure 4.1│Schematic drawing of (A) the microfluidic device, (B) plane view of tapered and abrupt channel openings, and (C) the side profiles of the symmetric and asymmetric narrow channels. (D) A table outlined to show the dimensions of the confined channels and including the total area in which cell migrate through. 92

Figure 4.2│Percentage of migrated cells (PDAC mutant p53 and deleted p53) passed through various pore sizes. Images displayed of (A) mutant p53 and (B) deleted p53 cells on 8 µm transwell. All scale bars are 50 µm. (C) Percentage of migrated of both cells on 3, 5, and 8 µm transwell (n = 6 wells), expressed as mean ± SD. Less migration was observed with deleted p53 cells compared to its counterpart at 8 µm pore ($p < 0.0001$), though no difference in 3 µm and 5 µm pore sizes. .................................... 96

Figure 4.3│Percentage of migrated cells (EGFP:ER and ROCK1:ER) passed through various pore sizes (n = 6 wells), expressed as mean ± SD. There was a significant decrease in number of migrated cells when ROCK1 activity was overexpressed, though these were also view in the control. ........................................................................................................ 97

Figure 4.4│Chemical gradient established over a 4 µm microchannel of various heights using fluorescein and PBS, over 10 hours. The heights of the microchannels include (A) 5 µm, (B) 8 µm and (C) 15 µm. ............... 99

Figure 4.5│Time-lapse images of PDAC mutant p53 cells travelling through 3 µm x 15 µm microchannels, over 5 hours. Red arrows indicate the movement of cells through the channel. Cells passed through (A) tapered and (B) abrupt openings. .......................................................... 100

Figure 4.6│Effect acquired extended length measurements carried out on large and small cross sectional microchannels at different times (n = 3 devices), expressed as mean ± SD. Two type of cells used; (A) PDAC mutant p53 and (B) deleted p53 cell. Although the measurements for different times were insignificant, a decrease in cross sectional area increases the extended lengths. .......................................................... 101

Figure 4.7│Comparison between PDAC mutant p53 and deleted p53 cells moving into tapered (T) and abrupt (R) channel openings in 5 µm (A) and 15µm (B) height channels with three different channel widths (i.e. 3, 4, and 5 µm), expressed as mean ± SD from n = 3 devices. On average there are less deleted p53 cells occupied in the microchannel as oppose to its counterpart. No significant difference between the two channel openings against cells. ...................................................................... 102

Figure 4.8│Comparison between channel openings and extended lengths (PDACs) generated within the channel (n = 3 devices), expressed as mean ± SD. No statistical difference between channel openings and cell length in (A & B) 5 μm and (C & D) 8 μm heights, though there were difference shown in channel widths. The cells used were (A & C) PDAC mutant p53 and (B & D) deleted p53 cells. ............................................. 103

Figure 4.9│Comparison between channel openings and the cell lengths (PDACs) generated within the channel (n = 3 devices), expressed as mean ± SD. No statistical difference between channel openings, and widths on cell velocity in (A & B) 5 μm and (C & D) 8 μm heights. The cells used were (A & C) PDAC mutant p53 and (B & D) deleted p53 cells. 105

Figure 4.10│Comparison between cell occupancy (PDAC p53 cells) in microchannels against its cross sectional area (n = 3 devices), expressed as mean ± SD. A gradual decrease in cell occupancy as channels gets narrower ($p < 0.004$ for deleted p53 and $p < 0.01$ for mutant p53 cells). The mutant p53 cells tend to migrate into the narrow channels more than its counterpart cells. ........................................................................... 107

Figure 4.11│ Comparison between cell length (PDAC p53 cells) in microchannels against its cross sectional area (n = 3 devices), expressed as mean ± SD. A gradual increase in cell lengths with decrease channel size. The mutant p53 cells tend to elongate along the narrow channels more than deleted p53 cells. ..................................................................... 108

Figure 4.12│ Comparison between migration velocity of PDAC p53 cells in microchannels against its cross sectional area (n = 3 devices), expressed as mean ± SD. No statistical difference between migration velocity and the channel size, in both cell lines. ......................................................... 109

Figure 4.13││Comparison between EGFP:ER and ROCK1:ER in relation to cell occupancy within a microchannel following estrogen treatment (n = 3 devices), expressed as mean ± SD. No significant difference between numbers of cells entered into the microchannels and treatment to cells. . 111

Figure 4.14│ Comparison between EGFP:ER and ROCK1:ER in relation to cell lengths within a microchannel following estrogen treatment (n = 3 devices), expressed as mean ± SD. A reduction in cell length in both EGFP:ER and ROCK:ER cells following treatment ($p < 0.0001$). ............. 112

Figure 4.15│ Comparison between EGFP:ER and ROCK1:ER in relation to migration velocity within a microchannel following estrogen treatment (n = 3 devices), expressed as mean ± SD. Overexpression of ROCK1 activity displayed a decrease in migration velocities ($p < 0.01$). ............... 114

# List of tables

Table 3.1│A list of symbols with their definitions. 54

Table 3.2│A table to display *G’* values of ROCK activated and inactivated cells at low, mid-range and high frequencies and their differences relative to the control (%). The values in the brackets display the percentage of reduction relative to the control and inactivated cells. 86

Table 4.1│A table outlining the pre-bake, exposure, and post-bake parameters used to achieve optimal thickness. 93

Table 4.2│A table outlining the calculated chemical gradient for each channel dimension. 100

# Acknowledgements

Firstly, I would like to thank my first supervisor Dr Huabing Yin for the technical guidance and support throughout the process. I would also like to thank my co-supervisor Prof. Michael Olson for informative discussions on the biology aspect and Dr. Manlio Tassieri on the microrheology aspect of the studies.

I want to extend my acknowledgements to all the research colleagues who got involved in any aspects of this work, either at the Biomedical Engineering department or the Beatsons Institute (R17 group), namely: Dr. Xiaofei Yuan, Dr. David McIlvenna, Dr. David Paterson, Dr. Jenifer Cameron, and Dr. June Munro.

Great appreciation to James Watt Nanofabrication Centre (JWNC) for their excellent facilities, so I could fabricate my microfluidic devices, and to Beatsons Institute for Cancer Research for providing me with the resources for my studies.

Many thanks to Ellie Pulleine for teaching me AFM and Dr. Rab Wilson for teaching me photolithography of which I had no prior knowledge. Thank you to Dr. Nicola Rath providing the experimental data shown in Figure 3.14, and for transfecting the cells along with Dominika Rudzka.

Special thanks go to Dr Andrew Glidle for invaluable assistance throughout the duration of the project, and Dr. Julien Reboud, for his help and contribution with my work and preparation for conferences.

I would like to thank the Engineering and Physical Sciences Research Council for the funding with which this thesis study was possible.

Thanks to my friends, namely Niall and Laura Geoghegan, Louisa Lee, and Doaa Kredi whom helped me to escape from my bubble, of just home and the research lab. Also, friends from Manchester, whom have put up with my rants about the research work, and were there when I needed them the most.

Thanks to Damon Lazos for putting up with me during the emotional and stressful times.

Finally, most importantly, thanks to my parents and siblings for their moral support during my studies.

# Author’s declaration

The author declares that the work conducted in this thesis is the result of their own work and has not previously been submitted for a degree at University of Glasgow or any other institution.

# Abbreviations

| | |
|---|---|
| ADF | Actin depolymerising factor |
| AFM | Atomic force microscope |
| ATP | Adenosine triphosphate |
| a.u. | Arbitrary unit |
| BPE | Bovine pituitary extract |
| BSA | Bovine serum albumin |
| Cdc42 | Cell division control protein 42 homolog |
| CFL1 | Cofilin 1 |
| $CO_2$ | Carbon dioxide |
| CP | Contact point |
| CRD | Cystein-rich domain |
| CRFM | Contact resonance force mode |
| DMEM | Dulbecco’s modified Eagle medium |
| DMT | Derjaguin-Müller-Toporov |
| $E$ | Young’s Modulus |
| EDTA | Ethylenediaminetetraacetic acid |
| EGFP:ER | Enhanced green fluorescent-estrogen receptor fusion protein |
| ER | Hormone binding domain of the estrogen receptor |
| $F$ | Indentation force |
| FA | Focal adhesion |
| F-actin | Filamentous actin |
| FBS | Foetal bovine serum |
| FMM | Force modulation mode |
| FT-AFM-M | Fourier transform-AFM-microrheology |
| $G'$ | Storage modulus |
| $G''$ | Loss modulus |
| GA-1000 | Gentamicin sulphate and amphotericin-B |
| GDP | Guanosine diphosphate |
| G-actin | Globular actin |
| GTP | Guanosine triphosphate |
| HEPES | 4-(2-hydroxyethyl)-1-piperazineethanesulfonic acid |
| IPA | Isopropyl alcohol |

| | |
|---|---|
| JKR | Johnson-Kendall-Roberts |
| $K^+$ | Potassium ion |
| K14 | Keratin 14 |
| KBM-2 | Keratinocyte growth medium |
| KD:ER | Kinase-dead ROCKII-estrogen receptor fusion protein |
| KGM | Keratinocyte growth medium |
| LIM kinases 1/ 2 | LIMK1/ 2 |
| $Mg^{2+}$ | Magnesium ion |
| MLC | Myosin regulatory light chain |
| MLC AA | Non-phosphorylated MLC protein |
| MTC | Magnetic twisting cytometry |
| MYPT1 | Myosin binding subunit |
| $Na^+$ | Sodium ion |
| PBS | Phosphate buffered saline |
| PDAC | Pancreatic ductal adenocarcinoma |
| PDMS | Polydimethylsiloxane |
| PH | Pleckstrin homology |
| PDAC p53 R172H | PDAC mutant p53 |
| PDAC p53 fl | PDAC deleted p53 |
| QKK | Genetically modified mice expressing K14-KD:ER |
| QKR | Genetically modified mice expressing K14-ROCK:ER |
| PBS | Phosphate buffered saline |
| PEG | Polyethylene glycol |
| $R$ | Radius of the probe |
| RBD | Rho-binding domain |
| ROCK | Rho-associated kinase |
| ROCK:ER | Conditionally active ROCK-estrogen receptor fusion protein |
| $\upsilon$ | Poisson ratio |
| SD | Standard Deviation |
| Si | Silicon |
| SLS | Standard linear solid |
| UV | Ultraviolet light |
| 3D | Three-dimensional |
| 4HT | (Z)-4-Hydroxytamoxifen |
| $\alpha$ | Half opening angle of the tip for conical indentation |
| $\delta$ | Indentation depth |

# Chapter 1 Introduction

## 1.1 Early cancer diagnostics

Cancer is one of the leading causes of morbidity and mortality worldwide. It has been estimated that, globally, there were approximately 8.2 million cancer related deaths in 2012 (B. W. Stewart and C. P. Wild, 2014). Therefore, there has been a global action plan to reduce the mortality from cancer by extensive research in both science and medicine. To improve understanding of the disease condition and progression, active fields of research include cancer metabolism, growth, survival, invasion and metastasis.

A definition of cancer is a disease that causes normal cells to change and grow in an uncontrollable manner before spreading to other parts of the body (B. W. Stewart and C. P. Wild, 2014). These abnormal cells keep doubling until a lump (tumour) is formed. Tumours are complex masses that are made up of billions of copies of the original cancerous cell. In some cases, modifying the genetics and gene expression (epigenetics) of a cell can cause various functions such as growth, motility, metabolism, communication (signalling), and cell remodelling (Ben-Ze'ev, 1985) to change. These alterations within a cell could contribute to tumour formation.

Traditional methods to detect cancerous cells include palpation, visual identification of malignant changes, cell proliferation analysis, specific ligand-receptor labeling, or genetic testing (Huang and Ingber, 2005; Iyer et al., 2009). These methods are known to be either insufficiently accurate or require lengthy and complicated analysis. There have also been investigations into alternative methods to detect cancer that use traditional methods as their basis (Iyer et al., 2009; Lekka et al., 2012). For instance, it has been shown that elevated tissue stiffness is associated to tumour development (Samuel et al., 2011), though it is unclear how the mechanical properties of individual cells may contribute both to tissue stiffening and their physiological significance in tumour development.

## 1.2 Cellular mechanics in cancer

### 1.2.1 Cell structure

Living cells are complex organisms due to their dynamic nature and constant change in shape and structure. They consist of many varying components, all having different roles contributing to maintaining the cell in a state of equilibrium. A eukaryotic cell is constantly being stabilised by the cellular skeleton (cytoskeleton), which is made up of three elements: actin filaments, microtubules and intermediate filaments (Suresh, 2007) (Figure 1.1). These biopolymers play an important role in retaining the cell shape, cell migration, rigidity, and cell division. Hence, the concentration and molecular state of all the macromolecular and polymeric biomolecules will determine the mechanical deformation characteristics of an individual cell (Zhu et al., 2000). Below, we will discuss several of the biopolymers and their relevance to cellular behaviour.

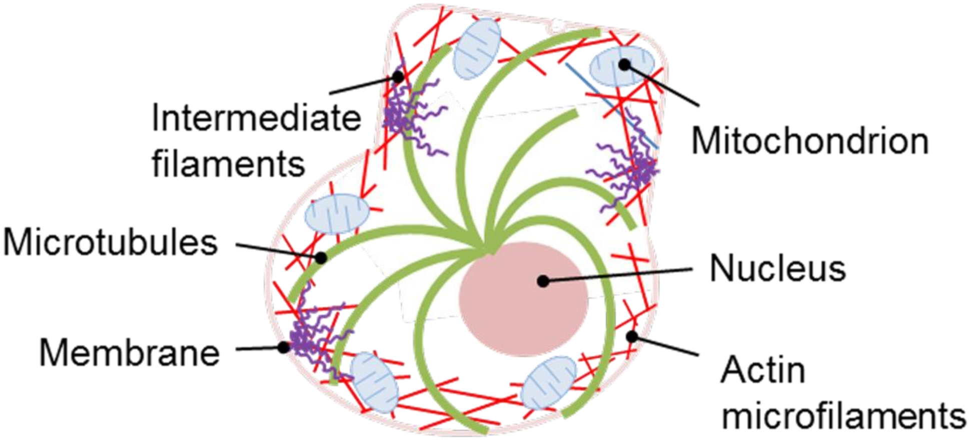

**Figure 1.1│Schematic diagram of a typical eukaryotic cell with its subcellular elements.**

Actin filaments (filamentous actin; F-actin) are formed by polymerisation of actin monomers (globular actin; G-actin). These biopolymers are the most abundant protein in most eukaryotes (typically 5–10% of total protein), with a helical cable-like structure (having a diameter of about 7 nm and up to several micrometres in length) (Cooper, 2000). These filaments can be arranged into two general types of structure, known as actin bundles and actin networks. In bundles, the actin filaments are crosslinked into parallel arrays, which are found to support the projections of the plasma membrane. These bundles are also known as stress fibres. In network, the filaments are loosely crosslinked in orthogonal arrays to form networks, which are localised at the periphery of a cell; beneath the plasma membrane. The formation of these structures is determined by a variety of actin-binding proteins (e.g. fimbrin, α-actinin and filamin) that crosslink actin filaments. This process is reversible, though the presence of certain ions ($Mg^{2+}$, $K^{+}$, $Na^{+}$) reduces the likelihood of polymerisation of actin monomers (Suresh, 2007). However, if the cell requires additional strength in response to an increase in stress, actin stress fibres tend to be formed. These fibres will be attached and localised at the focal adhesions. Actin filaments are highly associated with cell migration forming filopodia and lamellipodia as the initial step, with an interaction with myosin leading to actomyosin contractions that aid movement.

Microtubules are formed from a globular protein known as tubulin, two types of which are the polypeptide families, α-tubulin and β tubulin. These polypeptides string together, to form long strands of protofilaments. When thirteen parallel protofilaments come together, they can form hollow rod structures, with a diameter of ~25 nm (Cooper, 2000). Microtubules are polar structures and so the direction of movement is pre-determined. The negative end of these structures is anchored in the centrosome (microtubule-organising centre) at one end, and the tubule can extend outward toward the cell periphery at the other. In most cells, the centrosome is located near the nucleus. The microtubules are under constant assemble and disassemble at each end. This coexistence is known as dynamic instability, which can be regulated by the rate of GTP (guanosine triphosphate) hydrolysis. Indications are that microtubules are the most rigid of the three cytoskeletal biopolymers: When mechanically coupled with the surrounding cytoskeleton, microtubules have been shown to withstand large compression forces (Brangwynne et al., 2006). This suggests that microtubules could provide a structural contribution towards a cell's mechanical behaviour. Microtubules have been shown to play an important role in mitosis (cell division) with the formation of mitotic spindles and cell migration, with the internal structure of cilia and flagella made of this biopolymer. Research has also found that there are certain binding agents that inhibit the formation of microtubules, thus inhibiting mitosis (Suresh, 2007).

Intermediate filaments are made up of more than 50 different intermediate filament proteins that can be categorised into six groups: acidic keratin, neutral/basic vimentin, neurofilament proteins, nuclear lamins and nestin (Cooper, 2000). The filaments are collected from about eight protofilamemts that assemble together and form a rope-like structure, with a diameter of about 10 nm. Unlike actin filaments and microtubules that are both polar, having distinct positive and negative ends, intermediate filaments do not have this degree of polarisation. An intermediate filament network is formed in the cytoplasm of most cells, extending from the nucleus to the plasma membrane. These filaments commonly work alongside microtubules, to provide strength and support to fragile tubulin structures. Although there are intermediate filaments in each cell, each have specific functions. For instance keratin filaments in epithelial cells are tightly anchored to the plasma membrane at junction between cell-cell contact (demosomes) and junction between cell-extracellular matrix (hemidemosomes) (Suresh, 2007). When there are two anchors either side of a cell, they will provide a mechanical link between the nearby cells, and provide overall mechanical rigidity. Another instance of a specific function is the vimentin intermediates filaments that provide mechanical strength to fibroblast and endothelial cells.

### 1.2.2 Mechanical properties of cancer cells

The role of cellular signalling pathways and mechanics are said to be interdependent sources that lead to cancer (Katira et al., 2013). The signalling pathways that control cell proliferation and apoptosis can cause mutation in genes, which would activate or overexpress key proteins that would lead to transformation of cells. We will discuss a particular signalling pathway in the next section. Meanwhile specific changes to the mechanical behaviour of cells as a consequence of their physiological environment can also be observed. For example, it has been noticed that a mechanical change between healthy and cancerous cells was their reduced stiffness; this was shown for bladder, breast, colon, prostate, melanoma, and brain cancer cells (and so on) (Guo et al., 2014; Khan and Vanapalli, 2013; Lekka et al., 2012; Li et al., 2008). A further mechanical property difference that has been seen is the reduced viscous nature of ovarian cancer cells (Ketene et al., 2012). Hence, it has been suggested that stiffness differences between normal and cancer cells could be employed as a diagnostic tool (Kumar and Weaver, 2009).

The transformation of healthy cells into cancerous cells is associated with a change in internal and external environments (Yallapu et al., 2015). Internally, the cytoskeleton governs the mechanical properties, which we have discussed above. In addition to the discussion above, it has been shown that there was an increase in actomyosin contractions within cancerous cells compared to healthy cells (Jonas et al., 2011; Kraning-Rush et al., 2012). There are other internal organelles that have been suggested as being associated with the transformation of cells, including nucleus size organisation or condensation of complex macromolecules (i.e. DNA, RNA and proteins), and epithelial mesenchymal transitions (Yallapu et al., 2015). Changes in the external environment can involve cell's ability to bind to neighbouring cells or to the extracellular matrix. It has been shown that modifying specific adhesion proteins can affect proliferation and invasiveness of a cell (Paredes et al., 2005; Ribeiro et al., 2010). Furthermore, increasing of the extracellular matrix stiffness has been proven to lead to an increase the metastatic potential of cells (Gartland et al.)

## 1.3 Rho-associated protein kinase (ROCK)

Rho-associated kinase (ROCK) signalling has been extensively researched in cancer, particularly in relation to tumour cell motility and metastasis (Rath and Olson, 2012). ROCK is a downstream effector protein from the Rho GTPase family. The Rho GTPase family includes RhoA, Rac1 and Cdc42, which are well known in regulation of the actin cytoskeleton organisation (Hall, 2009). Each member acts on different region of actin filament in a cell: RhoA is associated with stress fibres, Rac1 is associated with lamellipodia, and cdc42 is associated with filopodia. RhoA proteins are downstream signal transducing proteins that play roles in various cellular processes such as gene expression, cell proliferation, migration and apoptosis (Boureux et al., 2007). ROCK was the first effector of RhoA to be discovered. There are two ROCK isoforms (ROCK1 and ROCK2) that have been identified. Although there are two forms, it has been noted that the progenitor form is probably ROCK2 (Rath and Olson, 2012).

The two forms of ROCK can be situated in different regions of the cell, and so although their signalling pathways are the same, it is possible the main functions are different. ROCK1 has been shown to be diffusely located around the nucleus with stress fibres, whereas ROCK2 has been located both at the periphery of the cell as well as being around the nucleus (Yoneda et al., 2005). In addition, it has been shown that ROCK1 is important for the formation of stress fibres and focal adhesions, while ROCK2 is associated with myosin II-dependent phagocytosis (ingestion of material).

The structure of ROCK comprises a kinase domain followed by a coiled-coil region with a Rho-binding domain (RBD) and Pleckstrin homology (PH) with an internal cystein-rich domain (CRD). In an inactivated state, the ROCK structure is coiled into an auto-inhibitory ring (Figure 1.2A). Once activated by GTP-RhoA, it can promote the generation of actomyosin contractile force, through mediating phosphorylation of some downstream proteins. These proteins included myosin light chain LIM kinases 1 and 2 (LIMK1 and LIMK2), the myosin regulatory light chain (MLC), and the myosin binding subunit (MYPT1) (Rath and Olson, 2012) (Figure 1.2B).

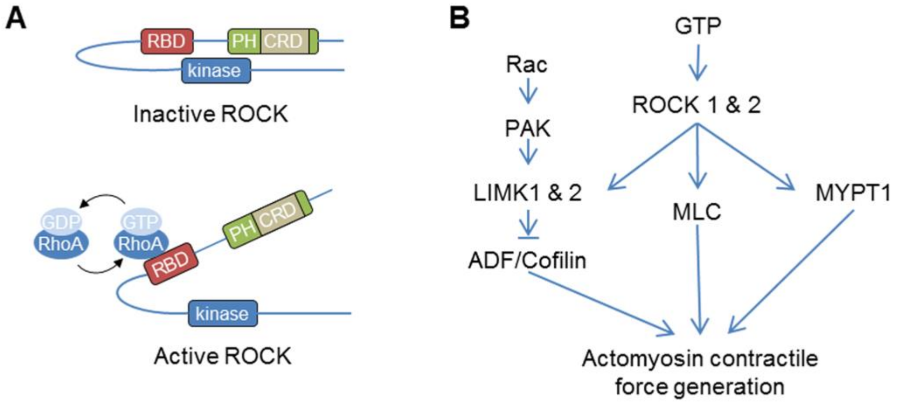

**Figure 1.2│Schematic diagram of (A) active and inactive ROCK with its structure and (B) a collective of ROCK signalling to promote actomyosin contractile force generation along with Rac signalling to promote actin dynamics.**

Many of the proteins phosphorylated by ROCKs regulate the amount of actin filaments present and the cellular contractility, thus a regulator of morphology and motility (Riento and Ridley, 2003). ROCK stabilises actin filaments in two ways: LIMK phosphorylation that phosphorylates ADF (actin depolymerising factor)/ cofilin that leads to inactivation of actin-depolymerisation activity, and MLC phosphorylation that increases actin filaments and myosin-driven contraction.

For cell migration, Rac signalling regulates the actin polymerisation to form the leading edge of a cell (lamellipodia) (Zhang et al., 2011a). This involves the downstream protein, PAK that in turn phosphorylates LIMK1 and 2, and inactivates cofilin. Therefore stable and formation of actin filaments.

## 1.4 Review of techniques for characterising cell mechanics

There have been various techniques developed to measure the mechanical properties of a single cell. These can be divided into two broad categories: active and passive, when considering the modes under which cell mechanics are measured. An active method is when an applied force used to deform a cell to indicate stiffness, elastic or viscoelastic properties, whereas a passive method senses the force generated by the cell as a consequence of its tensile stress (Addae-Mensah and Wikswo, 2008). Results from passive methods generally depend on the substrates used for measurements, which is not ideal for studies of sensitive cells. Within this sub-section we have mainly focused on the literature for active methods, describing the basic principle of each procedure and their advantages and limitations. Note, the use of an atomic force microscope to measure cell mechanics will be discussed in a separate section in further detail.

### 1.4.1 Micropipette aspiration

Micropipette aspiration (MA) was first developed by Mitchison and Swann, to study the mechanism of cell division of sea-urchin eggs by acquiring the elastic properties (Mitchison and Swann, 1954). This method can be described when a cell is deformed by a gentle suction from a micropipette when in contact with its surface. The change in cell geometry combined with the applied known pressure can then be used to calculate the force and thus the mechanical properties of a cell. The typical range of controlled suction pressure is 100–10000 Pa with a typical force range of 1–100 nN (Kamm et al., 2010). This procedure has been applied to range of cells such as: red blood cells, to look at the redistribution of cytoskeletal proteins (Discher et al., 1994); erythrocyte membranes, to observe the viscoelastic properties of the two phases of membrane (Chien et al., 1978); human leukocytes, to detect the shear modulus of applied fast and slow motion (Schmid-Schönbein et al., 1981); and normal/ osteoarthritic chondrocytes, to compare the difference between the two Young’s moduli (Alexopoulos et al., 2003; Jones et al., 1999). Furthermore, the technique has been used to study cell-cell interactions by taking two micropipettes both with a cell attached to the ends (Chu et al., 2004). The advantages of this technique are that it can be useful when studying relatively homogeneous structures, it can provide highly reproducible measurements, and it can exert a well-defined pressure to a specific localised region on the cell membrane (Oh et al., 2012). However, cells can also get aspirated too far into the pipette causing large deformations (ratio of pipette and sample), and thus the interpretation of the experiments is not always straight forward (Pravincumar et al., 2012).

### 1.4.2 Magnetic particle microrheology

Magnetic particle microrheology was first demonstrated to observe the magnetic motion of drag, twist and prodding within the cytoplasm of chick fibroblasts (Crick and Hughes, 1950). The procedure involves attachment of magnetic beads onto the cell's surface and subject them to magnetic force (Kamm et al., 2010). These beads can either generate a torque to twist on the beads (known as magnetic twisting cytometry; MTC) or generate a linear force to pull the beads (known as magnetic tweezers). The mechanical properties of a sample can be measured by either studying the magnetic field change during deformation, or particle-tracking the motion of the attached bead. These procedures have been used on biological samples such as the actin network to look at local viscoelastic properties (Ziemann et al., 1994), mouse macrophages to observe the shear modulus of the surface (Bausch et al., 1999), and endothelial cells to understand the relationship between cytoskeletal stiffness and the applied stress (Wang et al., 1993). Although the typical force generated by MTC (0.01–1 nN) and magnetic tweezers (0.1–10 nN) are ideal for detecting the mechanical properties of cells, there are a lot of disadvantages regarding these methods. To highlight a few: it is difficult to control where the magnetic beads are attached on to a cell, the depth in which the bead is embedded and keeping the bead magnetised for a long period of time is also difficult.

### 1.4.3 Optical tweezers

Optical tweezers are similar to magnetic tweezers, as both techniques attach microscopic beads to the biological substrate then apply a controlled force to determine the mechanical properties. Instead of applying a magnetic force, optical tweezers uses an optical force that is generated by a high powered laser beam. This was first developed by Arthur Ashkin, who studied micro-sized particles for trapping and acceleration (Ashkin, 1970). This procedure consisted of two beads, each of high refractive index allowing precise control of the bead in all directions. This leads to a force that can deform the sample. Optical tweezers have been used with human erythrocytes to look at the difference between discotic and nearly spherical swollen cells (Dao et al., 2003; Hénon et al., 1999), and *Escherichia* coli cells to trap and measure their rotational movement (Neuman et al., 1999). The advantages of this system are that multiple cells can be measured at once by the use of multiple beads, and that it provides high precision forces of a range typically between 1–500 pN (Kamm et al., 2010). However, as the typical forces are low, higher laser powers are required if a larger force is needed to probe stiffer samples. The use of a higher powered laser ultimately kills biological samples by overheating them. Furthermore, even long exposure to regular wavelength and power of lasers can cause photo-induced damage.

### 1.4.4 Micro-particle stretcher in microfluidic device

Microparticles such as cells, in microfluidic devices can be stretched either optically or hydro-dynamically (Gossett et al., 2012; Guck et al., 2005). Optical stretcher is an adaptation of optical tweezer, rather than using a single laser beam trap, it uses two beams; to trap and deform microparticles. There has studies on red blood cells and epithelial cells using the optical stretcher (Guck et al., 2005; Sraj et al., 2010). The limitations of this process are similar to the optical tweezers, and that it operates at a low-throughput; though faster than individual probing of cells (i.e. AFM). Recently, it has been discovered by using hydrodynamic stretching of cells in a microfluidic device, one can collect high-throughput mechanical data (Gossett et al., 2012). Approximately 2000 cell/ s of mechanical data can be collected; from flowing cells into a uniform increased hydrodynamic stresses that deform the cells. A high-speed camera was used to record the cell before and after deformation. In my opinion, the only concern with this procedure is the analysis algorithm, whether irregular cells can be tracked.

### 1.4.5 Particle tracking microrheology

Although particle tracking is not an active method as it does not apply an external force to the sample, we discuss this technique here as it can measure viscoelastic properties that can be compared alongside the above techniques. Particle tracking microrheology was first developed by *Mason et al*, to measure the linear viscoelastic shear moduli of polyethylene oxide (Mason et al., 1997). This was later used to measure semi-flexible polymers such as actin filaments (Xu et al., 1998), and more recently to measure the viscosity of the cytoplasm (Wirtz, 2009). The procedure entails tracking the movement of beads that are embedded in a viscous liquid, under an optical microscope. The beads are usually smaller than 1 µm, so they can undergo random motion due to the negligible inertial forces (gravity). This means that there are two forces acting on the bead within the viscous fluid: small random forces from the random bombardment of water molecules and movement of the fibrous network, and a frictional force from the movement of the beads. As the inertial forces are neglected and the beads are in random motion, the two forces sum to zero. By taking into account that the random motion was generated by thermal energy and there is diffusion from the bead, the viscosity of the viscous fluid can be determined. For these measurements, it has been shown that not only can the beads be suspended in a viscous fluid (Lau et al., 2003), but they can also be located on the surface of the biological sample (Shin and Athanasiou, 1999). This technique can thus be applied to analyse the beads in MTC/ magnetic tweezers and optical tweezers experiments. The advantages of this procedure include ability to measure heterogeneous samples, short timescale data collection (10–20 s), and measurements of frequency-dependent viscoelastic moduli. Furthermore, multiple bead tracking can be used to measure multiple samples simultaneously (Wirtz, 2009). However, the drawbacks include random motion of the beads could cause imaging problems due to halo effects or disappearance of the bead, and would be challenging to apply to very stiff or viscous materials (Cicuta and Donald, 2007).

## 1.5 Atomic force microscopy (AFM) force spectroscopy

The AFM technique was developed in 1986 (Binnig et al., 1986), and now is routinely used for biological sample imaging, stiffness measurements and quantifying molecular interactions (Kamm et al., 2010). It was first used to image biological samples (H G Hansma and Hoh, 1994), before looking at their mechanical properties (Radmacher et al., 1993; Weisenhorn et al., 1993). In this sub-section, we will discuss how force spectroscopy is carried out, along with how elasticity is extracted and other applications of AFM.

### 1.5.1 Operational principle

An AFM is a type of scanning probe microscope that uses a piezo drive mechanism to move the cantilever in any direction to gather the information required (Figure 1.3). By reflecting a laser beam off the back of the cantilever, movement of the cantilever can be tracked by position sensitive photodiode detector. This movement can be quantified by a change in voltage, compared to that when the laser hits the central position of the detector. The systems usually contain a feedback loop that can be closed during measurement; outputs from this loop will monitor the deflection of the cantilever and adjust the z-piezo according to a set deflection specified by the user.

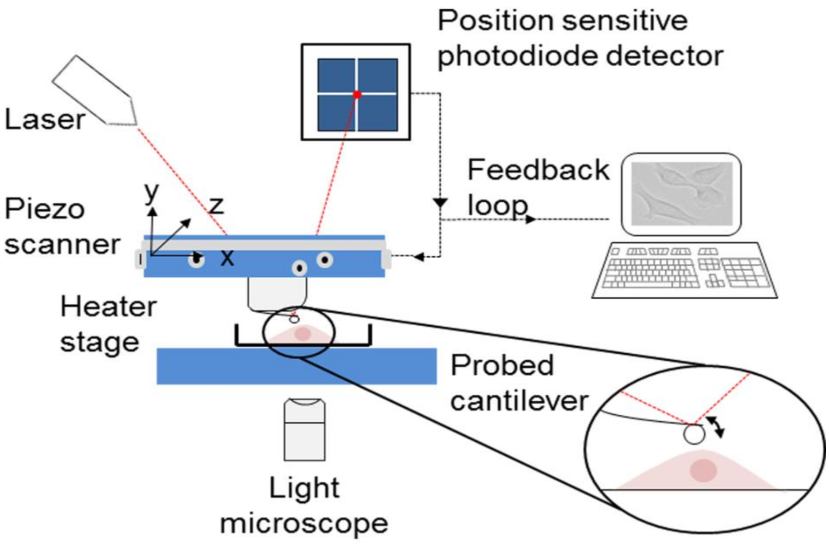

**Figure 1.3│Schematic diagram of the set-up for atomic force microscope (AFM), highlighting spherical probe indentation on a cell.**

To obtain elastic properties of a material, AFM force spectroscopy is used. The various modes of force spectroscopy can be categorised into contact, tapping and non-contact modes (Friedbacher and Fuchs, 2009). Here, we will discuss contact mode force spectroscopy, as this is the most well-established form. This process entails a probed cantilever being brought towards the surface of a sample in the z-direction, and then retracted away without scanning in the x and y directions. Once the cantilever is retracted away, a plot of force-distance curve is produced (Figure 1.4). The distance displayed in the curve corresponds to the piezo movement during the measurement. This means it does not take into account the change in deflection of the cantilever. By calibrating the system prior to measurements, a conversion between voltage to force can be made (Hutter and Bechhoefer, 1993). This means that the computed distance can be corrected for using the calibration measurement, so giving an indentation into the sample as opposed to the z-distance movement.

The produced force-distance curves can provide information regarding the sample before any analysis is taken place. In Figure 1.4, two curves are displayed. These describe the approach of the probed cantilever moving towards the surface of the sample (red line) and the retraction of the probed cantilever moving away from the surface (blue line).

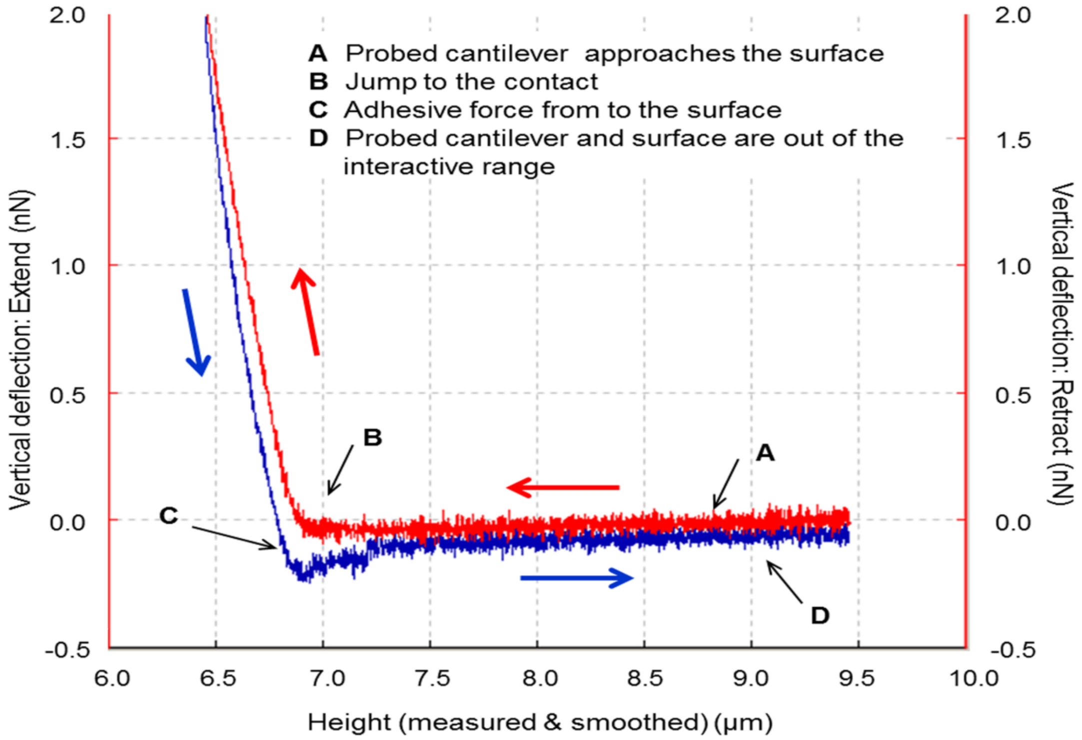

**Figure 1.4│Typical force-distance curve on a cell computed out from AFM NanoWizard II (JPK Instruments).**

There are four steps that the probed cantilever undergoes during a measurement. Firstly, the probed cantilever approaches the sample; this creates the baseline trace that must be accounted for in the measurements. The fluctuations within this baseline can be either thermal fluctuation (if the measurement is in air) or hydrodynamic forces acting upon the cantilever (when the measurement is in liquid). Once the indenter is in contact with the surface, the cantilever would start to deflect. As the indenter moves into the sample, repulsive forces are acting on the cantilever. This movement continues until the set force is approached and then the indenter starts to move out of the sample. Upon retraction of the indenter off the sample, it is often noticed that there are adhesive forces between indenter and sample. These forces could be caused by capillary forces when measurements are in air or specific/ non-specific binding forces when the sample is a cell. Once pulled free, the probed cantilever moves away from the surface back to the original point and creates another baseline in the process. In the above example, the difference between the approach and retracted baselines could be explained by hydrodynamic forces acting on the cantilever as it moves towards the liquid and away from the liquid.

### 1.5.2 Elasticity calculation

The stiffness can be extracted from force-indentation curves, without the need of modelling the data. This property can be calculated from the gradient between force and distance, which is based on the sample obeying Hooke’s law. The Hooke’s law states that the strain in a solid is proportional to the applied stress, within linear-elastic regime of loading. This property is known to be a general term describing a solid body. Meanwhile Young’s modulus (elasticity) is an example of stiffness, which is more specific and describes the property of a constituent material; the normal stress is divided by the normal strain experienced by the material within the linear-elastic loading regime.

The Young’s modulus of the sample can be calculated from force-indentation curves by fitting the data to a mathematical contact model. Although there are many contact models, the method was first pioneered by Heinrich Hertz and most other models are modifications of the original (Puttock and Thwaite, 1969; Shi and Zhao, 2004). The Hertz model has been the most commonly used and most favoured model, especially with biological samples. The model describes the forces when two spheres with different radii are brought into contact (Bhushan, 1990) (Figure 1.5). With the original model, there are a few assumptions: (i) the surfaces should be parabolic, continuous, smooth, regular and frictionless, (ii) the size of the contact area is small in comparison to the size of the bodies, i.e., small deformations typically < 10% of sample thickness and the indentation is > 200 nm (Pelling et al., 2007), and (iii) each of the bodies behave as an elastic half-space in the vicinity of the contact region. The fact that biological samples such as cells are not elastic, homogenous, and isotropic, means that the calculated Young's modulus will contain some degree of error. In the Hertz model for a spherical indenter, the applied force ($F$) can be written in terms of indentation ($\delta$) as:

$$F = \frac{4}{3}\frac{E}{1-\upsilon^2}\sqrt{R\delta^3}$$

where $\upsilon$ is the Poisson's ratio (for a cell; $\upsilon$ = 0.5 assuming it is incompressible), $R$ is the radius the indenter, and $E$ is Young's modulus.

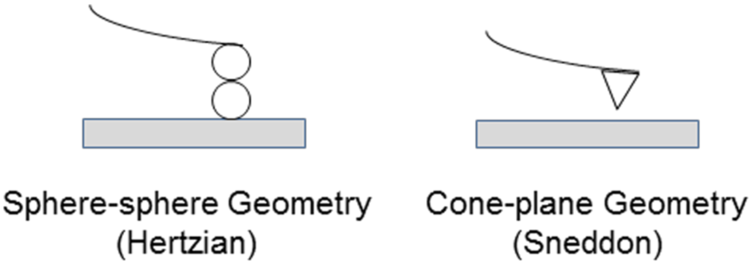

**Figure 1.5│Sketch of the cantilever probes.**

Sneddon's variation of the Hertz's model uses a conical indenter, though the assumptions for the model are the same (Figure 1.5). This model can be expressed in terms of applied force as follows (Kuznetsova et al., 2007):

$$F = \frac{2}{\pi}tan\alpha\frac{E}{1-\upsilon^2}\delta^2$$

where $\alpha$ is the half opening angle of the tip for conical indentation.

When measurements are carried out on very thin material, the Hertz model cannot be applied, due to strong substrate effects. However, by modifying the Hertzian model it can be applied., This variant is known as the Chen model or Tu model (Lee, 2011). Chen's model applies in a regime where the sample is attached to a substrate, for instance measuring the leading edge of a cell where the cytoskeleton adheres to the substrate. The advantages of this model include ability to measure elastic property and the Poisson's ratio (this was assumed in the Hertz and Sneddon model). The Chen model can be written in the ratio of the elastic constants for Hertz and Chen model ($K_{\mathrm{Hertz}}/K_{\mathrm{Chen}}$) as follows (Mahaffy et al., 2004):

$$\frac{K_{\mathrm{Hertz}}}{K_{\mathrm{Chen}}} = \frac{3\pi}{4}(1-\upsilon)\frac{a_{\mathrm{Chen}}}{a_{\mathrm{Hertz}}}\sum_{i=1}^{N}\frac{{p_i}^{\mathrm{c}}(\upsilon)}{1+2i}$$

where $a_{\mathrm{Chen}} \equiv a$ and $a_{\mathrm{Hertz}} \equiv \sqrt{R\delta}$.

Here, notations are similar to above with the addition of $a$ is the contact area, and ${p_i}^{\mathrm{c}}$ values are calculated numerically and is dependent on the Poisson ratio.

Tu's model is applied to situations where the sample is sliding freely. Tu *et al.* modified the model system so as to describe a spherical body on a non-adherent layer, to limit the range of thickness (Tu and Gazis, 1964). Both Chen and Tu model were used to measure frequency-dependent viscoelastic properties. The Tu model can be written in the ratio of $K_{\mathrm{Hertz}}/K_{\mathrm{Tu}}$ can be written as the follow (Mahaffy et al., 2004):

$$\frac{K_{\mathrm{Hertz}}}{K_{\mathrm{Tu}}} = \frac{3\pi}{4}\frac{a_{\mathrm{Tu}}}{a_{\mathrm{Hertz}}}\sum_{i=1}^{N}\frac{{p_i}^{\mathrm{T}}}{1+2i}$$

where $a_{\mathrm{Tu}} \equiv a$ and $a_{\mathrm{Hertz}} \equiv \sqrt{R\delta}$.

Each of the above models includes the assumption that there are no adhesive forces between the surfaces. However, there are models that include adhesive forces, such as the Derjaguin-Müller-Toporov (DMT), Johnson-Kendall-Roberts (JKR) and Maugis-Dugdale models. A study comparing these models with the Hertz model concluded that if small loads were applied, the work of adhesion does not play a key role in the contacts (Shi and Zhao, 2004). Hence, the models Hertz, Sneddon, Chen and Tu model can still be used even when adhesive forces are present, when measurements are applied at small loads.

### 1.5.3 Applications of AFM methods to cell mechanics

AFM techniques have been evolving for several decades and now it is a powerful tool to acquire biomechanical properties of biological samples such as biomolecules and cells (Goldmann et al., 1998; Lieber et al., 2004; Vahabi et al., 2013; Weisenhorn et al., 1993; Zhao et al., 2006). Mechanical properties have been studied on the cell membrane (Scheffer et al., 2001) and measurements have been made of cell stiffness (Carl and Schillers, 2008) and cell viscoelasticity (Alcaraz et al., 2003; Ketene et al., 2012; Rebelo et al., 2013; Vadillo-Rodriguez et al., 2008). These techniques have been highly favoured as a means to measure cell behaviour due to high precision control of the loading forces (10 pN–100 nN), an ability to record strain-stress characteristics of individual cells with nanometre resolution, minimal sample preparation and an ability to examine live cells under physiological conditions (Sokolov, 2007).

## 1.6 Cancer cell migration

Conventionally, our knowledge about cell migration has been obtained through two-dimensional (2D) studies (Doyle et al., 2009). However, there have been studies to suggest that cells migrate differently in three-dimensional (3D) models compared to 2D models. This can occur as cell motion switches from an adhesion-independent mechanism in 3D to adhesion-dependent mechanism in 2D (Lämmermann et al., 2008). This in order to have a clearer understanding of cancer cell migration *in vivo*, we study cells in 3D model systems. Here we will discuss current procedures used for 3D *in-vitro* cell migration by describing the principles of each procedure and highlighting their advantages and disadvantages.

### 1.6.1 Boyden chamber

The Boyden chamber (also known as transwell assay), is commonly used to study the chemotactic ability of cells through migration. This technique was initially created to study the cell migration of leukocyte cells under the influence of antibody-antigen complexes (Boyden, 1962). It involved two compartments separated by a membrane filter having a specific pore size (smaller than the investigated cells); the cells were seeded on one side while the chemoattractant was placed in the other. Due to the chemical difference between the two compartments, over time cells would transmigrate through the porous membrane towards the chemoattractant. These cells were then fixed, stained and counted under a microscope to calculate the migration rate. More recently, this procedure has been modified by pre-coating the membrane with a Matrigel containing extracellular components, to assess tumour cell invasion and motility through the gel (Saito et al., 1997). In addition, a colorimetric assessment (crystal violet) as oppose to the microscopic assessment has been used to quantify the assay. Other modifications have been to place different cells in separate chambers, to study the effect of soluble factors on cell migration, or to seed cancer cells on a monolayer of endothelial cells (Katt et al., 2016; Rodriguez-Menocal et al., 2012). This general procedure offers the unique advantages of being able to analyse cell migration and cell invasion in response to a chemotactic gradient. Furthermore, it has the ability to study either adherent or non-adherent cells (Hulkower and Herber, 2011). However, there are several limitations to this method that include the fact that the established gradient is transient, the results can be misleading due to an uneven distribution (or staining) of cells, or the transmigrated cells could be a subpopulation of tumour cells (Brekhman and Neufeld, 2009). Furthermore, it is often difficult to distinguish between the cells and the pores of the membrane (see images in Chapter 4).

### 1.6.2 Gel invasion assay

Biological hydrogels that include collagen, fibrin and agarose have been used for invasion assays. There are three approaches to this method, which includes cells being cultured on glass/ polystyrene substrate with a hydrogel with a thickness of 500 µm on top, or cells seeded onto a hydrogel with a thickness of 300 µm (Hooper et al., 2006). The migrated cells can be viewed and measured by optical sectioning through/from the gel, or by radioactive labeling of the cells (Kramer et al., 2013). The first mention of this type of assay is in a skin cancer cell invasion study, whereby the model was later known as organotypic skin model (Fusenig et al., 1983; Timpson et al., 2011a). In this study, fibroblasts (or immune cells) were embedded in the gel and the keratinocytes were seeded on top, with the migrated cells being quantified using histochemical staining. The advantages of this procedure are that it can mimic the *in-vivo* environment, allow observation of cell invasion and heterotypic cell-cell interactions between two seeded cells. However, the drawbacks include preparation can take a long time, there is an inability to quantify extent of invasion due to unknown start positions, and cells on substrates face a competitive situation whereby they could favour either movement into the substrate or the gel matrix above.

### 1.6.3 3D tumour spheroid invasion assay

The spheroid invasion assay was adapted from the situation that occurs whereby a cluster of tumour cells invade the surrounding tissue (Mueller-Klieser, 1987). Clusters of cells can be made *in-vitro* by forming small aggregates of cells that are known as multicellular spheroids. These clusters of cells or single cell suspensions are embedded into an extracellular matrix gel that contains another cell type. Cell invasion can be studied via cell migration towards the spheroids (intravasation) or when cells from the spheroids migrate out (extravasation). This method has been used to study the invasion properties of malignant cells into the spheroid structured of non-malignant cells (Vinci et al., 2015). The cells attached or invaded into the spheroids can be analysed using confocal fluorescence microscopy as the cells were fluorescently labelled or quantified by flow cytometry after trypsinisation. The advantages of this procedure is that cancer cells in a 3D structure mimic a tumour micro-region or micro-metastasis, the size of the spheroids can be controlled, and the invasion assay can be performed along with tumour spheroid formation in the same plate (Kramer et al., 2013). However, this process has similar drawbacks to the gel invasion assay in that the process can be long, the malignant cells are capable of forming spheroids, and movement is difficult to quantify due to an undefined origin of migration.

### 1.6.4 Oris 3D embedded invasion assay

The invasion assay uses a similar set-up to cell exclusion zone assay, whereby a single layer of cells were seeded around a small silicone stopper that creates the exclusion zone (Kramer et al., 2013). In this procedure a thin coat of basal membrane extract (or collagen) was made prior to positioning the silicone stopper and cells. Once cells have adhered, the stopper was removed (creating an exclusion zone), and the set-up was overlaid with a thicker layer of gel. This meant that cells were embedded between two layer of gel and a cell-free zone filled with the gel. The invasive cells would migrate into the cell-free zone and can be tracked under a microscope (Lim et al., 2010). Fixation of cells along with immunofluorescent staining can be carried out too. The advantages of this process is that the set-up is rather simple, real-time imaging of cell migration is possible due to the thin layer of gel and cell morphology can be studied at the end of the assay (Kramer et al., 2013). However, within this method there are no cell-cell interactions established before the assay as cells were seeded in a layer of single cells, no chemical gradient present to drive the cells, and the possibility that cells can migrate upwards as opposed to along the gel.

### 1.6.5 Microfluidic methods

Currently, there are more studies adopting the microfluidic approach to investigate cell migration in 3D, due to the controllability of the design that can be tailored to the cells under investigation, the ability to mimic the cell's physiological environment, and as a means to study low numbers of cells or single cells (Halldorsson et al., 2015). In addition, microfluidic approach does not require large amounts of sample/reagents, it can be used in high-throughput experiments, and real-time cell migration can be observed using optical microscopy.

To investigate the invasiveness of cancerous cells in a well-defined 3D environment, the development of micro-sized channel structures at various widths for cells to migrate through was required. There are various studies using different channel dimensions to address certain issues (Hung et al., 2013; Mak et al., 2011, 2013). To highlight a few designs, there have been studies where four arrays of 50 microchannels of dimensions between 6–100 µm in width with 3 or 12 µm in height are positioned above a central well that is connected to a media supply (Irimia and Toner, 2009). This was used to study various cancer cells and whether treatment targeting microtubules affected migration. Another approach has been to study the cell behaviour when moving from an unconfined space to a confined space. In this, the array of channels were tapered from 20 µm to 5 µm wide at a height of 10 µm, which was separated by two chambers (Rao et al., 2014). A recent study, applied the two chamber approach to investigate how cells change when moving from one confinement to another. This was carried by using channel segments along the channel length with widths varying from 11.2 to 1.7 µm and having a constant height of 3.7 µm (Lautscham et al., 2015). There have also been studies whereby cells were confined under 15 µm wide and 50 µm height channels, and the channel surfaces were treated with Matrigel, to mimic the physiological environment for cells. The results showed that invasive cells can migrate faster through these channels as opposed to non-invasive cells (Chaw et al., 2007).

Under physiological conditions, cancer cells are not often in uniform environments. Instead, they are most often in complex chemical environments where chemotaxis is guided by concentration gradients of growth factors, chemokines, and/ or surface ligands (Halldorsson et al., 2015). Cells regulate their behaviour accordingly, to sense the variation in chemical concentration within their surrounding area (Keenan and Folch, 2007). Steady state gradients in a microfluidic devices can be controlled by generating flow-based gradients, diffusion based gradients, or micro-patterning gradients (Huang et al., 2011). However, although chemical gradients can be controlled within microfluidic devices, it has been shown that cells can spontaneously migrate even in the absence of a gradient (Irimia and Toner, 2009). Thus this needs to be considered when interpreting observations of cell movement.

Another approach used to guide cell migration involves regulating the physical environment; such as substrate stiffness gradient or fluidic shear stress (Sant et al., 2010). This process is known as mechanotaxis. There has been evidence to show that fibroblasts, muscle cells and macrophages migrate from softer to stiffer surfaces (Kidoaki and Matsuda, 2008; Lo et al., 2000; Wong et al., 2003).

## 1.7 Aims and objectives

Cancer is one of the leading causes of death worldwide, in particular pancreatic ductal adenocarcinoma (PDAC). ROCK signalling has been extensively researched in cancer, particularly in relation to tumour cell motility and metastasis (Rath and Olson, 2012). However, the contributions of cell mechanics and cell migration have not been explored for PDAC, although tissue mechanics has been a feature used to distinguish between healthy and diseased pancreas. Therefore, this thesis research aims to unravel the involvement of ROCK activity in PDAC cells, from single cell mechanical behaviour to single cell invasion. To fulfil this aim, several objectives were constructed, as highlighted below.

To discover the effect of ROCK activity on single cell mechanical response, our objective was to measure the elastic and viscoelastic properties of cells that can overexpress ROCK, using AFM. Furthermore, to observe the cytoskeletal changes between normal and overexpressed ROCK, we used immunofluorescence staining of actin network.

Since it was known that there were limitations with using current methods to measure the viscoelastic properties of cells with AFM, thus there was a desire to establish a new procedure. Establishing this new viscoelastic measurement procedure with cells, validation investigations were made by comparing compact rheometry measurements of complex materials (30 kPa, 100 kPa, multi-purpose tac and 20:1 polydimethylsiloxane) with those derived from the new AFM based technique.

Finally, to investigate the effect of ROCK activity on single cell invasion, our objective was to design a microfluidic platform for these cells to probe migration through well-defined multidimensional restrictive channels. This would be used to correlate the measure cellular mechanical behaviour with cell migration.

## 1.8 Thesis outline

The thesis was organised into six chapters which are structured as follows:

***Chapter 1***: Introduction: discusses the background of the field of cell mechanics and cell migration for cancer research. Initially explores the fundamental components of a cell that contributes towards cell mechanics, and then highlights advantages and disadvantages of the available mechanical techniques. It includes descriptions of the basics of atomic force microscope force spectroscopy and the models used to extract elastic properties and the possible applications. Finally, discusses the basics of cancer cell migration in 3-dimentional techniques.

***Chapter 2***: Effect of ROCK activation on cell elasticity: presents the elastic response of cells along with immunofluorescence imaging of actin network within the cells, when overexpression of ROCK activity was applied. Furthermore, explores the possible downstream protein that contributes to the cellular response of overexpressed activity.

***Chapter 3***: Cell viscoelasticity: describes a novel procedure to measure the continuous change in viscoelastic properties of cells, over a wide range of frequencies. Initial investigations with applied procedure on cells have opened up a new method that can be used to measure cell mechanics.

***Chapter 4***: Cancer cell migration: describes the design and fabrication of a high-throughput microfluidic device with an array of microchannels with various dimensions. The effects of cell confinement on cell migration were observed with use of cells from chapter 2 and 3.

***Chapter 5***: Conclusions and future work: draws together the conclusions of the experimental chapters and highlights the main findings and conclusion of this work. In addition, further investigations that could be explored using the novel viscoelastic procedure, and established microfluidic device are mentioned.

# Chapter 2 Effect of ROCK Activation on Cell Elasticity

## 2.1 Abstract

Pancreatic cancer is the fifth most common cause of cancer death, in Europe. There are no symptoms during the early stage, therefore it is often diagnosed at a very advanced stage, which leads to poor prognosis. Although advances have been made in diagnosis and treatment, there has been less progress in treating the spread of the disease. It is known that overexpression of rho-associated kinase (ROCK) can lead to cell invasion and metastasis, though how cells move through tissues remains unclear. Here, we use atomic force microscope (AFM) force spectroscopy to measure the effect of ROCK overexpression, and cofilin activity on the mechanical properties of pancreatic cancer cells. Overexpression of ROCK led to a reduction in elasticity by 49–58%, whereas with cofilin activity, cell elasticity increased by 36%. This indicated that the cofilin activity is an important contributor towards the mechanical behaviour change that occurs with overexpression of ROCK. These findings were in agreement with the observed actin structures. Blebbistatin was also used on the cells to inhibit the myosin II activity that occurs when ROCK is active. However, as myosin II activity is not exclusive to ROCK activation, the decreased elasticity was observed for cells with both normal and overexpression of ROCK.

## 2.2 Introduction

Pancreatic adenocarcinoma occurs when cells from the exocrine duct begin to grow in an uncontrollable manner. It is known to be one of the most lethal malignancies, and due to its aggressive nature, it is most frequently seen at the time of clinical diagnosis (Kaneko et al., 2002). Therefore there has been urgent need for new treatments and diagnostic approaches.

ROCK signalling has been extensively researched in cancer, particularly in relation to cell motility, invasion, metastasis and apoptosis (Itoh et al., 1999; Lochhead et al., 2010; Riento and Ridley, 2003; Xu et al., 2012). These cellular processes are controlled by reorganisation of the cytoskeleton and regulation of actomyosin contractility. ROCKs are downstream signal transducing proteins from Rho GTPase (Rath and Olson, 2012). The pathway is activated by GTP-RhoA, which in turn phosphorylates various downstream proteins that include LIM kinase 1/ 2, myosin light chain (MLC), and the myosin binding subunit, MYPT1 (one of the three subunits that compose MLC phosphatase) (Figure 2.1).

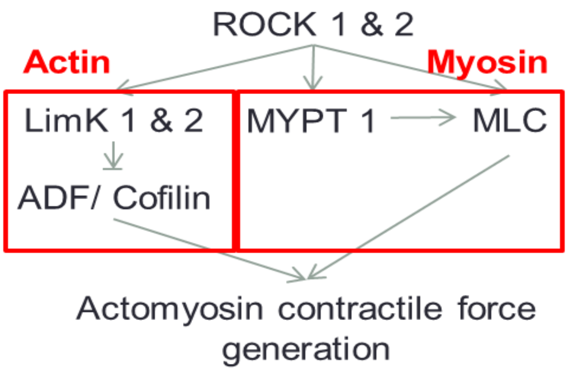

**Figure 2.1│A schematic diagram of the ROCK signalling pathway once activated.**

The ROCK pathway can be divided into two elements that consist of actin organisation and stress fibre formation/ cell contraction. The actin cytoskeleton is stabilised through activation of LIM kinases (Morgan-Fisher et al., 2013). These kinases are involved in actin-binding that catalyses the transfer of phosphate groups to cofilin. The function of cofilin (actin depolymerisation factor (ADF)/cofilin) is to break down actin filaments (Popow-Woźniak et al., 2012). This activity can be reversibly controlled by phosphorylation (addition of phosphate group) and dephosphorylation (removal of phosphate group). With ROCK activation, the LIM kinases are activated and in turn cofilin is phosphorylated, thus inhibiting cofilin activity.

The formation of stress fibres involves bundles of actin filaments of alternating polarity and myosin II (Riento and Ridley, 2003). Adding adenosine triphosphate (ATP) to separate stress fibres generates contraction. With ROCK activation, MLC is phosphorylated which increases myosin II ATPase activity and in turn contracts the bounded active myosin on actin filaments (Connell and Helfman, 2006). Increased levels of phosphorylated MLC occur during ROCK activation, through inactivation of MLC phosphatase.

Melanoma skin cancer was previously studied to understand how actomyosin cellular tension from activated ROCK2 activity affected the mechanical property of the formed tumour (Samuel et al., 2011). However, it was unclear how keratinocytes that were differentiated and migrated from the epidermis layer had changed its cellular mechanics in relation to tissue stiffening.

The mechanical properties of cells are dependent on two factors: changes in the structure of the cytoskeleton, and cytoskeletal tension (Martens and Radmacher, 2008). There have been studies to link mechanical properties of cells with signalling pathways in which these factors are regulated. ROCK activation in cells has been shown to increase intercellular stiffness (Wilhelm et al., 2014), though there is a decrease of cellular compliance of the cytoplasm (Kole et al., 2004). The reason for the effect has been associated with cell morphology and adhesion. When ROCK was deleted, the cells increased in surface area as they became flat, displayed fewer central stress fibres and there was a decrease the number of focal adhesion points (Kümper et al., 2016; Yoneda et al., 2005). This has been thought to be connected with both RhoA activity and degree of decoupling between RhoA and ROCK activity, regulators of cell spreading.

Within this chapter, we try to observe the effect that overexpressed ROCK activity has on the mechanics of single cells. This could lead to a better understanding of the proteins that may contribute to the change in mechanical properties. The information gained could bring us a step closer in understanding how ROCK activity contributes the overall tissue stiffening.

## 2.3 Materials and Methods

### 2.3.1 Materials

The general regents used throughout the experimental studies were purchased from Sigma Aldrich. The materials used for cell culture were obtained from Invitrogen. The remaining reagents that were not purchased from either company will be stated in the text.

### 2.3.2 Cell culture

The cells used in the experiments describe include extracted primary murine keratinocytes and various pancreatic ductal adenocarcinoma (PDAC) cells. All cells were supplied by the Beatson Institute of Cancer Research, Glasgow, UK.

Extracted primary keratinocytes were from two murine models (Samuel et al., 2011). One set of mice expressed the human ROCK2 kinase domain fused to mutant 17b-estradiol, an insensitive estrogen receptor and enhanced green fluorescent protein, under the control of the K14 promoter (QKR:ER). The other set contained a kinase dead protein version with similar fusion proteins (QKK:ER). These cells were only extracted from mouse tail skins and cultured when needed. The extraction process involved separation of dermis and epidermis, with the aid of 0.1% v/v 80 mg/ml dispase II (Roche) in PBS for 2 hours at room temperature. The keratinocytes present in the epidermis layer were extracted from the tissue by incubation at 37°C, with 5% $CO_2$, in 0.25% trypsin- ethylenediaminetetraacetic acid solution for 10 minutes. After incubation, the cells and tissue mixture was filtered using 40 µm cell strainer (BD Biosciences). All the cells in the collected filtrate were sedimented at 716 x *g* for 5 minutes, and seeded onto collagen (3 mg/ml Purecol; Advanced BioMatrix) coated petri dishes with keratinocyte growth medium (KGM$^{TM}$-2 BulletKit$^{TM}$; Lonza). These coated dishes were created by coating the dish with 0.22% v/v collagen type I solution in PBS for 1 hour at 37°C; to assist attachment for the primary cells.

In our investigations, there were two parental PDAC cells that were extracted from two murine models (Morton et al., 2010). One set of mice expressed accumulating p53 mutants (p53 R172H), and the other set harboured a *Trp53* null allele (p53 fl). These cells had been extracted and immortalised, so were sub-cultured when needed. Further modifications were carried out using various procedures on PDAC p53 fl cells. Ecotropic retroviral infection (Allele Biotechnology) was applied to PDAC p53 fl cells to tag them with an enhanced green fluorescent-estrogen receptor protein (EGFP:ER), and EGFP-conditionally active ROCK1- and ROCK2-estrogen receptor fusion proteins (ROCK1:ER and ROCK2:ER). For continuous selection of the expressed cells, an addition of 2.5 µg/ml puromyocin was added to the cell's media, every third subculture. Amaxa Nucleofector® kit (Lonza) was used to modify ROCK1:ER cells, which were tagged with red fluorescent protein (mcherry) and cofilin protein (CFL1). Finally, Lipofectamine® 2000 reagent

(Invitrogen) was used to transfect ROCK1:ER cells, and tag them with MLC protein and non-phosphorylated MLC protein (MLC AA). All cells were validated by western blotting, to ensure the modification was successful. These modification processes were carried out by Dr. Nicola Rath and Dominika Rudzka at the Beatson Institute of Cancer Research, Glasgow, UK, and were done according to the manufacturer's instructions.

All PDAC cells were maintained in 25 $cm^2$ tissue culture flasks with Dulbecco's modified Eagle medium (DMEM) containing 10% v/v foetal bovine serum, 1% v/v antibiotics and 1% v/v L-glutamine. Once the flasks reached 70% confluence, the cells were sub-cultured. The cells were harvested from the culture flasks by washing with phosphate buffered saline (PBS) followed by incubation in 0.25% trypsin-ethylenediaminetetraacetic acid solution for 5 minutes, to detach cells from the flask surface. The cells were collected and sedimented by centrifugation at 318 x *g* for 4 minutes, before being reseeded into fresh flasks.

All cells mentioned above were cultured at 37°C, with 5% carbon dioxide ($CO_2$) in a humidified incubator.

#### 2.3.2.1 *Single cell culture*

For atomic force microscope (AFM) force spectroscopy and immunofluorescence microscopy, cells were seeded at a sufficiently low density that they were present as single cells in the culture dishes. For example, the cells were sub-cultured and reseeded on 34 mm petri dishes (TPP®) at a concentration of 659 cells/$mm^2$. These cells were incubated overnight at 37°C, 5% $CO_2$, so that they fully attached to the petri dish.

#### 2.3.2.2 *ROCK activation*

The majority of the cells used for the experimental work contained an estrogen receptor fusion protein that could activate the ROCK pathway. For these cells to be activated *in-vitro*, the cells were cultured in its medium that contained 1 μM (Z)-4-hydroxytamoxifen-ethanol (4HT). For the activation to be complete, the cells were incubated under their culturing conditions for more than 18 hours. When the cells required activation over a period of several days, the 4HT medium was changed daily.

### 2.3.3 Atomic force spectroscopy

The mechanical properties of single cells were performed with an atomic force microscope, NanoWizard II (JPK Instruments) combined with an inverted optical microscope, Zeiss AxioObserver A10 and a cell heater attachment. The system was placed on top of a vibration isolation unit, Micro 40 (Halcyonics). The complete set-up was in enclosed in an acoustically isolated in-house manufactured chamber. The chamber was created to eliminate any ambient noises during system's operation.

The force-indentation measurements were performed by using in-house made spherical probes comprising silica beads glued onto tipless cantilevers. To create these probes, it was required to collect together, a glass slide half covered with 4.74 μm silica beads (Bang Laboratories Inc.), epoxy glue (B&Q), and a tipless silicon nitride cantilever (arrow TL-1; NanoWorld).

To fabricate the probed cantilevers, firstly, a small portion of the epoxy glue was placed on the glass slide where there were no beads. The AFM controls were then used to cause the tipless cantilever to approach the edge of the puddle of glue. Once the glue surface was reached, the cantilever was moved laterally away from the glue, removing any express glue along the way. The cantilever was then lifted off the surface, and positioned over another region of the microscope slide so as to locate an isolated bead. Upon locating an isolated bead, the AFM controls were used to cause the cantilever to approach the bead, positioning the glue above it. The glue on the cantilever was kept in contact with the bead for ~ 30 seconds, before the bead and cantilever was retracted away. The final step was to keep the probed cantilevers overnight at room temperature so that the epoxy glue fully cured.

The cantilevers had a nominal spring constant value of ~ 0.03 N/m. Unless specified differently within the experimental chapters, the probe size and spring constants for the cantilevers were as stated above. Calibration procedures were performed before and after every probe addition and experiment; to deduce any variations in spring constants that might have occurred as a result of the experimentation. The calibration procedure used was that of Hutter and Bechhoefer in which a glass slide is used to obtain the sensitivity and spring constant values for each set-up (Hutter and Bechhoefer, 1993). Within the AFM software, the sensitivity value converts the applied voltage into distance value, while the spring constant value converts the distance value to a force value. These experimentally determined probe constant values are essential to convert the raw voltages and displacements obtained from the AFM system into values that can be used in subsequent analysis.

Once the probe cantilever had been calibrated, the cell sample was mounted onto the cell heater attachment, where it was heated at 38.5°C. The temperature was set higher than 37°C to accommodate for the heat to be transferred from the attachment to the petri dish. The cells can only be cultured outside $CO_2$ environment for 2 hours, which imposes a limit on the number of measurements that can be performed. Therefore to measure cells in a $CO_2$ free environment, the pH levels in the media were controlled. A difference in pH could cause cells to move faster and contract at the cytoplasm (high pH) or reduce cell activity and eventually stop, causing gelation of the cell (low pH) (Taylor, 1962). These effects could therefore lead to the overall change in a cell's mechanical behaviour. Here, I used HEPES buffered media to control the pH levels within the media, as HEPES is commonly used as a zwitterionic buffer (i.e. one that contains ions that can bear both positive and negative charges), with a buffering capacity range of pH 7.2–7.4 (Good et al., 1966). Although HEPES has the ability to control the pH level within the media, it has been suggested that cells were toxic (cytotoxic) with high concentrations of HEPES. Therefore, to evaluate the minimal concentration to use so as to keep the pH of the media within an acceptable range over the course of AFM experiments, a range of concentrations were tested at 37°C in $CO_2$ free environment for a period of 8 hours (Figure 2.2).

The results showed that over the 8 hour period, all concentrations increased in pH by the same increment. At the initial time point, 10 mM HEPES displayed the highest pH level (pH 7.59), compared to the other concentrations. Typically cells prefer to be in a pH environment between 7.4–7.7 (pH & $CO_2$ levels; ThermoFisher Scientific). Therefore, it was concluded that 25 mM HEPES should be added into the media used for AFM cell experiments, as this concentration allowed the media to hold its pH level close to the required physiological level for the longest period of time.

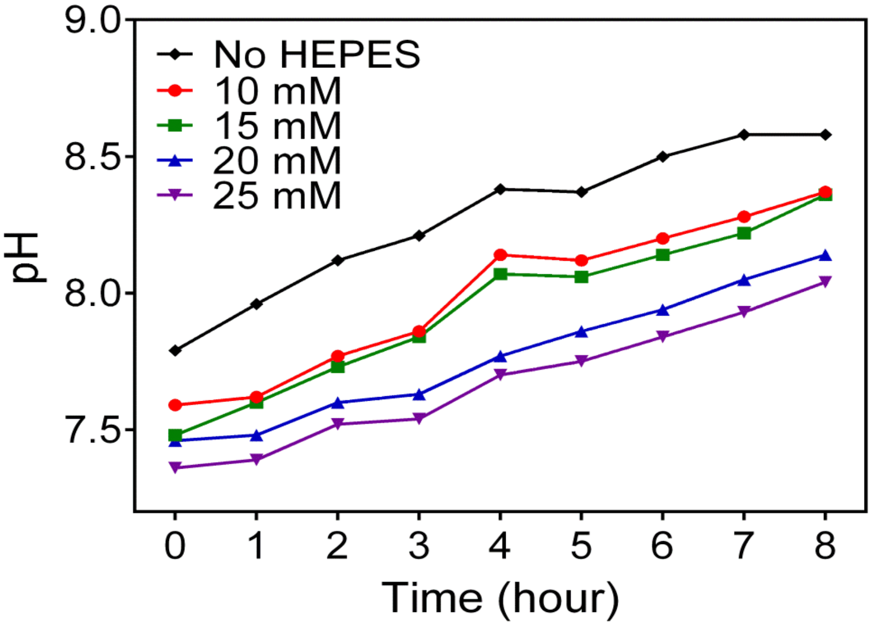

**Figure 2.2│ The effect of pH change according to the HEPES concentration in DMEM media, over 8 hours.** The highest concentration of HEPES gave the lowest pH value for a longer period of time, and vice versa for low concentrations.

Apart from the culture conditions, there were several parameters that needed to be considered as part of the experimental set-up. These included the substrate used for cell culture, indenter geometry, loading rate, position of tip-cell contact, depth of indentation, and the variability between cells in a population (Chiou et al., 2013; Lekka et al., 2012).

Firstly, cells are known to sense substrate stiffness and modify their mechanical properties to mimic them by adjusting their adhesion properties, cytoskeleton and overall state (Discher et al., 2005). Thin surface coatings (i.e. collagen, poly-l-lysine or fibronectin) have also been shown to be implicated in the mechanical behaviour, e.g. as the coatings adhesive properties increases, their elastic properties also increase (Lekka et al., 2012; McPhee et al., 2010). The objective of our investigations was to understand the mechanical behaviour of cells according to their expression of particular proteins. Therefore, it was only essential for us to be consistent with the substrate used, so comparisons between mechanical properties due to cell expression can be made. Consequently, for the majority of cells, culture on non-coated petri dishes was used.

For biological samples, it has been shown that spherical indenters can provide a wider surface-contact area, compared to using a sharp pyramid or conical indenter (Lin et al., 2006). This means that pressure applied onto the cell would be more dispersed, and hence lower when using a spherical probe. Meanwhile, the irregularity of the shape of sharp indenters could cause uneven pressures to be exerted on the cell surfaces and lead to large variations between the extrapolated mechanical properties of different cells (Sokolov, 2007). The reason for this could be due to local strain on the cell that resulted from non-uniform applications of pressure. Therefore, to gain a representative overview of a cell's mechanical properties, spherical indenters were used for all cell measurements.

Importantly, the size of the indenter in the above measurements was smaller than the cell, so that there were no complications in determining the contact area (Chen, 2014). The cells were typically 10–15 μm in size (refer to optical images within chapter), thus 4.74 μm silica beads were used within the investigations.

For AFM force spectroscopy, the loading rate is defined as the speed at which the cantilever is moved towards the sample. This rate has been shown to have an influence on the mechanical properties of benign and malignant cells (Lekka et al., 2012). When the speeds increased from 0.5 μm/s to 10 μm/s, both type of cells responded with an increased stiffness. However another study concluded that mechanical behaviour was not affected by loading rates between 1 and 25 μm/s (McPhee et al., 2010). Although there are mixed reviews on this matter, it was shown in that the variability between elasticity values was lower when low loading rates were used (0.5, 1.5 and 3 μm/s). As aforementioned, if the conditions were kept constant, the measured elastic moduli should be comparable. Hence, a loading rate of 2.5 μm/s was chosen for all the measurements in this study.

Another parameter to consider for the experimental set-up was the location on the cell that should be used for indentation. The elastic modulus of live cells have been shown to be significantly different for different regions of a cell (Kuznetsova et al., 2007). The review showed that cells were not definitively softer at the nucleus compared to the cell periphery or vice versa, the variation of elasticity was shown to be dependent on the presence of stress fibres. It has been suggested that measurements on the cell nuclei is advantageous as the nucleus is integrated with in cytoskeleton, so upon deformation it can remodel itself to maintain the cellular physiological environment (Liu et al., 2014). Therefore, to achieve narrow distributions in the measured elasticity for a particular cell line and for the consistency of using a well-defined point on the cell surface, the cells were measured at the apex of the cell nucleus.

The depth of indentation on cells has been shown to have an influence on their stiffness due to the cell's structural heterogeneity (McPhee et al., 2010). It was noted that an indentation depth of <100 nm when using fibroblast cells resulted in a large variation in the elastic modulus; this could be associated with network differences in the actin filaments. Meanwhile, the elasticity values for indentation depths of 300–600 nm were consistent. To determine the appropriate indentation depth to apply, we considered the assumptions applied to the Hertz model. For the model to work, small indentations should be applied to the material, <10% of sample's thickness (Lekka et al., 2012). We measured the height of the cells (PDAC p53 fl cells) using the AFM, which gave an average of 6.9 ± 1.9 µm. Therefore an indentation depth of 500 nm was chosen as a standard, used for all the cell experiments.

Finally, the variability between cells within the same population is a parameter to acknowledge in that it could result in large variations in the measured elastic values (Lekka et al., 2012). Within the same population, cells can vary according to their age, stage point in the mitosis cycle, or heterogeneity of cell surfaces (Sokolov, 2007). Therefore, to achieve robust statistics, both measurements on a large sample size were taken (n = 80 cells), and small number of indentations (5 indentations) on individual cells to observe their reproducibility were performed.

Once the force-indentation measurements have been obtained on the cells, phase contrast images were carried out using 20x LD, 0.4 NA, Plan-Neofluar objective (Zeiss).

#### *2.3.3.1 Data analysis*

The data analysis was carried out using an in-house algorithm (written in R), to eliminate any human error created by allocating the contact point by oneself. The procedure was adapted from Scott Crick and Frank Yin's method (Crick and Yin, 2007), to identify the contact point before applying a model to the data (Figure 2.3). The algorithm was written to firstly identify the "noise" present within the initial data (baseline). A window between 12.5–37.5% of the initial data was taken to calculate the mean and standard deviation (SD). The data was normalised, by subtracting each data point against the calculated mean. To identify the contact point, each data value was compared against the sum of the calculated mean and SD. When the data begins to go above this value, and increases for a certain number of consecutive points, the first point in this rising trend was taken as the contact point. However, to be certain this point provided the best model fit to the data, in fitting models, a 10% window was used. This 10% window was defined as 10% of the indentation depth used for the fitting model, i.e. 50 nm. The force-indentation data was then fitted to the Hertzian model, as this model describes a situation when a rigid spherical indenter was pressed on an incompressible linearly elastic half-space material. Formulaically this can be written as

$$F = \frac{4}{3}\frac{E}{(1-\upsilon^2)}\sqrt{R\delta^3}$$

where $F$ is the force applied, $E$ is the Young's modulus (elastic modulus), $\upsilon$ is the Poisson ratio (assuming a cell is an incompressible material, $\upsilon$ = 0.5), $R$ is the radius of the indenter, and $\delta$ is the amount of indentation applied.

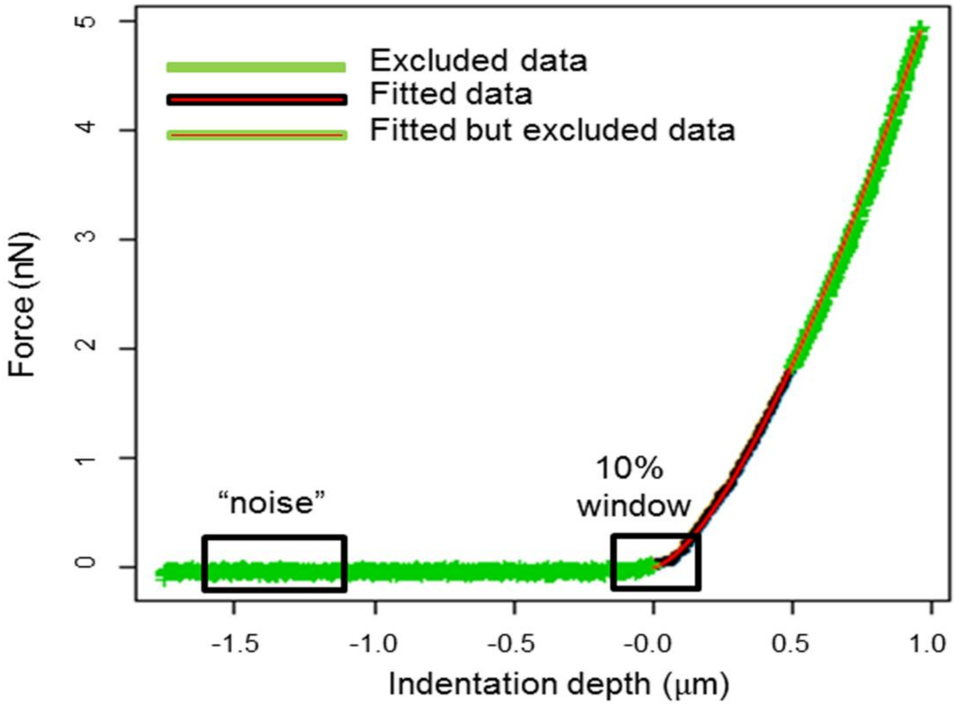

**Figure 2.3│ Analysed force-indentation result off cell measurement, using our in-house made algorithm.**

The procedure continued to apply fittings to the data that was within the 10% window. The data value that achieved the highest coefficient of determination ($r^2$) value was used to calculate the elastic modulus. The $r^2$ value from each measurement had to be above 0.95, for it to be used.

### 2.3.4 Actin staining

Immunofluorescence labelling was applied to the modified PDAC cells with and without the overexpression of ROCK. The cells were cultured on glass coverslips overnight in a 5% $CO_2$ incubator at 37°C, before stained for F-actin. Briefly, the cells were washed with PBS and fixed with 3.8% formaldehyde in PBS, in 2% sucrose for 10 minutes at room temperature. The cells were permeabilised with 0.1% triton X-100 in PBS for 10 minutes at room temperature. After permeabilisation, the cells were washed with PBS and blocked with 1% bovine serum albumin (BSA) in PBS for 30 minutes. The actin filaments were stained using phalloidin, BSA in PBS (1:500; Alexa Fluor® 488, Life Technologies) for 1 hour at room temperature. The stained cells were washed in 0.5% Tween20 in PBS and finally mounted onto a coverslip using Vectashield mounting medium containing DAPI staining (Vector Laboratories Inc.).

Differential interference contrast microscopy (DIC) and fluorescence imaging was carried out using a 40x, 0.75 NA objective on a Zeiss AxioObserver A10 microscope coupled to a DU885 iXon CCD. The set-up was operated using AxioVision software (Zeiss). For fluorescence imaging, the FITC filter (XF100-2; Omega Optical) was used to excite and detect phalloidin, and the DAPI filter (XF06; Omega Optical) was used to excite and detect DAPI. Each sample was exposed to the mercury lamp for different times dependent on the stain: phalloidin stains were exposed for 2 seconds, and DAPI stains were exposed for 0.3 seconds.

### 2.3.5 Statistics

The data was presented and statistically analysed using Prism 6 (GraphPad Software). The majority of the datasets in this chapter used two-way ANOVA statistical test that accepts or rejects null hypotheses. This method was chosen since within the various data sets, there were always two factors to compare e.g.

cells and treatment. The validity of using this method requires that the sample populations are independent, normally distributed, and their variances are equal – this is a reasonable supposition for the cells studied here. The null hypotheses for our datasets would be that there was no difference in means of cells, no difference in means of treatments and no difference in means of cells and treatments. If the test came back to show that the null hypothesis was rejected, then this means that at least the two populations were different from each other, using the 95% confidence value. To understand which populations were different from which, a post hoc test (Sidak test) was executed. The Sidak test is a conservative method, which means that the probability of falsely rejecting the null hypothesis is never greater than the nominal significance level ($\alpha$ = 0.05). The test determines the significance by an alpha level that can be written as

$$\alpha_s = 1 - (1 - \alpha)^{1/n}$$

where $n$ is the number of independent (comparison) tests conducted, and $\alpha$ is the nominal significance level. In this case, the p-value must be smaller than $\alpha_s$ for it to be considered as significant. The statistical significance was cut off at $p < 0.05$, whereby the p-value is the probability of the result given that the null hypothesis was rejected.

The remaining datasets whereby only one factor was compared, e.g. overexpression of cofilin, a paired two-tail student t-test was used. This was to compare the mean of two populations with unequal variance (standard deviation), to accept or reject the null hypothesis. The null hypothesis being that the two populations were equal to each other.

## 2.4 Results and Discussion

### 2.4.1 Effect of overexpression of ROCK on elastic modulus

Previous work has shown that tumour formation occurs in the QKR:ER mouse model when ROCK is activated, whereas the QKK:ER mouse model remained healthy (Samuel et al., 2011). In that work, the overall tissue stiffness was shown to increase when going from a kinase dead to a kinase active model. As it was unclear how individual cells changed during tissue stiffening, we investigated the effects of ROCK activation on these cells using AFM force spectroscopy, to probe the elastic properties before and after estrogen treatment. This treatment enables ROCK activation within the cells. A sample size of 80 cells was used and the extracted elastic moduli (*E*) were generated from the force-indentation approach curves, using the Hertz model (Section 2.3.3).

Prior to indentation measurements, the extracted keratinocytes were studied visually to see if there were any observations that should be considered when interpreting the AFM force spectroscopy measurements (Figure 2.4).

For example, there had been evidence to suggest that ROCK activation causes an increase in actomyosin contractility that could result in either a reduction in cell size and/or them becoming rounded (Kole et al., 2004; Lochhead et al., 2010). However, the observations here showed that the morphology of the cells extracted from the tissue was similar, before and after estrogen treatment. The measured surface area of individual cells confirms with the observations that showed untreated QKK:ER and QKR:ER cells were 178.58 ± 57.96 μm$^2$ and 221.75 ± 85.21 μm$^2$, respectively (n = 80 cells), while estrogen treated QKK:ER and QKR:ER cells were 182.11 ± 65.49 μm$^2$ and 224.78 ± 74.21 μm$^2$, respectively (n = 80 cells).

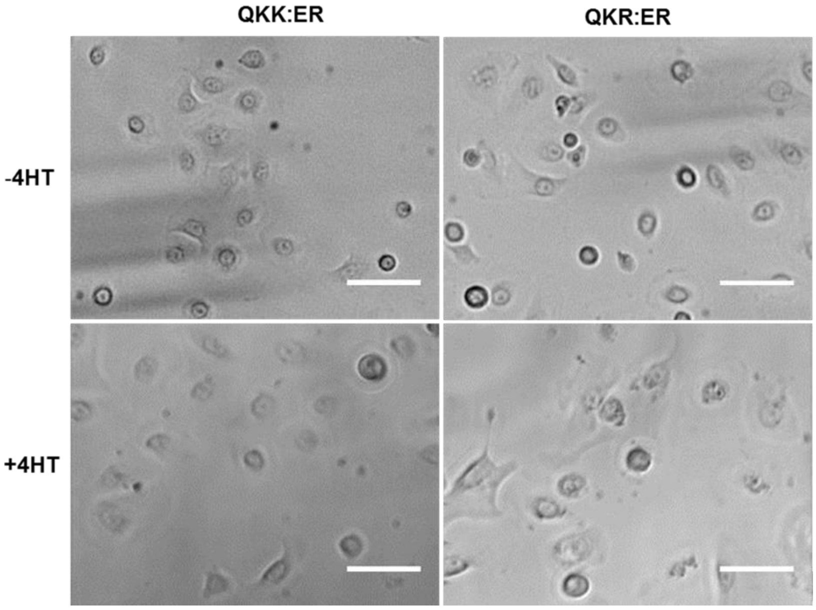

**Figure 2.4│Images of QKR:ER and QKK:ER cells in the absence and presence of estrogen (4HT) treatment.** All scale bars are 30 μm.

The study of the elasticity *in-vitro* showed that the elastic modulus of ROCK activated cells (QKR:ER +4HT) was significantly lower compared to the counter model cells (QKK:ER +4HT) and the untreated cells (QKR:ER -4HT) ($p < 0.0001$; Figure 2.5). While there was a difference in cell elasticity due to ROCK activation, the mechanical response remained unchanged within 2 days of treatment. This meant that the cells were unaffected by either the period of ROCK activation or of the increased cell density.

The average elastic modulus was 2.86 ± 0.93 kPa for QKR:ER -4HT, 1.47 ± 0.33 kPa for QKR:ER +4HT (1 day), and 3.21 ± 0.52 kPa for QKK:ER +4HT. This gives an average modulus reduction of 49% between the treated and untreated cells and 54% reduction between kinase active and kinase dead cells. Although, these observations were in close agreement with some studies where cancerous cells were more compliant than normal cells (Goldmann et al., 1998; Lekka et al., 1999, 2012; Sokolov, 2007), it was contradictory to other studies on ROCK activation.

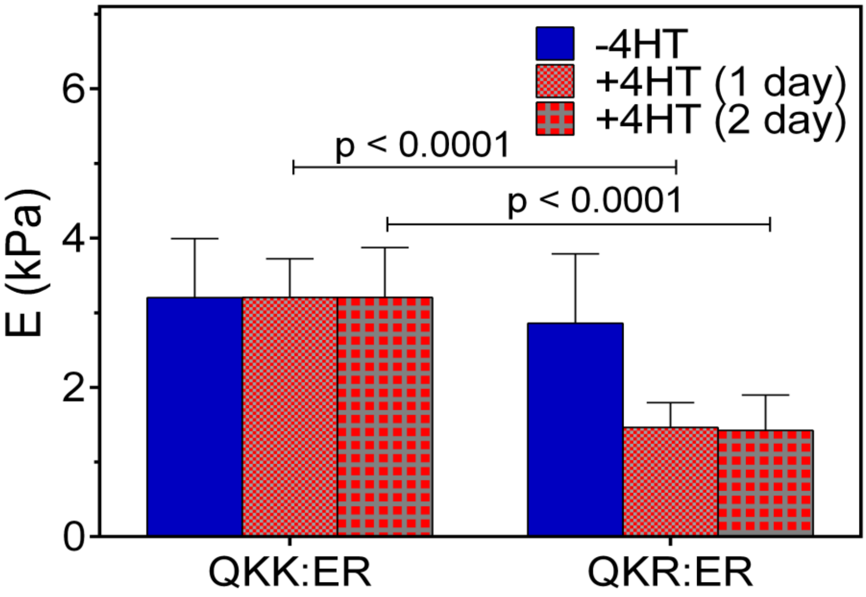

**Figure 2.5│Elasticity change of QKR:ER relative to QKK:ER following 4HT treatment (n = 80 cells), expressed as mean ± SD.** QKR:ER +4HT became softer in reference to the QKR:ER-4HT and QKK:ER+4HT ($p < 0.0001$).

In the literature, it has been shown that ROCK activation resulted in an increase in the overall elastic mechanical property of cells, however there was a decrease in the viscoelastic property of the cell cytoplasm (Kole et al., 2004; Wilhelm et al., 2014). These effects can be explained by the downstream responses from activated ROCK. ROCK activation promotes actin microfilament stabilisation, increases actin microfilament bundling and myosin-driven contraction (Rath and Olson, 2012). Due to the increased levels of contractile actin bundles, the overall stiffness increases and there has been evidence of an increase in actin cross-linker concentration, bundling length and diameter of the bundles: all these these factors directly increase the bending stiffness of the actin bundles (Bathe et al., 2008). However, in our study, ROCK activation led to a decrease in the elastic properties of cells.

The primary keratinocytes have exhibited softer characteristics when ROCK was activated. This could be associated with nuclei mechanical response to ROCK activation rather than the whole cell itself, as measurements were carried out on the apex of the nucleus. To understand whether this cell behaviour was solely shown in this model or that we have revealed new findings in the field of Rho GTPase, we carried out the same investigation on another cell line, PDAC p53 fl.

PDAC p53 fl cells were tagged with EGFP:ER, ROCK1:ER or ROCK2:ER. All cells exhibited normal levels of ROCK expression, although with estrogen treatment, ROCK1:ER and ROCK2:ER would overexpress ROCK1 and ROCK2 respectively. Again, the cell morphologies were observed, prior to the mechanical studies (Figure 2.6).

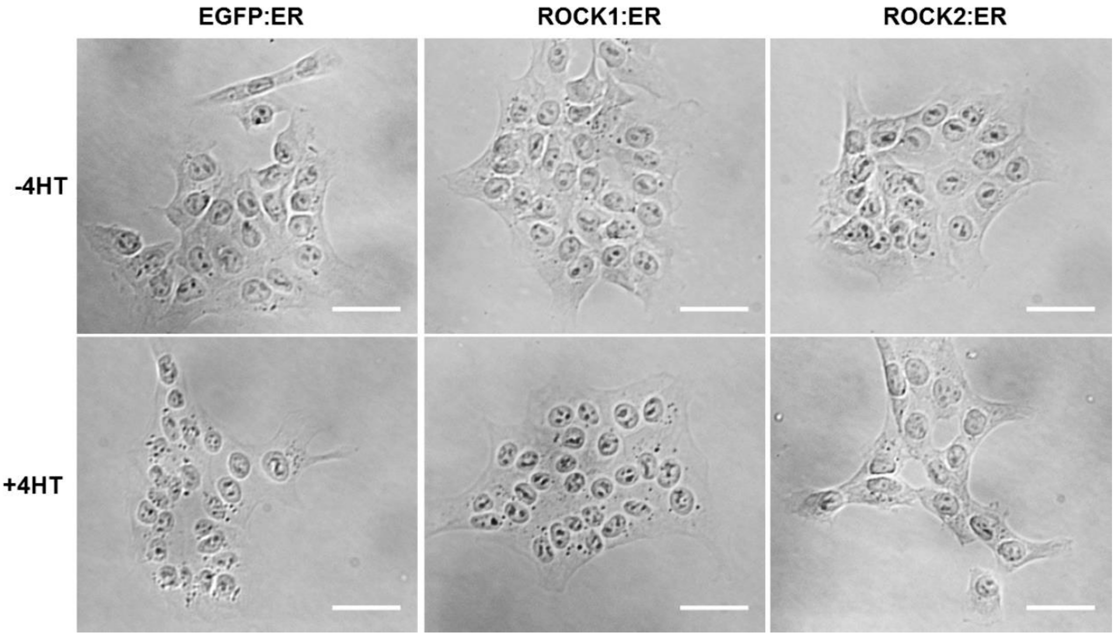

**Figure 2.6│Images of modified PDAC p53 fl cells in the absence and presence of estrogen (4HT) treatment.** All scale bars are 30 µm.

For all three modified cells, EGFP:ER, ROCK1:ER and ROCK2:ER, there were no differences in cell morphology before and after estrogen treatment. This was clarified with surface area measurements of cells from the images obtained. The surface area of untreated EGFP:ER, ROCK1:ER and ROCK2:ER cells were 322.71 ± 94.62 $\mu m^2$, 363.65 ± 87.39 $\mu m^2$ and 329.50 ± 87.62 $\mu m^2$, respectively (n = 80 cells). Meanwhile, estrogen treated EGFP:ER, ROCK1:ER and ROCK2:ER cells were 363.22 ± 81.94 $\mu m^2$, 340.53 ± 77.35 $\mu m^2$ and 342.44 ± 83.87 $\mu m^2$, respectively (n = 80 cells). These cells were similar to the primary keratinocytes both in terms of semi-rounded structure, and that they grow in colonies. As these cells were similar in morphology and grow in the same way to primary cells, our hypothesis was that these cells would exhibit a similar effect in mechanical response following an overexpression of ROCK.

The findings collected from AFM force microscopy showed that both ROCK1:ER and ROCK2:ER activated cells were significantly softer relative to the control (EGFP:ER) and the untreated cells ($p < 0.0001$; Figure 2.7). The ROCK1:ER cells displayed a reduction of 57% in Young's modulus, from 2.22 ± 0.72 kPa for the untreated cells to 0.95 ± 0.17 kPa for the treated cells.

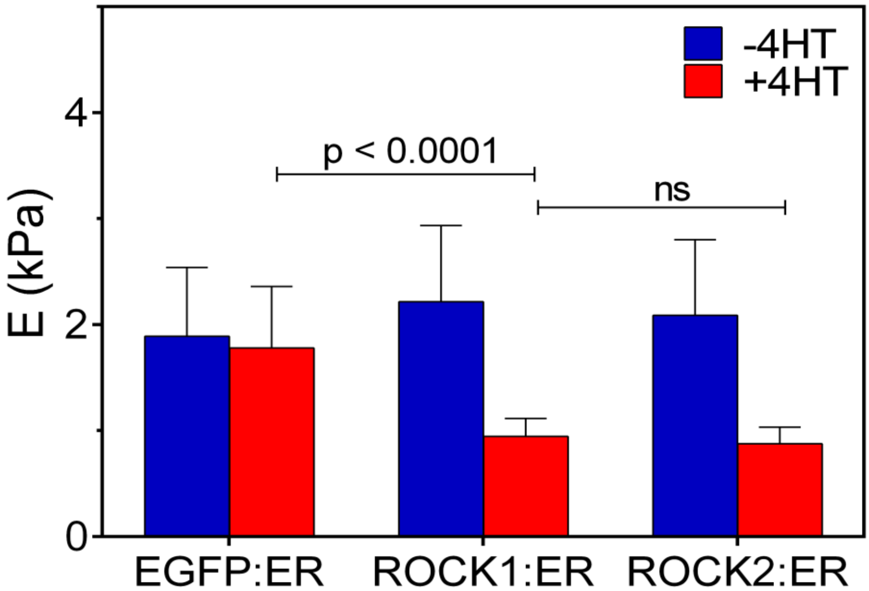

**Figure 2.7│Elasticity change of ROCK1:ER and ROCK2:ER relative to EGFP:ER following 4HT treatment (n = 80 cells), expressed as mean ± SD.** Both ROCK1:ER and ROCK2:ER cells were softer in reference to the EGFP:ER cells (p<0.0001).

Meanwhile, ROCK2:ER cells had a reduction of 58%, from 2.09 ± 0.71 kPa for the untreated cells to 0.88 ± 0.16 kPa for the treated cells. Moreover, the average elasticity between the untreated samples was significantly different to each other ($p < 0.0001$). Although it cannot be proven, the difference in elasticity could be associated with the number of proteins added to the cell, as there was no significant difference shown between the extracted primary cells.

The overview of the two experiments have shown that overexpression of ROCK in primary keratinocytes and modified PDAC cells, led to a decrease in elastic response. Although again this is contradictory to previous studies, the elasticity difference seen in these cells could be connected with the cells having grown colonies or the unchanged cell morphology.

In the literature, measurements were carried out on isolated cells that overexpressed in ROCK, and here our single cell measurements involved cells in colonies. This could mean that there was a cell-cell contribution to the measured mechanical response (Kole et al., 2004; Wilhelm et al., 2014). Furthermore, as discussed previously overexpression of ROCK has shown to alter cell morphology from a stretched to rounded cell. Although our cells were rounded before overexpression and the morphology did not change, the internal organisation within the cell may be different for overexpressed ROCK.

To address how cells grown in groups may affect their elasticity, we measured the elasticity of untreated ROCK1:ER cells in two conditions; isolated single cell (separate) and single cell in a colony (cluster) (Figure 2.8A and B). The culturing conditions were not altered to select for isolated or in colony cells, instead, over the same culture area, 17 randomly chosen cells from either condition were selected and probed to determine their elasticity.

Before the extraction of the elastic modulus from the force-indentation approach curve, we studied the difference between the curves. A typical force-indentation approach curve generated by a cell in a colony was found to be similar to a curve that was measured when a cell was isolated (Figure 2.8C). This meant that the extrapolated elastic modulus for the two types of cells should also be similar. The average elasticity value for cells measured in a cluster was 2.10 ± 0.78 kPa, while for isolated cells it was 2.20 ± 0.84 kPa (Figure 2.8D). Although there was a large distribution of values for the cells, there was no significant difference between the two populations of cells.

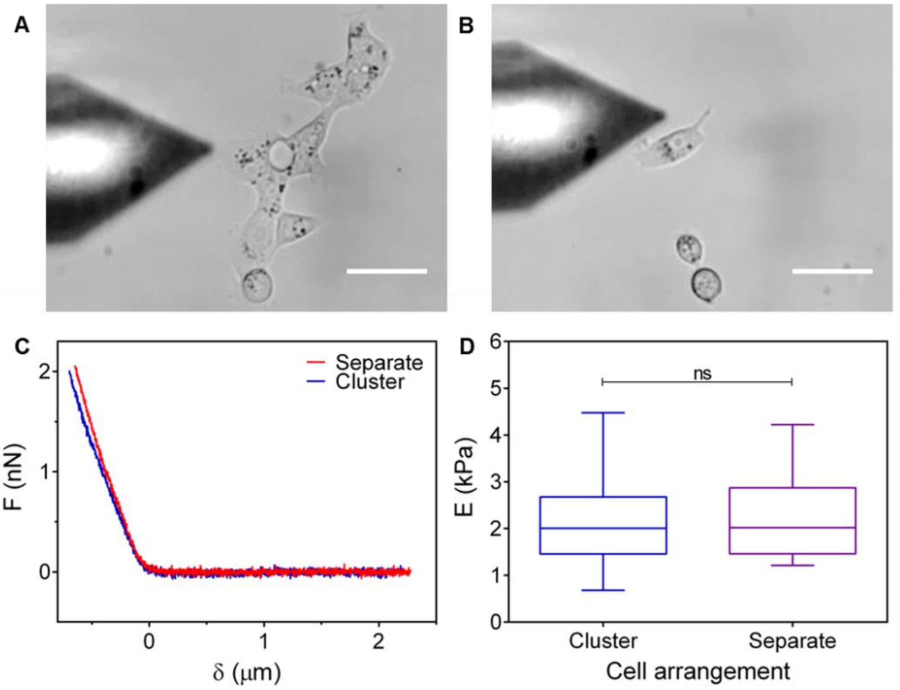

**Figure 2.8│Comparison between untreated ROCK1:ER cells grown independently or in clusters.** Cells in (A) clusters or are (B) isolated. All scale bars are 30 μm. (C) Representative force-indentation approach curves of cells in condition (A) and (B). (D) Box and whiskers plot of elasticity values measured from clustered and isolated cells. n=17 (p= ns; non-significant).

These observations were also found by other peers, which indicated that individual cells that were measured from the same position either isolated or grouped the cells would have similar mechanical properties (Stroka and Aranda-Espinoza, 2010). However, the elasticity changed when single cells were measured within a monolayer of cells. According to these findings, unless the colonies from treated and untreated cells were extremely different (colony grown in size to form monolayer), the mechanical response would be similar. Although there were no differences between isolated and group cells within the same population, this does not indicate whether ROCK activation of cells in colonies would have a downstream effect on the mechanical properties.

As the external cell morphologies for estrogen treated and untreated cells were the same, we investigated the relationship between the intracellular structures of these cells (Figure 2.9). This was performed by using immunofluorescence staining on EGFP:ER, ROCK1:ER and ROCK2:ER cells with and without treatment, to stain for F-actin and the nuclei within the cells.

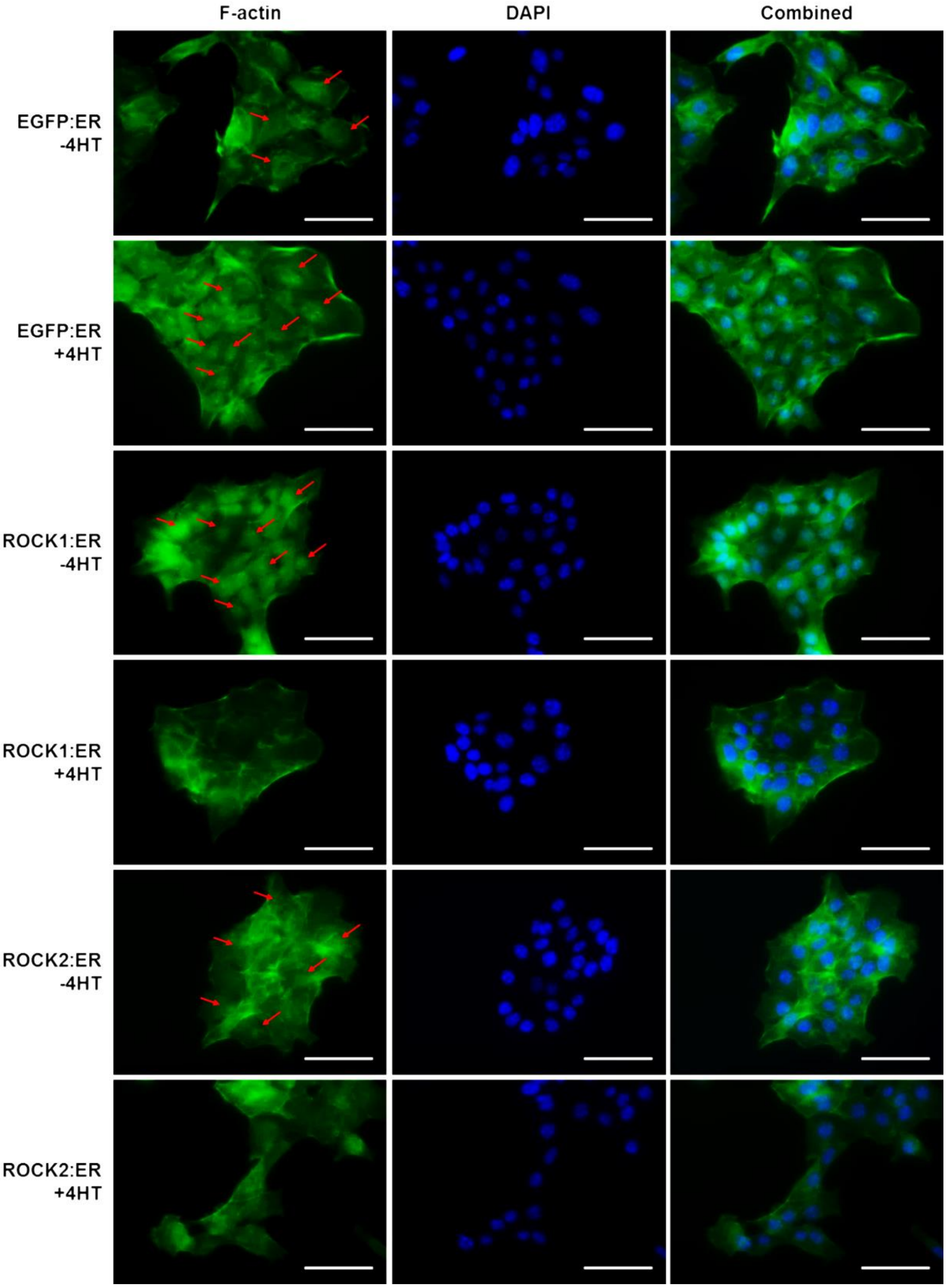

**Figure 2.9│Comparison between the actin filaments of modified PDAC cells in the presence and absence of 4HT treatment.** The fluorescent cells showing nucleus (blue) and F-actin (green). All scale bars are 50 µm. Red arrows indicate dense actin bundles. Overexpression of ROCK led to fewer bundles of stress fibres, and none at the centre of the cell compared to the control.

According to the images, a high density of actin bundles were present locally around the nucleus, in both EGFP:ER and untreated cells. Meanwhile, when ROCK1:ER and ROCK2:ER cells were overexpressed, the actin bundles were located mainly around the periphery of the cells. To understand the association between cell's mechanical behaviour and its cytoskeleton when ROCK was overexpressed, we need to understand the function of ROCK.

ROCK activation can stabilise actin cytoskeleton by the activation of LIM kinase 1/ 2, the formation of stress fibres from increased actin bundling and cellular contractility by activation of MLC (Morgan-Fisher et al., 2013). It was understood that cortical myosin II-dependent contractility occurred with ROCK activity. This association with the cortical region could justify for the presence of actin filaments at the periphery of the cell, when cells were overexpressed with ROCK activity.

To explain the difference in mechanical behaviour, we have to understand how cells in colonies act during contraction. It has been suggested that adherent and contractile colonies of cells would cause inwards stresses (Mertz et al., 2012). These stresses could lead to cell packing within a colony and hence the arrangement of stress fibres at the periphery of the cell (Stroka and Aranda-Espinoza, 2010). This downstream effect would result in softer cells, similar to the findings we gathered for overexpressed ROCK.

### 2.4.2 Cell activation in relation to ROCK

As pancreatic cancer is one of the major causes of cancer death and there has not been much advancement in the field (Baker et al., 2016), from here onwards the focus of this thesis is on the understanding the effects of PDAC cells' behaviour with overexpression of ROCK.

There are several paths in the ROCK pathway that could lead to an overall mechanical change for a cell (Figure 2.1). Interference on the main paths was conducted to further investigate how the cell mechanics of each element contributes to the overexpression of ROCK. By using the PDAC cells that were tagged with EGFP:ER and ROCK1:ER, these paths were investigated using some of the downstream proteins in the ROCK pathway. These proteins include cofilin, LIM kinase and MLC (details regarding these protein are given in Section 2.2).

Firstly, to investigate the effect of cofilin activation on the cell mechanics, we measured the elastic properties of ROCK1:ER cells that were tagged with cofilin using AFM force spectroscopy. ROCK1 expression was of interest, as it has been shown to excessively express itself in pancreatic cancer, as opposed to ROCK2 (Kaneko et al., 2002). The ROCK1:ER cells were tagged with either red fluorescent protein (mcherry; control) or mcherry with cofilin type 1 (CFL1), as stated in Section 2.3.2. Again, the morphology of these cells was similar to each other (surface area of ROCK1:ER mcherry was 338.70 ± 113.22 μm$^2$ and ROCK1:ER CFL1 was 393.37 ± 181.53 μm$^2$; n = 80 cells), and to their parental cells (Figure 2.6 and Figure 2.10).

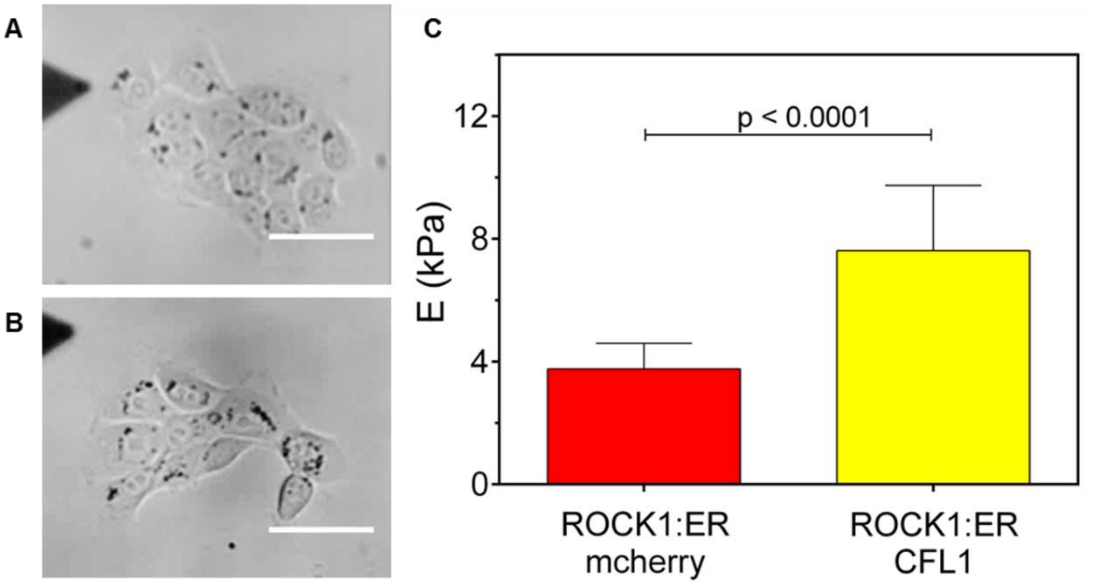

**Figure 2.10│Average elasticity measurements of PDAC p53 fl ROCK1:ER: mcherry; control, and cofilin cells (n = 80 cells), expressed as mean ± SD.** All scale bars are 30 μm. Cofilin activated cells presented to be significantly stiffer compared to the control ($p < 0.0001$).

CFL1 is a protein that can be widely distributed within a cell, which can depolymerise filamentous actin and inhibit the polymerisation of globular actin (actin monomer). The aforementioned ROCK activation inactivates ADF/cofilin activity and hence stabilises the actin cytoskeleton. Therefore activation of ADF/ cofilin should reorganise the actin cytoskeleton (Popow-Woźniak et al., 2012). For these cells, no external treatment was needed as an active CFL1 plasmid was inserted into one set of ROCK1:ER cells, whilst the other contained only the fluorescent protein.

The measured elastic modulus for CFL1 activated cells displayed stiffer characteristics compared to the control ($p < 0.0001$; Figure 2.10). For CFL1 activated cells, the average elasticity increased by 51%, from 7.65 ± 2.19 kPa for the activated cells to 3.77 ± 0.84 kPa for the control cells. These findings were in good agreement with cofilin activated breast cancer cells, which also showed an increase in cell elasticity (Cameron et al., 2015). Together, through measuring the mechanical response from overexpression of ROCK1 (reduction in elasticity of 57%), and cofilin activation, we have shown that the inactivated cofilin activity in ROCK may be the major contributor to the overall cell behaviour for overexpressed ROCK1:ER cells. However, it is unclear to what degree actin contraction contributes to the overall cell behaviour too.

Prior to understanding how actin contraction contributes to overexpressed ROCK cells, we observed the effect of elasticity on overexpressed ROCK cells when LIM kinases were inhibited. This investigation could confirm the observations on cofilin activated cells and give the added information about whether cells fully returned to their original state. Using EGFP:ER and ROCK1:ER cells, these cells were estrogen treated to overexpress ROCK1, and later inhibited with 12 μM of BMS-5 (LIM kinase inhibitor), which was added to the estrogen media. This inhibitor inhibits both LIM kinase 1 and 2.

As seen previously, the overexpressed ROCK1:ER cells exhibited a reduced elastic behaviour compared to control and untreated cells (Figure 2.11). Following LIM kinase inhibition, it was shown that the elastic modulus increased by 36%, from 0.98 ± 0.12 kPa for overexpressed ROCK1:ER cells to 1.54 ± 0.31 kPa for overexpressed ROCK1:ER + BMS-5 cells.

The inhibition of LIM kinases may return the elastic properties of ROCK1:ER cells back to the values they had when untreated ($E = 1.63 \pm 0.31$ kPa). However, although the ROCK1:ER cells increased in elasticity with LIM kinase inhibitor, there were significant differences between the two populations of cells (estrogen + BMS-5 treated and untreated). This information, in turn indicates the presence of another factor that could contribute to the overall mechanical response of overexpressed ROCK1 activity ($p < 0.0001$).

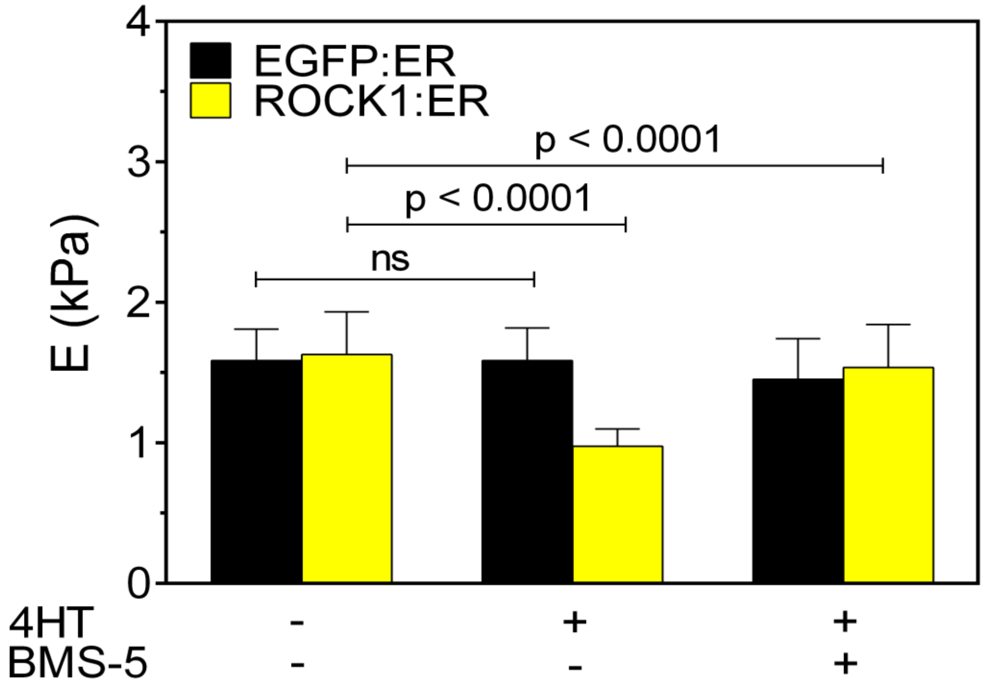

**Figure 2.11│Average elasticity measurements of PDAC p53 fl+ ROCK1:ER relative to GFP:ER following 4HT and BMS-5 treatment (n = 80 cells), expressed as mean ± SD.** Although activated ROCK1:ER cells were softer compared to EGFP:ER ($p < 0.0001$), the cells returned to its original stiffness with LIM kinase inhibitor.

To address the effect of actin contraction on the elastic response of the cell, we measured the elasticity of overexpressed ROCK1:ER cells that were tagged with MLC and MLC AA (Figure 2.12).

The cells were transfected according to the method stated in Section 2.3.2. The method of transfection was transient, which meant that the modification was not stable and the tagged proteins may not have been present when measurements were taken. Therefore, as an added precaution we applied the normal estrogen treatment to one set of the cells, and to another we applied an ethanol treatment (1 µM). The reason for ethanol treatment was that the estrogen was diluted in ethanol before being placed in the media; this should provide a good control to indicate if the transfection had worked.

From the untreated cells, the average elasticity increased by 61% and 47%, for overexpressed ROCK1:ER + MLC AA and overexpressed ROCK1:ER + MLC cells, as respectively ($p < 0.0001$). In comparison to the ethanol treated cells, the overexpressed ROCK1:ER + MLC cells were not significantly different from each other; 5.18 ± 2.89 kPa for estrogen treated cells and 4.80 ± 1.38 kPa for the ethanol treated cells. In addition, there was no significant difference between the two ethanol treated sets of cells; as stated above for overexpressed ROCK1:ER + MLC + ethanol the modulus was 4.80 ± 1.38 kPa and it was found to be 4.54 ± 1.94 kPa for overexpressed ROCK1:ER + MLC AA + ethanol.

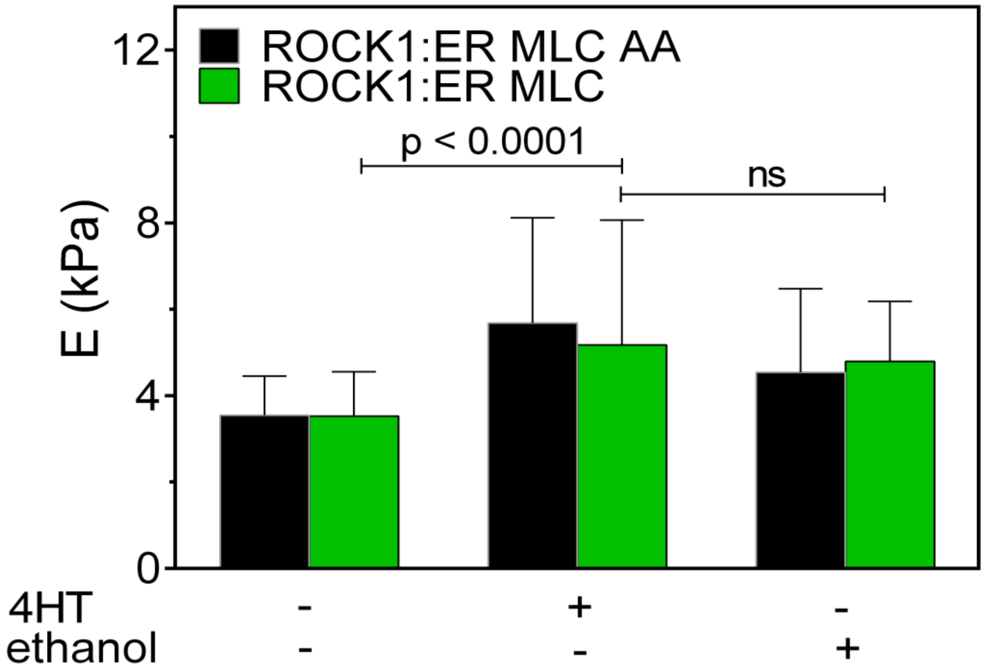

**Figure 2.12│Average elasticity measurements of PDAC p53 fl+ ROCK1:ER MLC and counterpart MLC AA cells following 4HT or ethanol treatment (n = 80 cells), expressed as mean ± SD.** MLC on overexpressed ROCK1 caused an increase in stiffness though similar effect was seen in ethanol and MLC AA cells ($p < 0.0001$).

These results suggested that the cells had lost the tagged proteins within the timescale over which the measurements were performed. The reason for this conclusion was that cells that had been estrogen treated (overexpressed in ROCK1) were found to be similar to the ethanol treated cells (normal levels of ROCK). To support such a statement, we carried out fluorescence imaging on these cells to identify whether the tagged fluorescent protein (mcherry) was still present. Fluorescence microscopy was performed with a Cy5 filter (XF102-2; Omega Optical) and each set of modified cells (ROCK1:ER + MLC and + MLC AA) were exposed for 0.02 seconds (Figure 2.13).

From the images, it was found that there was no mcherry expression in the ROCK1:ER + MLC AA cells and the same was true for majority of the ROCK1:ER MLC cells. Based on these observations along with the outcome of the elastic data, there was reasonable doubt that the measured elasticity was a good representation of the effects of actin contraction, due to the loss of the proteins.

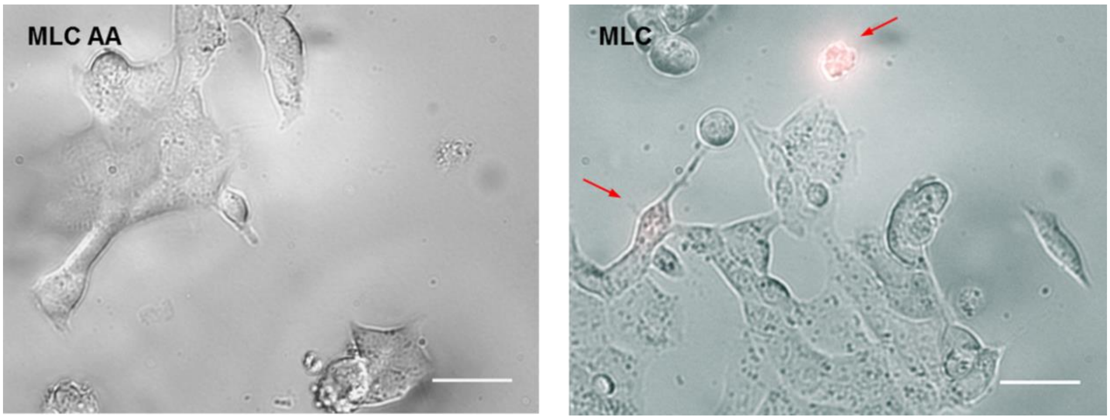

**Figure 2.13│Fluorescent image of PDAC p53 fl+ mcherry MLC and MLC AA cells showing the amount of expressed mcherry.** Scale bar showing 100 μm. The red arrows indicating the mcherry expressed.

Thus another approach was taken to investigate the effects of actin contraction. This involved recognising the effect on actin contraction when a small molecule inhibits myosin II activity, known as blebbistatin, is included in the culture media. In this investigation, the elastic responses of EGFP:ER and ROCK1:ER cells with and without blebbistatin treatment were compared (Figure 2.14).

Firstly, it was observed that the morphologies of EGFP:ER and ROCK1:ER cells treated with media containing both estrogen (1 μM) and blebbistatin (5 μM) were different compared to those where only estrogen was added to the media (Figure 2.6 and Figure 2.14). The effect of blebbistatin caused both cells to collapse in structure, which would be due to the loss of cytoskeletal tension. Blebbistatin targets all myosin II activity, which is regulated by two main signalling pathways; ROCK and MLCK (Martens and Radmacher, 2008). As the inhibitor is not specifically targeted to ROCK activated myosin, this in turn clarifies why blebbistatin affected both types of cell as opposed to only those with overexpressed ROCK1 activity.

Both EGFP:ER and ROCK1:ER cells exhibited softer elastic properties when treated with blebbistatin. An average reduction in elastic modulus was observed of 35% and 34% for EGFP:ER and ROCK1:ER cells, respectively. It was also found that there was no significant difference between the two cell lines. Together, observations of the cells' morphology and elastic behaviour have shown that in both types of cells actin contraction is inhibited in the same way.

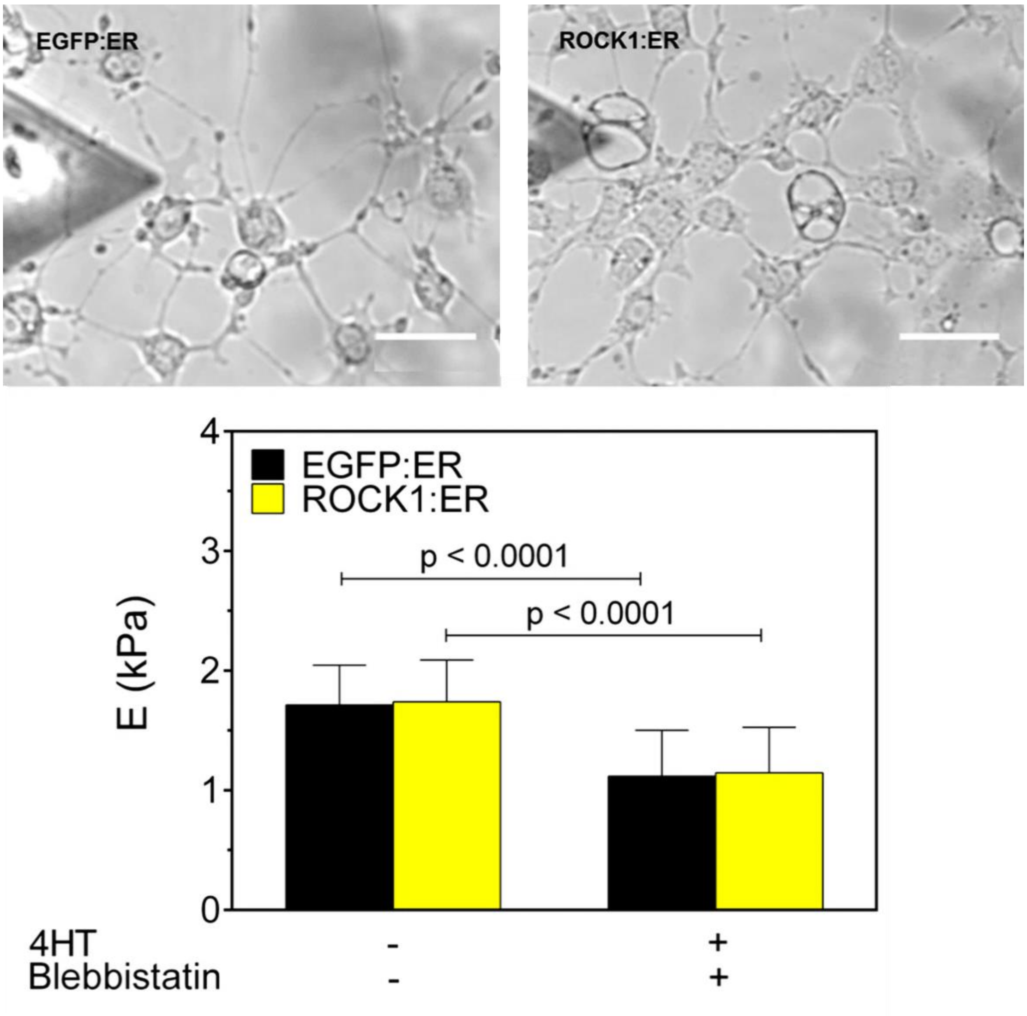

**Figure 2.14│The comparison between PDAC p53 fl+ ROCK1:ER relative to EGFP:ER cells in the presence of blebbistatin treatment.** All scale bars are 30 μm. The graph was expressed as mean ± SD from 80 cells. Both EGFP:ER and ROCK1:ER cells exhibited decrease in elasticity with blebbistatin treatment ($p < 0.0001$).

Here, we have revealed that ADF/cofilin activity within the cells largely contributes towards the overall mechanical response for overexpressed ROCK1 activity. This is in agreement Kole *et al.*, which showed that entangled actin networks and bundles dominated intracellular stiffening, as oppose to actomyosin contractility and the formation of focal adhesions (Kole et al., 2004). Although we were unable to see the effect of ROCK activated actin contraction, it was observed that inhibiting all the myosin II within the cell did reduce cellular stiffness.

## 2.5 Conclusions

We have investigated the effect of overexpression of ROCK activity on mechanical properties of cells in colonies by AFM force spectroscopy. ROCK activation in cells was shown to provide stable actin cytoskeleton, and generate actomyosin contractions. The results showed that overexpression of ROCK activity led to softening of the cells. Furthermore, it changed the actin arrangement from dense actin bundles around the nucleus to actin bundles mainly situated at the periphery of the cell. By combining the elastic behaviour to the observed actin structures, the cells' behaviour is possibly connected to the inward stresses generated by actomyosin contraction, exerted on cells in colonies. It was further noticed that ADF/cofilin activity contributes to majority of the cell response in overexpressed ROCK activity. As we have shown that PDAC cells do not follow the conventional pattern, it remains unclear how the overexpressed ROCK activity completely influences the cell mechanics, in relation to cell invasion. Hence, future investigations should focus on understanding how other parts of the cells, ROCK activated myosin and substrate influence could also affect the overall mechanical behaviour that occurs with overexpression of ROCK activity.

# Chapter 3 Cell Viscoelasticity

## 3.1 Abstract

The study of cell mechanics using atomic force microscope (AFM) has been evolving for decades, from collecting simple cell stiffness values to obtaining complex viscoelastic properties. Although there have been advances in the field of cell mechanics, the existing methods for viscoelastic measurements contain limitations and cannot be applied over a wide range of frequencies. To address this situation, we developed a novel methodology, namely, Fourier transform-AFM-microrheology (FT-AFM-M). This method generates the viscoelastic properties of cells across a significantly wider frequency range than can be obtained from single experiments using other techniques. Initially, the FT-AFM-M method was validated using traditional rheometer measurements on various complex materials. We then went on to use this method to uncover subtle mechanical behaviour changes within a variety of cancer cells, over more than five decades of frequency (0.005–2400 Hz). In this chapter, we have used pancreatic ductal adenocarcinoma cells, to investigate the change in viscoelastic properties with morphology, deletion of the TP53 gene and the overexpression of Rho kinase, all of which have a relation to cell invasiveness. The results showed that stretched cells exhibited ~44% increase in *G'* (elasticity) and 25–68% increase in G'' (viscosity) compared to the rounded cells on patterned surfaces, over the accessible frequency spectrum. These observations were seen in both in mutant p53 (stretched) and deleted p53 cells (rounded), where their morphologies changed in a similar manner. In the absence of this morphology difference, overexpression of ROCK led to a reduction in the elastic behaviour by ~25%, while the viscous properties remained constant. Overall, we have shown that cells generally exhibit a soft glassy behaviour; hence the elastic characteristic is dominant within a cell. The invasive cells have shown to transition from soft glassy behaviour to viscoelastic behaviour earlier than non-invasive cells. This transition means that cells become more fluid-like, as the viscous characteristics become dominant within the cell. However, to fully understand the mechanical response of cancer cells in their physiological conditions, further investigations

under other conditions will have to be performed. However, this new procedure will aid in providing the best overview of information regarding a cell's viscoelastic behaviour.

## 3.2 Introduction

Living cells are known to be complex materials, behaving both as an elastic solid and as a viscous fluid. This means that cells do not fully fit within classical models that account for either elasticity or viscosity; this is because the main assumption of these models is that the materials are homogeneous, and this clearly does not apply to biological cells as these are dynamic. Furthermore, the presence of hysteresis (the phenomenon that the system's prior history influences the current and future internal states) between loading and unloading indentation curves indicates that the mechanical properties of cells are complex.

Cells are a combination of a high water content fluid with a structural biopolymer matrix. The majority of the fluid is made up of cytosol. This fluid coexists with solid phases that are composed of proteins, DNA, RNA and cytoskeleton filaments as well as organelles. The collection of solid and liquid phases within the region between the nucleus and the plasma membrane is known as the cytoplasm. The viscosity of the cytoplasm controls the shape, transport and movement of macromolecules within the cell. The cell's overall elasticity can govern the movement of different elements on different timescales. For instance, it controls the response of the cytoplasm to external stresses within seconds; the organelles and cytoskeleton elements move over a period of a few minutes, and the contractile mechanical organisation can occur on even longer timescales (Bhat et al., 2012).

To fully understand the mechanical response of cells and its complexity, the viscoelastic properties (rheology) has been studied (Zhu et al., 2000). This property corresponds to both storage (elastic portion; *G'*) and loss (viscous portion; *G''*) processes that occur during deformation. For a solid, the elastic characteristics can be defined as the ratio of stress and strain, however for a viscous fluid, the deformation under external stresses changes with time. Hence, fluid viscosity is the ratio of stress to strain rate (change of strain over time). In a complex material, *G'* is the ability of a material to store energy and release it after deformation (in a time dependant manner), while *G''* is the energy dissipated due to internal friction during deformation (again, this dissipation may occur with different time constants, depending on the bodies and processes involved) (Étienne and Duperray, 2011; Meyers and Chawla, 1999).

The main techniques that are routinely used to measure the cell's viscoelasticity are micropipette aspiration, magnetic twisting cytometry, optical tweezers, AFM and particle tracking microrheology (full details reviewed in Section 1.4). Among these techniques, AFM is the method with the highest spatial resolution. Typically, it can impose forces that are in the range appropriate for studying eukaryotic cells (piconewton to micronewton). It also has the ability to examine live cells under physiological conditions. The current approaches employed to measure time-dependent mechanical properties with AFM include creep tests, stress relaxation tests, acoustic methods and multifrequency AFM (Chyasnavichyus et al., 2015).

In the time domain, measurements can be made using creep or stress relaxation tests. For creep tests, the AFM cantilever probe is indented into the sample producing a cantilever deflection (load). The deflection is kept constant by a closed feedback loop, which only moves the cantilever base whilst the tip moves freely, as the sample surface relaxes. In stress relaxation tests, the cantilever is indented into the sample and maintained at a constant deformation, while the deflection force is monitored. For a complex material, creep compliance is when the material experiences an increase in strain under constant stress. Here, stress relaxation occurs when stress decreases even though there is a constant strain applied (Desprat et al., 2005; Moreno-Flores et al., 2010). Both creep and stress relaxation experiments have been used to measure the viscoelastic properties of live bacteria (Vadillo-Rodriguez et al., 2008) and eukaryotic cells (Desprat et al., 2005; Hiratsuka et al., 2009; Moreno-Flores et al., 2010; Wu et al., 1998), under physiological conditions.

In the frequency domain, measurements can be made by observing small amplitude sinusoidal oscillations of the cantilever that is in contact with the sample, at various frequencies. This can be accomplished using several instrumental modes that can be applied to the AFM; these include force modulation mode (FMM), contact resonance force mode (CRFM) and a multifrequency mode. In FMM experiments, in addition to the conventional AFM setup a sinusoidal signal is added to either the tip or the sample's piezo's, whilst the z-feedback loop maintains a constant cantilever deflection. The amplitude and phase components of the measured AC signal are used to study the elastic properties of the surface. (Radmacher et al., 1993). In contrast, CRFM uses resonance frequencies (where the forced motion is coherent with an oscillatory frequency) and mechanical quality factors of the cantilever, to measure the difference when the tip is above and in contact with the sample (Churnside et al., 2015; Yuya et al., 2008). A multifrequency measurement is the process that involves simultaneously having two or more natural frequencies driven by sinusoidal base excitation of the cantilever. Using amplitude and frequency modulation of the frequencies, it is possible to extract both frequency shifts and amplitude differences for the vibrations, and thus the mechanical parameters of tip-sample contact (Chawla and Solares, 2011; Sunyer et al., 2009).

For each technique, the measured data from either a time or frequency domain approach can be interpreted via several ways to extract their time-dependent properties. These approaches will be discussed in detail in the next subsection.

## 3.3 Approaches to describe viscoelastic behaviour

The collected data can be analysed with one of the following approaches; the spring and dashpot models, power-law model or frequency dependent stress-strain representation. Within this section, we will discuss how the viscoelastic properties can be calculated from the data, and the advantages and disadvantages for each procedure.

There will be several equations discussed below, for ease a table with a list of symbols and their definitions were compiled (Table 3.1).

**Table 3.1│A list of symbols with their definitions.**

| Symbol | Name |
|---|---|
| $\sigma_s$ | stress of the spring |
| $E$ | Young's modulus (elasticity) |
| $\varepsilon_s$ | strain of the spring |
| $\sigma_d$ | stress of the dashpot |
| $\mu$ | Viscosity |

| | |
|---|---|
| $d\varepsilon_d/dt$ | strain rate of the dashpot (change of strain over time) |
| $\dot{\sigma}$ | stress rate; $d\sigma/dt$ |
| $\dot{\varepsilon}$ | strain rate; $d\varepsilon/dt$ |
| $E_1$ | modulus of the spring alone for standard linear solid (SLS) model |
| $E_2$ | modulus of the spring in series with the dashpot for SLS model |
| $\sigma$ | Stress |
| $\varepsilon_0$ | oscillatory strain |
| $\sigma_0$ | amplitude of the stress function |
| $t$ | Time |
| $\tau$ | characteristic time constant/ time variable |
| $\omega$ | angular frequency |
| $G^*$ | complex modulus |
| $G'$ | storage modulus |
| $G''$ | loss modulus |
| $i$ | imaginary number, i, the square root of -1 |
| $\beta$ | power-law exponent |
| $\eta$ | structural damping coefficient |
| $G_0$, $\omega_0$ | scaling factor |
| $\Gamma$ | gamma function (all complex numbers) |
| $\varphi$ | phase lag |
| $\upsilon$ | Poisson’s ratio |
| $R$ | radius of the indenter probe |
| $\delta_0$ | operating indentation |
| $F$ | force |
| $\delta(\omega)$ | indentation oscillations |
| $b$ | drag factor depending on the height from the cell surface |
| $G_\alpha(t-\tau)$ | relaxation modulus |
| $E_0$ | elasticity at a random chosen time |

| | |
|---|---|
| $t_0$, $t'_0$ | normalised timescales |
| $G(t)$ | reduced relaxation function |
| $T^{(e)}(\delta)$ | instantaneous elastic response that is a function of indentation |
| $\delta$ | Indentation |
| $\partial\delta(\tau)$ | small change of indentation on a material at an instant of time |
| ‘ $\dot{}$ ’ | denotes the rate of change with time |
| ‘ $\widehat{}$ ’ | denotes Fourier transform |
| $\hat{G}(\omega)$ | Fourier transformation of the material’s shear modulus |
| $\hat{F}(\omega)$ | Fourier transformation the force applied during deformation |
| $\widehat{T^{(e)}}(\omega)$ | Fourier transformation of the elastic response |

### 3.3.1 Spring and dashpot models

The data collected via the time domain can be modelled with a collection of springs and dashpots arranged in series or parallel, to obtain the linear viscoelastic behaviour of a material (Kollmannsberger and Fabry, 2011). The Maxwell model was first proposed in 1867, whereby the model was presented by two elements in series; a purely elastic spring and a purely viscous damper (Figure 3.1). The spring obeys Hooke’s law, so stress is proportional to strain: $\sigma_s = E\varepsilon_s$; the dashpot can be described as an element where stress is proportional to strain rate: $\sigma_d = \mu\, d\varepsilon_d/dt$. Another configuration between the spring and dashpot, known as the Kelvin-Voigt model arranges these two elements in parallel instead. Solares *et al.* has noted that the Maxwell model best describes stress relaxation with high accuracy, while the Kelvin-Voigt model best describes creep compliance (Solares, 2014). This is because the surface in a creep system lacks a spring to accommodate for the instant force applied, and lacks the existence of a mechanism for surface recovery (López-Guerra and Solares, 2014).

In the Maxwell model, the overall strain is the addition of strain of the spring and strain of the dashpot, while the stress is the same for all elements. This means that the strain rate for the Maxwell model can be written as: $\dot{\varepsilon} = \dot{\sigma}/E + \sigma/\mu$ (where the rate of change with time is denoted by the symbol ‘ $\dot{}$ ’) (Vincent, 2012). In a stress relaxation experiment, the strain is constant, thus strain rate equals to zero, and the stress decays exponentially with a characteristic time constant; $\tau = \mu/E$. Therefore the equation for stress can be written as: $\sigma = \sigma_0 exp(-t/\tau)$.

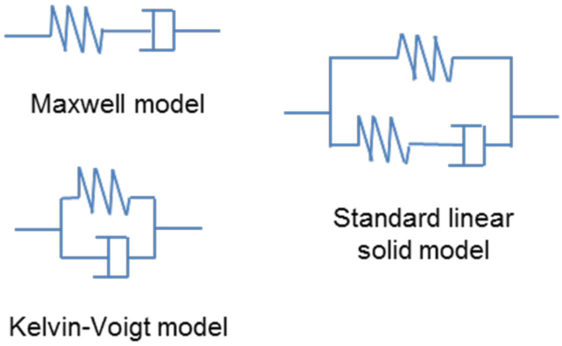

**Figure 3.1│Sketches of the spring and dashpot models.**

In the Kelvin-Voigt model, the overall stress is the addition of the stress of the spring and the stress of the dashpot, while the strain is the same for all elements. This means that the stress and strain rate for the Kevin-Voigt model can be written as: $\sigma = E\varepsilon + \mu\dot{\varepsilon}$ and $\dot{\varepsilon} = \sigma/\mu - E\varepsilon/\mu$, respectively (Vincent, 2012). In a creep experiment, the stress is constant, thus the stress always equals the initial stress, the stress rate is equal to zero, and the strain decays exponentially with $\tau$; this means the equation for strain can be written as: $\varepsilon = \varepsilon_0 exp(-t/\tau)$.

To describe creep compliance and stress relaxation, a model with the combination of Maxwell and Kelvin-Voigt models was developed, which is known as the SLS (standard linear solid) model (Figure 3.1). Within the model, the stress relaxes through the dashpot located in the series Maxwell, but some of the stress can be stored in the parallel spring. In the SLS model, the strain rate can be defined as: $\dot{\varepsilon} = (E_1 + E_2)^{-1}(\dot{\sigma} + E_2\sigma/\mu - E_1E_2\varepsilon/\mu)$, where $E_1$ is the modulus of the spring alone, and $E_2$ is the modulus of the spring that is in series with the dashpot (Chester, 2012). Applying a sudden constant strain or a sudden constant stress to a viscoelastic material with characteristic time constant, $\tau$, the stress and strain for stress relaxation or creep compliance response can be written as

$$\sigma = \varepsilon_0\left(E_1 + E_2 exp^{\frac{E_2}{\mu}t}\right) \qquad \varepsilon = \frac{\sigma_0}{E_1}\left(1 - \frac{E_2}{E_1+E_2}exp^{\frac{E_1E_2}{(E_2+E_1)\mu}t}\right) \qquad (3.1)$$

Hence, the complex modulus of a material can be solved as

$$G' = \frac{E_1{E_2}^2+(E_1+E_2)\mu^2\omega^2}{{E_2}^2+\mu^2\omega^2} \qquad G'' = \frac{{E_2}^2\mu\omega}{{E_2}^2+\mu^2\omega^2} \qquad (3.2)$$

where $\omega$ is the angular frequency, *G'* is storage modulus, and *G"* is loss modulus. There are more complex spring and dashpot models that have been extensively reviewed (López-Guerra and Solares, 2014). These models are good for interpreting time domain data to describe a viscoelastic material. However, when there are multiple unknown parameters such as a number of relaxation times (to produce a preconceived model), application of these models to measured data could produce large fitting errors (Grant et al., 2013; López-Guerra and Solares, 2014).

### 3.3.2 Power-law models

Power-law modelling was pioneered by Scott-Blair, to achieve properties from data collected in the frequency domain (Jaishankar and McKinley, 2013). There are different formulations of power-law models that include structural damping and rheology. The power-law structural damping model defines the complex shear ($G^*$) model as (Alcaraz et al., 2003)

$$G^*(\omega) = G' + iG'' \tag{3.3}$$

$$= G_0 \left(\frac{\omega}{\omega_0}\right)^{\beta} (1 + i\eta)\Gamma(1-\beta)\cos\left(\frac{\beta\pi}{2}\right) + i\omega\mu \tag{3.4}$$

where $\beta$ is the power-law exponent, $\eta$ is the structural damping coefficient that can be given by $G''/G' = \tan(\beta\pi/2)$ $G_0$ and $\omega_0$ are scaling factors. $\Gamma$ is the gamma function. This model can be applied to AFM indentation to measure $G^*$ using the relationship: (Lim et al., 2006; Roca-Cusachs et al., 2006)

$$G^* = \frac{1-\upsilon}{4(R\delta_0)^{1/2}}\left(\frac{F(\omega)}{\delta(\omega)} - i\omega b(0)\right) \tag{3.5}$$

where $\upsilon$ is the Poisson's ratio, $R$ is the radius of the indenter probe, $\delta_0$ is the operating indentation, $\delta(\omega)$ is the indentation oscillation function, $b$ is a drag factor depending on the height from the cell surface and expressed as $b(0)$ at contact.

A second power law approach has been termed power-law rheology. This has also been used in combination with AFM to measure the rheology of living cells (Kollmannsberger and Fabry, 2011). The creep and stress relaxation responses of these cells were written in the form of

$$\varepsilon(t) = \frac{\sigma_0}{E_0\left(\frac{t}{t_0}\right)^{\beta}} \qquad \sigma(t) = E_0\varepsilon_0\left(\frac{t}{t'_0}\right)^{\beta} \tag{3.6}$$

where $E_0$ is the elasticity at a randomly chosen time, $t_0$ and $t'_0$ are normalised timescales that can also be chosen randomly. Using these equations, a non-exponential relaxation process can be described with small number of parameters. Here, the response of a complex material to dynamic loading follows a power law giving

$$|G^*(\omega)| = \sqrt{\left(G'(\omega)\right)^2 + \left(G''(\omega)\right)^2}$$

$$\sim \omega^{\beta} \tag{3.7}$$

This approach has provided information on the dynamics of the elastic structures within the cell under deformation (Lange and Fabry, 2013). When a material exhibits properties of a purely elastic solid, $\beta$ = 0, and when a purely viscous fluid, $\beta$ = 1. An example of this is applicable to biological cells is where an increase in the value of $\beta$ corresponds to the response following actin disruption. Typically the $\beta$ value for cells falls below 0.5 (Kollmannsberger and Fabry, 2011). The main advantage of this approach is that it is simple method to describe the viscoelastic response of a material. However, this model cannot describe plateau regions within the frequency domain, which means that highly elastic properties are uncounted for.

### 3.3.3 Frequency dependent stress-strain representation

Oscillations imposed and/or measured on living cells using AFM can be represented by simple stress and strain formulae to express the viscoelastic behaviour of cells. If the time selected corresponds with a time at which the strain passes through its maximum, the response of stress is the same as strain but with a phase lag ($\varphi$)

$$\varepsilon(t) = \varepsilon_0 \sin \omega t \qquad \sigma(t) = \sigma_0 \sin \omega t + \varphi \tag{3.8}$$

The stress-strain relationship for a linear isotropic material can be written in the time domain as (Fung, 1993)

$$\sigma(t) = \int_{-\infty}^{t} G_{\alpha}(t-\tau)\frac{d\varepsilon}{d\tau}d\tau \tag{3.9}$$

where $d\varepsilon/dt$ is the shear rate and $G_{\alpha}(t-\tau)$ is the relaxation modulus describing both the deviatoric (change of shape; $\alpha = 1$) and the dilatational (change of volume; $\alpha = 2$) parts of the stress-strain relationship. The strain (Equation 3.8) can be substituted into Equation 3.9, to give the stress-strain relationship in terms of *G'* and *G"* as (Moeendarbary and Harris, 2014)

$$\sigma(t) = \varepsilon_0\left[\omega \int_0^\infty G(\tau)\sin\omega\tau\, d\tau\right]\sin\omega t + \varepsilon_0\left[\omega \int_0^\infty G(\tau)\cos\omega\tau\, d\tau\right]\cos\omega t$$

$$= \varepsilon_0 G' \sin\omega t + \varepsilon_0 G'' \cos\omega t \qquad (3.10)$$

For a purely elastic material, stress is in phase with the strain, thus $G' = G$, $G'' = 0$, and $|G^*| = G$. On the other hand, for a purely viscous material $G' = 0$, therefore the stress response has a phase lag of $\pi/2$ with strain and $G'' = |G^*| = \mu\omega$. A viscoelastic material exhibits both elastic and viscous properties and conventionally the phase lag $(0 < \varphi < \pi/2)$ is given at that between the applied strain and the resultant stress. Using Equation 3.10, the frequency-dependent of *G'* and *G"* for a material can be given as (Moeendarbary and Harris, 2014)

$$G' = \frac{\sigma_0}{\varepsilon_0}\cos\varphi \qquad G'' = \frac{\sigma_0}{\varepsilon_0}\sin\varphi \qquad (3.11)$$

The approach of imposing oscillations on the cells can only provide discrete viscoelastic values at given frequencies. In addition, there are many environmental effects when measurements are carried out in liquid. Within a liquid environment, the cantilever cannot be excited without piezoelectric excitation that could lead to damping effects in the cantilever and added mass effects from the liquid (Churnside et al., 2015).

To overcome these limitations, we have developed a new approach whereby the time-dependent stress relaxation data are analysed via Fourier transformation of the convolutional integral between force and indentation (fully outlined in Section 3.4). This approach does not require fitting of data to one of the models described above but nevertheless provides both storage and loss moduli over a continuous frequency domain. Obtaining this continuous frequency spectrum is important in the study of cells and biomaterials, since these bio-samples are constantly changing upon constant compression, no information would be lost like discrete measurements (Tripathy and Berger, 2009).

## 3.4 Fourier transform-AFM-microrheology

The FT-AFM-M analysis has been developed by following the same principles adopted by Tassieri *et al*. for deducing the materials' linear viscoelastic properties over the widest range of experimentally accessible frequencies from a simple time-dependent step-strain measurement (Tassieri et al., 2016). A feature of this method is that it does not rely on the need for preconceived models of the cell response nor the idealisation of real measurements. This has been achieved by evaluating the Fourier transforms of raw experimental data describing both the time-dependent stress and strain functions by means of the analytical method introduced by Tassieri et al. (Tassieri et al., 2012). In the original development of this method, particle trajectory data from optical tweezer measurements were used in the calculations. Thus here it was necessary for us to make modifications to the original algorithm in order to use the uniaxial compression data that comes from AFM measurements. These modifications also accounted for indenter properties such as the indenter probe radius and tip-sample contact area; hence a partial preconceived model (Hertzian model) has been used.

Using the model introduced by Fung *et al.* known as quasi-linear viscoelasticity, and the force-indentation data collected from the AFM, we can describe the material's stress response (relaxation function; $K(\delta, t)$) as (Fung, 1993)

$$K(\delta, t) = G(t)T^{(e)}(\delta) \tag{3.12}$$

where $G(t)$ is the reduced relaxation function (shear modulus) (a normalised function of time), and $T^{(e)}(\delta)$ is the instantaneous elastic response that is a function of indentation. In this equation, $G(t)$ expresses the material's history of relaxation behaviour, so for an elastic solid with a response that is independent of its history, $G(0) = 1$. In this case, the material's stress response is equal to $T^{(e)}(\delta)$.

Generally, the instantaneous elastic response of a material can be calculated by Hertzian contact model (Puttock and Thwaite, 1969). Using a rigid spherical indenter on an incompressible linearly elastic half-space model, this is given by

$$T^{(e)}(\delta) = F(\delta) = \frac{16}{9}E\sqrt{R\delta^3} \tag{3.13}$$

where $R$ is the radius the indenter, $E$ is elastic modulus, and assuming for an incompressible material, the Poisson ratio is 0.5. For a complex material, the stress response to an infinitely small change of indentation ($\partial\delta(\tau)$) on a material in a state of deformation at an instant of time can be written as (Tripathy and Berger, 2009)

$$K(\delta, t) = G(t - \tau)\frac{T^{(e)}[\delta(\tau)]}{d\delta}d\delta(\tau) \quad t > \tau \tag{3.14}$$

These functions of time can be connected by a linear constitutive equation (Equation 3.9), which is based on the principle that the effects of sequential changes in strain are additive, thus

$$F(t) = \int_{-\infty}^{t} G(t-\tau)\frac{T^{(e)}[\delta(\tau)]}{d\delta}\frac{d\delta(\tau)}{d\tau}d\tau$$

$$= \int_{-\infty}^{t} G(t-\tau)\dot{T}^{(e)}(\tau)d\tau \tag{3.15}$$

where $\dot{T}^{(e)}(\tau)$ is the rate of change in elastic response with time. Using Equation 3.15, the integral can be resolved by Fourier transformation (to express a function of time into the angular frequency; denoted by the symbol ‘$\frown$’),

$$\hat{F}(\omega) = \int_{-\infty}^{\infty} F(t)\, exp^{-i\omega t}dt$$

$$= \int_{-\infty}^{\infty}\left[\int_{-\infty}^{\infty} G(t-\tau)\,\dot{T}^{(e)}(\tau)\,d\tau\right] exp^{-i\omega t}dt$$

$$= \left[\int_{-\infty}^{\infty} G(t-\tau)\, exp^{-i\omega t}dt\right]\int_{-\infty}^{\infty}\dot{T}^{(e)}(\tau)\,d\tau$$

$$= \int_{-\infty}^{\infty} G(t-\tau)exp^{-i\omega(t-\tau)}\,dt\int_{-\infty}^{\infty}\dot{T}^{(e)}(\tau)\,exp^{-i\omega\tau}d\tau$$

$$= \hat{G}(\omega)\int_{-\infty}^{\infty}\dot{T}^{(e)}(\tau)\,exp^{-i\omega\tau}d\tau \tag{3.16}$$

where $\hat{G}(\omega)$ is the Fourier transformation of the material's shear modulus. The latter integral can be determined using integration by parts where $u = exp^{-i\omega\tau}$ and its derivative is $du/dt = -i\omega exp^{-i\omega\tau}d\tau$, while $dv/d\tau = \dot{T}^{(e)}(\tau)d\tau$ and its integral is $v = T^{(e)}(\tau)$

$$\widehat{\dot{T}^{(e)}}(\omega) = \int_{-\infty}^{\infty}\dot{T}^{(e)}(\tau)exp^{-i\omega\tau}\,d\tau$$

$$= \left[T^{(e)}(\tau)exp^{-i\omega\tau}\,\right]_{-\infty}^{\infty} - -i\omega\int_{-\infty}^{\infty}T^{(e)}(\tau)exp^{-i\omega\tau}\;d\tau$$

$$= i\omega\,\widehat{T^{(e)}}(\omega) \tag{3.17}$$

The force-indentation relationship for a linear isotropic material that can be rewritten in terms of complex modulus, $G^{*}(\omega) = i\omega\, G(\omega)$ (Ferry, 1980)

$$\hat{F}(\omega) = \hat{G}(\omega)i\omega\,\widehat{T^{(e)}}(\omega)$$

$$= \frac{G^{*}(\omega)}{\cancel{i\omega}}\cancel{i\omega}\widehat{T^{(e)}}(\omega)$$

$$= \boldsymbol{G^{*}(\omega)\widehat{T^{(e)}}(\omega)} \tag{3.18}$$

The derived complex shear modulus from AFM acquired data can be equated with Equation 3.3, to give viscoelastic properties of a material

$$G^{*}(\omega) = \frac{\hat{\hat{F}}(\omega)}{\widehat{T^{(e)}}(\omega)} \tag{3.19}$$

$$= G'(\omega) + iG''(\omega)$$

In this subsection, we have shown how to take the stress relaxation data collected from the AFM in terms of force and indentation (time domain), to achieve storage and loss moduli (frequency domain). Each data point was included in the Fourier transforms to provide a set of continuous data over the frequency range and to maximise the frequency range over which the viscoelastic properties were calculated. Furthermore, to reduce possible artefacts, a high sampling rate was used.

## 3.5 Materials and Methods

### 3.5.1 Samples

The complex materials used for experimentation include gel pads with known stiffnesses (30 kPa and 100 kPa gel; ExCellness Biotech SA), multi-purpose tac (Niceday), and in-house made polydimethylsiloxane slabs (PDMS; 20:1 silicone elastomer to curing agent ratio; Dow Corning). The 20:1 PDMS was evenly mixed, degassed and baked for 2 hour at 70°C. All materials were kept at room temperature before use.

The cells under investigation included pancreatic ductal adenocarcinoma mutant p53 (PDAC p53 R172H), deleted p53 (PDAC p53 fl) cells, modified PDAC p53 fl cells tagged with enhanced green fluorescent-estrogen receptor protein (EGFP:ER), and PDAC p53 cells containing conditionally active ROCK1- or ROCK2-estrogen receptor fusion proteins isoforms (ROCK1:ER and ROCK2:ER). To overexpress the ROCK isoforms, 1 μM of 4-hyroxytamoxifen (4HT) was added to the culture medium.

### 3.5.2 Fabrication of cell pattern

To investigate the effect of cell shape on their viscoelastic properties, micropattern substrates were created to control the shape of PDAC p53 R172H cells. The micropattern consists of an array of 20 μm circles with 80 μm gaps on surface treated glass slides. Following the procedure developed earlier (Cuestas-Ayllon et al., 2012), the circular areas were modified with amino groups to promote cell adhesion, and the remaining areas were modified with polyethylene glycol (PEG) to prevent cell adhesion. The glass substrates were cleaned with various solvents (acetone, methanol, isopropyl alcohol) and piranha solution (3:1 sulfuric acid to hydrogen peroxide) before being submerged in 5% (3-aminopropyl)trimethoxy-silane in ethanol for 1 hour at room temperature. The treated substrates were spin-coated with S1805 positive resist (MicroChem Corp) at 4000 rpm for 30 seconds. These coated substrates were soft-baked for 10 minutes at 95°C, to evaporate any solvents from the resist and to dissipate any bubbles created during spin coating. When the substrates were ready, these were placed in the MA6 mask aligner (SUSS MicroTec) along with the photomask that contained the pattern features. The conditions for the machine were generally set to 'hard contact' (substrate and chrome mask in contact) during exposure and 50 μm gap for alignment, if necessary. Each substrate was exposed to the UV light from a 350 W mercury lamp (wavelength: 360 nm) for 4 seconds. To develop the exposed resist surfaces, a 1:2 dilution of MF-321 developer to distilled water was used for 45 seconds, and then rinsed in distilled water. The developed surfaces were fully dried using nitrogen gun before checked under an optical microscope, to ensure the complete removal of photoresist at the necessary regions. After the development of the photoresist, the surface was modified with 1% 2-[methoxy(polyethyleneoxy)propyl]-trichlorosilane in anhydrous toluene for 2 hours under vacuum to generate a PEG modified surface. The pattern slides were complete once the remaining photoresist was removed using dimethyl sulfoxide, exposing amino-groups terminated array areas. For storage, the patterned slides were kept under vacuum.

Prior to cell seeding, the slides were sterilised with ethanol and phosphate buffered saline (PBS) for 10 minutes each, at room temperature. A cell density of $1.08 \times 10^5$ cells/ $cm^2$ was seeded onto the substrates, and incubated for 2 hours at 37°C, with 5% carbon dioxide ($CO_2$), to allow the cell pattern to form. Once the majority of cells attached, the unsuspended cells were washed away with culture medium. The pattern cells were incubated for another 2 hours to enable cells fully attached.

### 3.5.3 Immunofluorescence staining

The patterned and unpatterned PDAC mutant p53 and deleted p53 cells were stained to highlight the actin filaments and nucleus after either 4 hours or overnight culturing at 37°C, with 5% $CO_2$ in a humidified incubator. The staining procedure involved washing the cells with PBS and fixing with 3.8% formaldehyde, 2% sucrose in PBS for 10 minutes at room temperature. The cells were then permeabilised with 0.1% triton X-100 in PBS for 10 minutes at room temperature, and blocked with 1% bovine serum albumin (BSA) in PBS for 30 minutes. The actin filaments were stained using phalloidin in BSA in PBS (1:500; Alexa Fluor® 488, Life Technologies) for 1 hour at room temperature. The stained cells were washed in 0.5% Tween 20 in PBS and mounted onto a coverslip using Vectashield mounting medium with DAPI (Vector Laboratories Inc.). Bright field and fluorescent images were collected using Zeiss Axiovert microscope. For fluorescent images, excitation filters of 340 ± 10 nm (blue, DAPI) and 485 ± 10 nm (green, FITC) were used for the two stains.

### 3.5.4 Stress relaxation

This procedure was carried out using a NanoWizard II AFM mounted on a Zeiss AxioObserver A10 inverted optical microscope. In-house fabricated spherical probed cantilevers (McPhee et al., 2010) with the appropriate spring constant were used for the measurements: ~ 3 N/m (FESP; Bruker) for complex materials and ~ 0.03 N/m (arrow TL-1; NanoWorld) for live cells. The size of the probe was dependent on the tip-surface contact area of the sample in which the cantilever was approaching towards; larger the probe, larger the area (20 μm, 10 μm and 4.74 μm probes for complex gels, complex materials and living cells, respectively). Cantilever calibration measurements were performed before and after each experiment using an analysis of the natural thermal tip vibrations in air at room temperature (Hutter and Bechhoefer, 1993). Each sample was subjected to at least one stress-relaxation experiment. The non-cell materials were placed on stage and measured in air at room temperature. The cells were placed on a heater stage and measured in (4-(2-hydroxyethyl)-1-piperazineethanesulfonic acid (HEPES) buffered media at 37°C.

Measurements were made by positioning the probe above the sample's surface for t = 10 s, to determine any forces that could lead to small drifts in the cantilever deflection. The stress (force) relaxation was then measured when the indenter was held at a constant indentation distance into the sample (Figure 3.2). This distance complied with the conditions for which Hertzian model is valid i.e. when <10% of the sample's thickness is indented. An indentation of ~ 0.8 µm, 3 µm, 1.3 µm and 0.5 µm was applied to 30 kPa/ 100 kPa gels, 20:1 PDMS, multi-purpose tac and cells, as respectively. All indentations were applied to the samples at a constant loading rate. A range of loading rates (3–100 µm/s) and the holding times (1 s and 30 s) were examined to study whether they affected the measurements of viscoelastic properties of the samples. However if not specified in the discussion, the loading rate and time were typically 10 µm/s and 30 s.

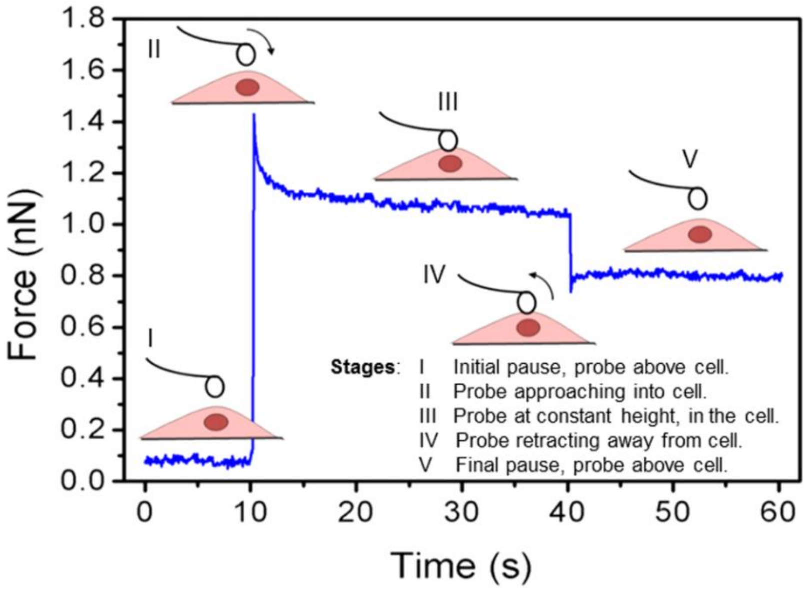

**Figure 3.2│Schematic diagram of the experimental procedure carried out for FT-AFM-M.**

After the indentation, the cantilever was retracted away from the indentation spot and kept stationary for t = 20 s, so the sample could recover to its original position. For each stage of the procedure, the deflection force and indentation data were collected at a sample rate of 16 kHz (16000 data points per second). For the complex materials, 4 randomly chosen areas on a sample were measured, while for each cell line, 50 cells from throughout the culture area were probed in the above manner. The data was analysed using an in-house Labview algorithm (see

Section 3.4). The viscoelastic data (*G'* or *G''*) was presented in a log-log graph against frequency ($\omega = 2\pi f$).

### 3.5.5 Bulk rheology

Oscillatory measurements were conducted with a modular compact rheometer, MCR 302 (Anton Paar) using a parallel plate tool of a diameter, 25 mm (PP25; Anton Paar). Calibrations of the motor and the system were carried out prior to measurements of the samples. The motor was calibrated by rotating the tool when force is equal to zero (in air) at a speed of 0.3 revolution/ min for 3 minutes followed by another 14 minutes calibration. Once the motor was calibrated, the system was calibrated by looking at the inertia (uniform motion unless changed by an external force), which is related to the mass of the tool. All calibrations were complete when a constant torque (-0.05 to 0.05 µNm) was displayed against deflection angle at a fixed speed of 0.3 revolution/ min. A frequency sweep was carried out on all complex materials, to measure *G'* and *G''* over an angular frequency range between $0.1 < \omega < 100$ rad/s, at a strain of 1%. These were performed at room temperature.

## 3.6 Results and Discussion

### 3.6.1 Establishment of FT-AFM-M

#### *3.6.1.1 The FT-AFM-M procedure*

Figure 3.3 shows the front panel of the Labview algorithm for FT-AFM-M that performs the analytical method, to calculate the Fourier transforms of both the measured force and indentation functions and therefore obtain the material's complex modulus with Equation 3.19.

In detail, the algorithm reads the experimental raw data (i.e. $[t, F, \delta]$) in the form of a tab-separated.txt file. Once Labview computed in raw data, the measured indentation was taken aside and corrected for the geometry of the indenter used via Equation 3.13. Then both force and corrected indentations were processed to calculate the viscoelastic moduli of the material under investigation.

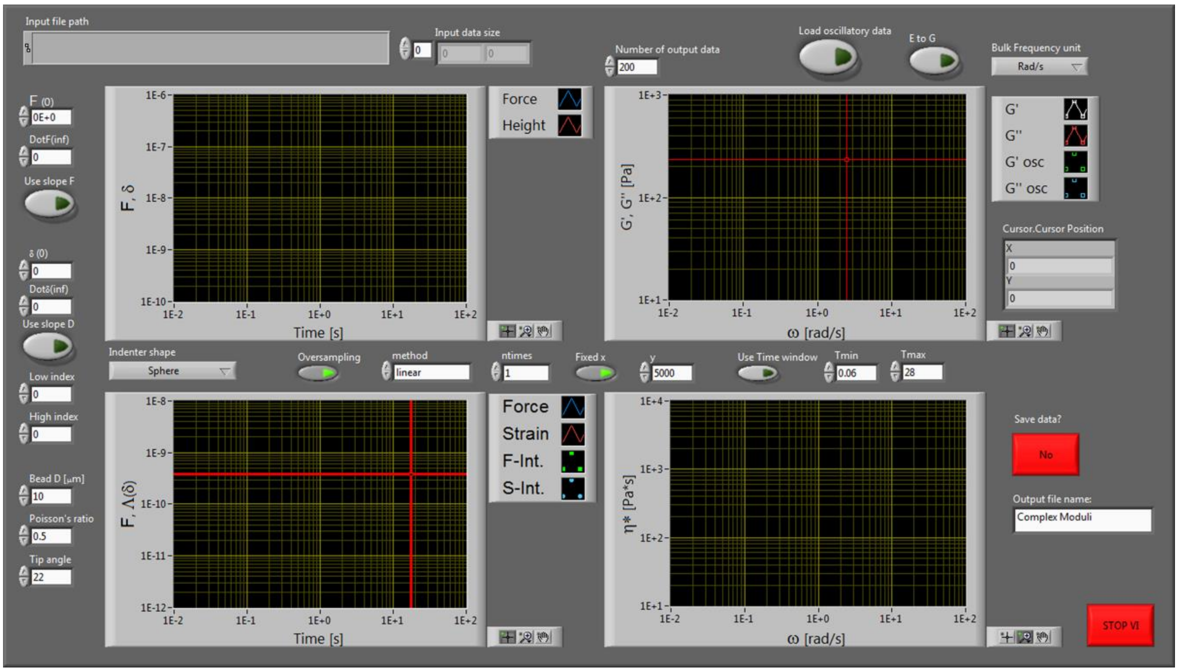

Input file path
Input data size: 0 (0, 0)
Number of output data: 200
Bulk Frequency unit: Rad/s
F (0): 0E+0
DotF(inf): 0
δ (0): 0
Dotδ(inf): 0
Low index: 0
High index: 0
Bead D [μm]: 10
Poisson's ratio: 0.5
Tip angle: 22
Indenter shape: Sphere
method: linear
ntimes: 1
y: 5000
Tmin: 0.06
Tmax: 28
Cursor.Cursor Position: X 0, Y 0
Save data?: No
Output file name: Complex Moduli

**Figure 3.3│Front panel of the Labview (National Instruments) algorithm that implements the analytical method to calculate the Fourier transforms of both measured force and indentation functions in Equation 3.19.**

Recently Tassieri et al. have presented a simple new analytical method for reducing the materials' linear viscoelastic properties, over the widest range of experimentally accessible frequencies, from a simple step-strain measurement, without the need of preconceived models nor the idealisation of real measurements (Tassieri et al., 2016). Although this has been successfully implemented in conventional linear oscillatory measurements, when using the AFM, the analysed data was too noisy at high frequencies to allow reliable conclusions to be drawn (Figure 3.4). This noise may be contributed to by the nonlinear deformation of the material during a fast indentation process, which makes it difficult to separate the non-linear elastic and non-linear viscous responses (Kollmannsberger et al., 2011). Because of this, only stress relaxation data was analysed (i.e. t = 0 is set instead to the point when force (stress) starts to relax; i.e. at the maximum force) (Moreno-Flores et al., 2010; Okajima et al., 2007).

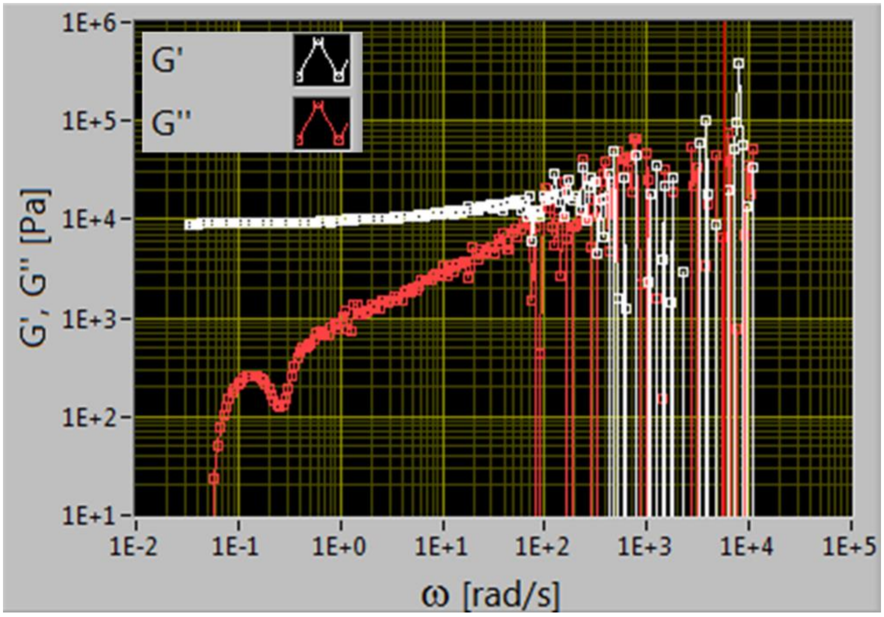

**Figure 3.4│Viscoelastic properties of 30 kPa complex gel analysed with Labview program from initial approach segment.** At the high-end frequencies, a lot of noise present in the data, which made it difficult to establish *G'* (white) and *G"* (red).

The range of accessible frequencies is dictated by the extremes of the experiment time window $[t_{min}, t_{max}]$: i.e. $\omega_{max} = 1/t_{min}$ and $\omega_{min} = 1/t_{max}$ (Tassieri et al., 2016); where $t_{min}$ is the time of the first measured point after t = 0, and $t_{max}$ is equal to the duration of the experiment. Note, although the sampling rate used in the experiment of Figure 3.4 was 11 kHz, a rate of 16 kHz (the upper limit of the NanoWizard II), was used in the rest of the investigations, to maximise the accessible frequency range.

#### *3.6.1.2 The effect of probe dimension*

Physical cues such as probe geometry, loading force and loading rates could affect the measurements of viscoelastic properties of a material (Boccaccio et al., 2015). To understand the relationship between probe diameter and viscoelastic behaviour of a material, we used three spherical probe indenters (4.74 μm, 10 μm and 20 μm) and applied FT-AFM-M procedure to a piece of 20:1 PDMS (6 months old). The piece of 20:1 PDMS had a volume of 14.14 cm$^3$ (radius: 3 cm and height: 0.5 cm) and a contact area of 28.27 cm$^2$. For each indenter, 9 stress relaxation curves were performed and analysed (Figure 3.5).

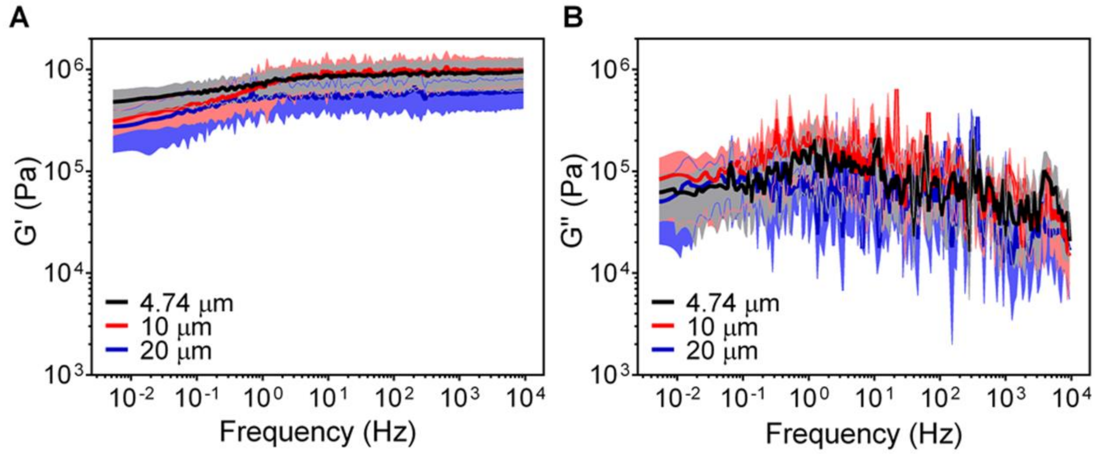

**Figure 3.5│The effect of indenter diameter on the viscoelastic properties of 20:1 PDMS at a loading rate of 3 µm/s (n = 9 measurements), expressed as mean ± SD.** The frequency sweeps below 10 Hz showed that there were differences in *G'* between 4.74 µm/ 10 µm and 20 µm probe geometries ($p < 0.04$), though *G''* did not change.

The calculated viscoelastic properties of PDMS changed with probe dimension. At the higher frequencies ($f > 10$ Hz), the average *G'* was similar for 4.74 µm and 10 µm indenters, while with the 20 µm indenter calculations using the indentation measurements suggested the material was significantly softer ($p < 0.04$). At lower frequencies ($f < 10$ Hz), the average *G'* followed the trend of 4.74 µm > 10 µm > 20 µm. These findings could be associated with local strain on the material; as the probe indenter gets smaller, the tip-surface contact area is reduced (Sokolov, 2007). However, the probe dimension did not show obvious effects on *G"*. This may be partially due to the rounded shape of indenters (Boccaccio et al., 2015), and the PDMS itself being an elastic-like material.

These results clearly showed that different probe indenters could affect the calculated viscoelasticity. Therefore to choose the appropriate probe indenter for an experiment, we have to consider the size of probe in relation to the surface area of the material. The probe would have to be large enough to measure the material globally, but still obey the Hertzian model requirement for tip-surface contact.

### 3.6.1.3 *The effect of loading rate*

To evaluate how loading rates influence measurements of the mechanical property of a material, we applied a range of rates between 3–100 µm/s to 30 kPa and 100 kPa gels. For each loading rate, 4 stress relaxations were performed and analysed, though only one measurement from each rate is shown here (Figure 3.6).

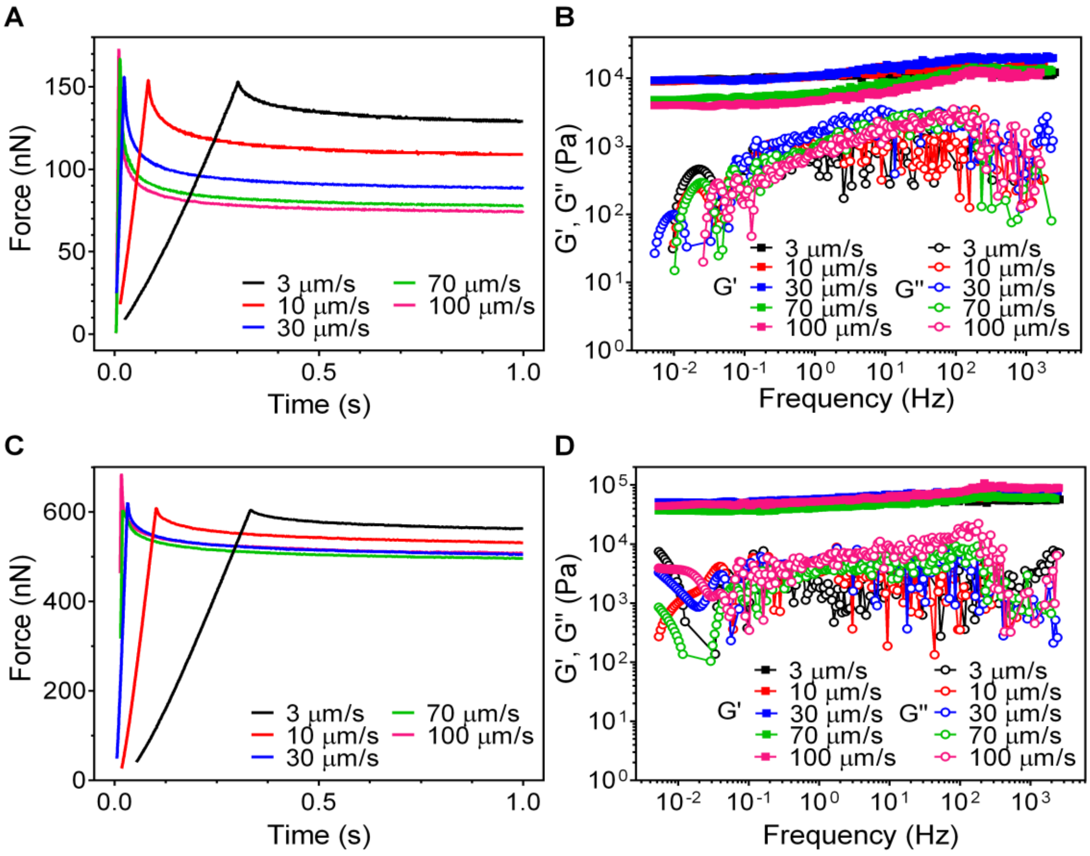

**Figure 3.6│Various approach ramp speeds applied to gels.** The stress relaxation curves for (A) 30 kPa and (C) 100 kPa gels showed that speeds > 70 µm/s the force overshot, otherwise no difference. The frequency sweep for (B) 30 kPa and (D) 100 kPa gels displayed speeds > 70 µm/s, *G'* and *G''* were lower compared to other speeds.

Before looking at any differences in the viscoelastic behaviour of the materials, general features in the stress relaxation curves of Figure 3.6 are discussed: It can be seen that when the loading rates are increased there is a steeper gradient of the measured force with respect to time (Figure 3.6A and C). This is as expected as the indentation depth was kept constant whilst the loading rates increased. The consequence of this is that it would take a shorter time for the cantilever to reach to the set indentation depth. However, it should be pointed out that for 70 µm/s and 100 µm/s rates, the forces reached were different to those at the other loading rates: 3 µm/s, 10 µm/s and 30 µm/s - the z-piezo overshoots at the higher loading rates. This effect leads to an increase in loading force by 9–13% compared to the force reached at the set indentation depth. As a result, the extrapolated viscoelastic properties of the gels changed with increased loading rates (Figure 3.6B and D). With the same gel, lower *G’* values were found at higher loading rates while *G”* remained unchanged, over the entire frequency range ($0.005 < f < 2526$ Hz). The difference in elastic behaviour may be associated with a decrease in contact area as the loading rates were increased (Alao and Yin, 2014).

Each loading rate was applied to the same indentation depth, though it was found that at higher loading rates (i.e. 70 and 100 µm/s), the z-piezo overshot and in turn exceeded the reliable operation range of the instrument. Therefore, as the viscoelastic behaviour for the gels was relatively constant for loading rates between 3–30 µm/s, a loading rate of 10 µm/s was chosen for the rest of the investigations.

#### ***3.6.1.4 Validation of the FT-AFM-M method with complex materials***

Having established the AFM operational parameters that could be used to give reliable measurements, to validate the FT-AFM-M method, a range of complex materials were examined. These materials included commercial gels (30 kPa and 100 kPa), a multi-purpose tac and freshly made 20:1 PDMS. Each material was investigated with both conventional oscillatory measurements using a compact rheometer equipped with parallel plate geometry of 25mm in diameter and the new FT-AFM-M approach. The two studies were compared to see how close the viscoelastic parameters derived from the new technique were to those obtained from conventional measurements. For the commercial gels, these values were also compared to those supplied by the company.

For the 30 kPa gel, it was stated by the supplier that this gel had an average Young’s modulus value of 30 ± 6.67 kPa. Figure 3.7 shows that the elastic properties (*G’*) from FT-AFM-M measurement were in good agreement with the discrete oscillatory rheology data over the frequency range that they share in common (Figure 3.7A). The viscous properties (*G”*) also showed a similar trend, although the absolute values were lower. Over the frequency range of the FT-AFM-M measurement, *G'* values of the material were between 10.01 and 14.79 kPa, while *G"* were between 0.24 and 2.01 kPa, suggesting a dominant elastic nature of the material.

Using the relationship between Young's modulus (*E*) and shear modulus for a linear elastic material; $E = 2(1 + \nu)G'$, (where $\nu$ is 0.5 for the Poisson's ratio of an incompressible material, (Landau et al., 1986)), the Young's moduli calculated from the oscillatory and FT-AFM-M measurements were 30.03 kPa and 33.67 kPa respectively at the lower end of the frequency range studied. This is in excellent agreement with the supplier's value (i.e. 30 ± 6.67 kPa).

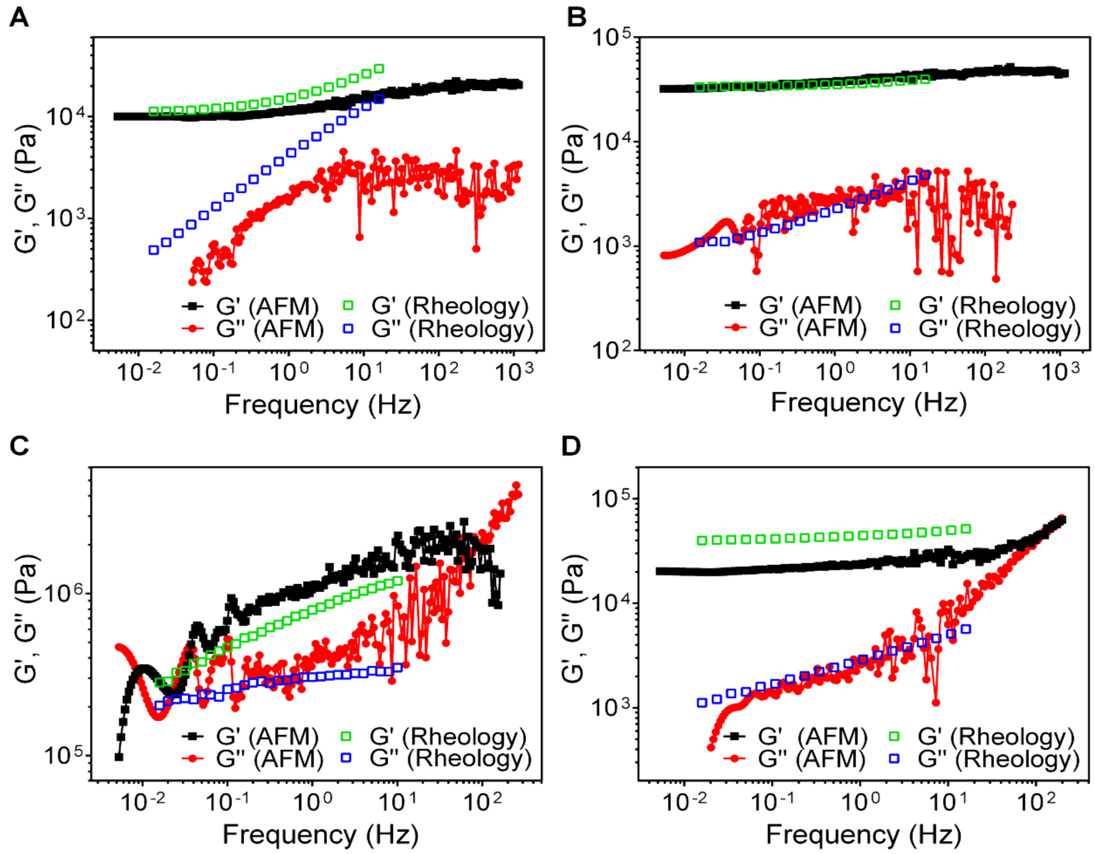

**Figure 3.7│Overlay rheology measurements from compact rheometer against FT-AFM-M for a range of materials; (A) 30 kPa gel, (B) 100 kPa gel, (C) multi-purpose tac and (D) 20:1 PDMS.** The measurements obtained from both techniques were in good agreement with each other, on both *G'* and *G"*.

Similar phenomena were observed for the 100 kPa gel (Young's modulus of 106.67 ± 40 kPa, supplied by the company). The measured G' and G" from both techniques displayed similar trends and absolute values over the frequency range in common (Figure 3.7B). The Young's modulus calculated from FT-AFM-M data gave $96.18 < E < 135.42$ kPa, and $100.55 < E < 119.16$ kPa from the oscillatory data. Again, these values are in good agreement with the supplier's value. These results have shown that the new FT-AFM-M method can provide viscoelastic information that is not only in good agreement with that from conventional techniques, but also over a wider and continuous frequency range.

The multi-purpose tac and freshly 20:1 PDMS were also investigated under the same experimental conditions as the gels. For both materials, the viscoelastic data from the oscillatory and FT-AFM-M measurements were similar over the frequency range in common (Figure 3.7C and D). However, cross-over frequencies were only observed from the FT-AFM-M measurement. Based on this approach, the viscoelastic properties for multi-purpose tac was found to be $0.10 < G' < 1.33$ MPa and $0.47 < G'' < 4.08$ MPa (Figure 3.7C), indicating a typical viscoelastic material. In contrast, the elastic and viscous properties for 20:1 PDMS were found to be $20.26 < G' < 63.06$ kPa and $0.42 < G'' < 65.68$ kPa (Figure 3.7D). It can be noted that the stiffness for this freshly prepared 20:1 PDMS was relatively softer than that of 6 month old 20:1 PDMS (Figure 3.5). The reason for the difference could be related to the aging of PDMS, as the material continued to crosslink even after being thermally-cured (Fuard et al., 2008).

For all complex materials, it was shown that the $G'$ was relatively constant throughout the frequency range, while $G''$ had dips at specific frequencies. Although it cannot be concluded whether these were artefacts from the data analysis or true behaviour of the materials, it would be interesting to measure a larger sample size and a wider range of materials to eliminate any uncertainties within the data.

Within this subsection, I have shown that the FT-AFM-M method can not only be used to calculate viscoelastic properties of a material that are similar to those obtained from traditional techniques, but can also provide added information over a wider frequency range from a single measurement.

### 3.6.1.5 *Viscoelastic properties of cells via the FT-AFM-M method*

Cells can response differently under short or long periods of deformation (Mitrossilis et al., 2010). Short periods (t < 0.1 s) address the instantaneous actomyosin-dependent response caused by the cytoskeletal tension. While at long periods (t >> 0.1 s) the stable response caused by cytoskeletal structure changes within the cell dominates. It would be convenient to investigate both aspect of the cell with one single measurement. However, *a priori*, it is uncertain whether the viscoelastic behaviour from long holding periods would provide the same information as the short holding periods. To address this issue, we collected data for both short-relaxation (t = 1 s) and long-relaxation (t = 30 s) times on PDAC p53 R172H cells (Figure 3.8).

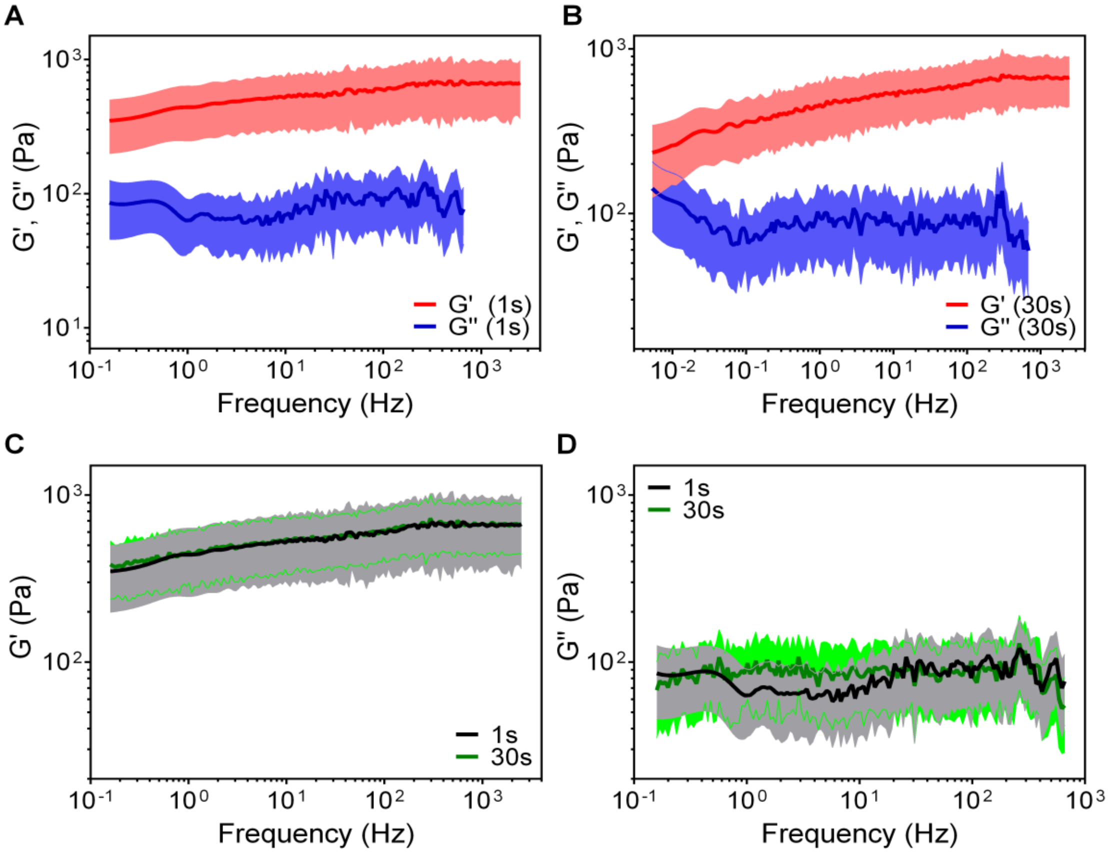

**Figure 3.8│Comparison between the short-relaxation and long-relaxation carried out on PDAC p53 R172H cells (n = 50 cells), expressed as mean ± SD.** The cells' viscoelasticity was measured with (A) t = 1 s and (B) t = 30 s holding times. Both relaxations displayed similar trends in (C) *G'* and (D) *G''* properties.

The accessible frequency range was different for both relaxation times, due to the difference in holding times. For short-relaxation times, it was between 0.16–2400 Hz, while for long-relaxation times, it was between 0.005–2400 Hz (Figure 3.8A and B). Whereas *G'* responses could be calculated over the whole frequency range, *G''* responses were only calculated up to 660 Hz. The reason for the omission of *G''* values at high frequency values from Figure 3.8 was due to knowledge that any induced hydrodynamic drag force on the cantilever only affects *G''* at these higher frequencies (Alcaraz et al., 2003).

Both long- and short-relaxation times exhibited similar viscoelastic behaviour for PDAC mutant p53 cells, over the range $0.16 < f < 2400$ Hz (Figure 3.8C and D). For short-relaxation times, *G'* values were consistently higher than *G''* values. Values for both moduli increased weakly with frequency. Long-relaxation time measurements provided the same findings as those collected over short-relaxation times and added information regarding the cells' mechanical behaviour at frequencies < 0.16 Hz. At $f < 0.16$ Hz, *G''* displayed a greater frequency dependence, which meant that the cells were under transition from one behaviour to another i.e. the cell exhibited the finger print of active dynamics (dissipating energy not just by friction) shown in living systems (Lieleg et al., 2008). The dynamics of cells can be characterised to have the mechanical behaviour of three materials, over several frequency decades; rubbery and glassy material found at low and high frequencies as respectively, and viscoelastic material in the intermediate frequency regime (Vadillo-Rodríguez and Dutcher, 2011). According to the characterisation, the cells under investigation transitioned from the mechanical behaviour of a viscoelastic complex material to a soft glassy material (low end of the regime) with increased frequency.

As general definitions, a viscoelastic material can be described as either a viscoelastic solid or viscoelastic fluid. A viscoelastic solid is when the material can substantially return to its original shape after a large applied load is removed, whereas in a viscoelastic liquid the shape is not regained. This can be illustrated on a frequency sweep graph when *G'* and *G''* crosses over once (viscoelastic solid) or many times (viscoelastic fluid) (Tassieri, 2015). As the frequency sweep for long-relaxation time has displayed one possible cross over (Figure 3.8B), this meant that mutant p53 cells could be described as either a soft glassy material or a viscoelastic solid material.

From the results for both relaxation times, we can safely say that the analysed data from long-relaxation time included data from short-relaxation time and more. As mentioned previously, the widest range of frequencies will give the best overview of the material's structure. Henceforth, we measured each cell using a long-relaxation time protocol, to gain the most information in regards to its mechanical response.

It was noted above that whilst the trends are the same, the absolute values measured with FT-AFM-M may differ slightly from those measured using other procedures. Thus, as a means of cross checking the FT-AFM-M measurements on cells, we calculated the Young's modulus of PDAC mutant p53 cells using both the common AFM indentation method (McPhee et al., 2010) and the FT-AFM-M method, Figure 3.9. When examining the frequency dependence of the viscoelasticity of this cell line (Figure 3.8), it was noted that *G'* values increased with frequency. This means that the Young's modulus calculated at $f$ = 0.005 Hz ($E$ = 0.70 ± 0.33 kPa) is different to that calculated at $f$ = 2400 Hz ($E$ = 2.01 ± 0.67 kPa).

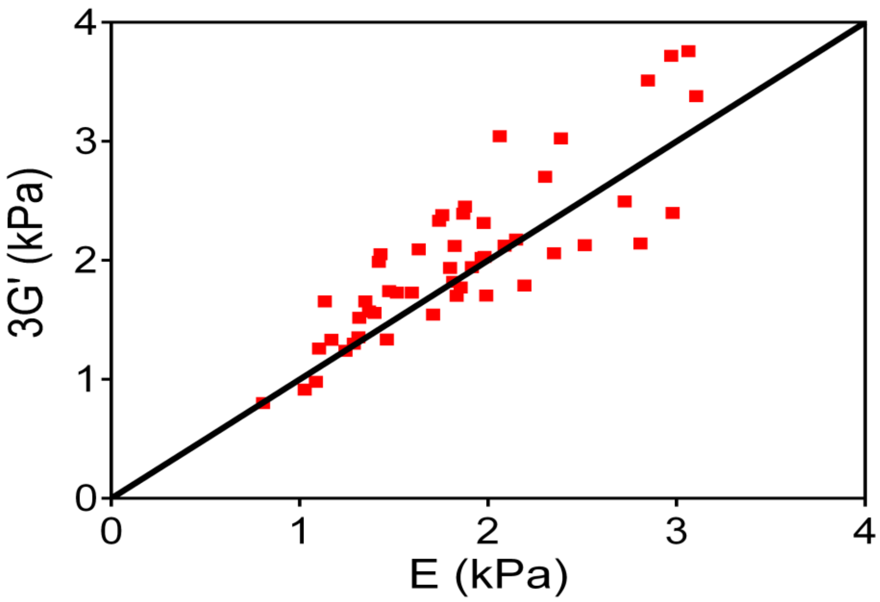

**Figure 3.9│Young's modulus measured using the common AFM indentation method and the new FT-AFM-M method on PDAC p53 R172H at $f$ = 2400 Hz (n = 50 cells).** A good agreement with the two methods; the points lying within y = x line of best fit.

Typically, in AFM indentation measurements the probe indenter being applied to the cell's surface at a set force is then retracted away instantly. Hence these measurements would be comparable to *G'* values at $f$ = 2400 Hz, as this frequency corresponds closest to the time period immediately after the stress relaxation was first recorded. A sample size of 50 cells were measured, compared and presented in Figure 3.9. Each cell was measured with both the conventional procedure and FT-AFM-M measurement. A linear relationship is clearly shown, confirming that the absolute values for the Young's modulus extracted from both methods is essentially the same. This confirmation eliminates the uncertainty of whether the analysed viscoelasticity values are representative of those estimated using different techniques.

### 3.6.2 Effect of cell morphology on viscoelasticity

The viscoelastic properties of cells could be varied by morphology, genetics or overexpression in a signalling pathway. These conditions were investigated and discussed separately to observe any differences in the elastic and viscous properties.

Firstly, we controlled the morphology of PDAC p53 R172H cells by seeding them onto patterned surfaces (Figure 3.10A). These patterned cells were compared against cells on non-pattern surfaces. It can be noted that mutant p53 cells normally stretch and spread out when in culture. Hence, confining cells to a pattern would restrict both their shape and movement, possibly leading to internal stresses. All cells were cultured for 4 hours, prior to FT-AFM-M measurements.

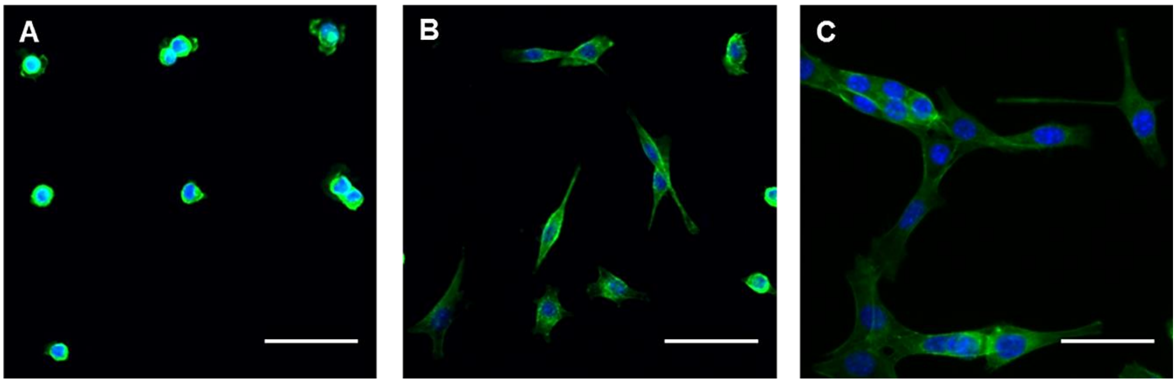

**Figure 3.10│Fluorescent images of PDAC p53 R172H cells cultured on different surfaces, stained for F-actin (green) and DAPI (blue).** The cells were presented in (a) pattern; t = 4 hours, (b) non-pattern; t = 4 hours, and (c) non-pattern; t > 18 hours. All scale bars are 50 μm.

The cells' viscoelastic properties changed with morphology. When $f > 1.9$ Hz, there was a significant difference between the rounded cells on patterned surface and spreading cells on non-patterned surface. There was an increase in *G'* data of between 59–62% and also in *G"* data of about 101%, when comparing spreading and rounded cells ($p < 0.04$; Figure 3.11A and B). This indicates that during this short period of culture, the rounded cells on patterns are stiffer than those that spread on non-patterned surfaces. Although this contradicts other findings which predict that a reduction in the cell shape should lead to a decrease in cell stiffness (Tee et al., 2011), the difference here could be due to either the length of time for which the cells were cultured or the curvature of the rounded pattern cell. Intracellular pressures defined by Laplace equations have shown that edge tension and curvatures can overestimate cellular pressure (stress), which in turn means cell stiffness is higher (Brodland et al., 2014).

When PDAC mutant p53 cells were cultured on non-patterned surface for $t > 18$ hours, the cells exhibited higher elastic and viscous moduli compared to those cultured for 4 hours on non-patterned surface ($p < 0.0001$; Figure 3.11C and D). It was found for non-patterned cells cultured for more than 18 hours exhibited an increase of 44% in *G'* values and 25–68% in *G"* values, when compared to the values for patterned cells that were cultured for 4 hours of culture. Our data agrees with previous finding that the elastic modulus of cells increases with time as it spreads on a surface (Pietuch and Janshoff, 2013). They suggest that a change in cell morphology coupled with change in tension, increases the elastic modulus as the cell spreads (and so broadens the contact area).

In addition, as actin filaments (F-actin) are the major contributor to stiffness for its availability within a cell and its association with cellular contraction, the differences were observed between short- and long-cultured cells. From the fluorescence images (Figure 3.10), F-actin was dispersed evenly across a larger surface area with long-cultured cells, as opposed to being localised in smaller areas as found in short-cultured cells on non-patterned surface. Hence, actin stress fibre formulation due to large cell spreading area and increased contractile tension, increases the overall stiffness during the initial culture period and then stabilises after long periods of culture (Byfield et al., 2009; Tee et al., 2011).

At timescales corresponding to $f < 1.9$ Hz (i.e. if cells are under constant strain for greater than 0.08 s), it has shown that *G'* for both rounded and spreading cells decreases, and shows a weak dependence on the frequency (Figure 3.11A and C). Using the complex modulus (Equation 3.7), we can evaluate the gradients with power-law exponent ($\beta$). The calculated $\beta$ value for rounded cells was 0.10, whilst for spreading cells on non-patterned surface at short- or long-culture it was 0.07. The physical origin of weak power-law values could be related to crosslinking protein (actin filament) dynamics (Hoffman and Crocker, 2009). The weaker power-law value found in the spreading cells on the non-patterned cells therefore indicates more unfolding and cross-linked actin filaments, which was corroborated well with their immunofluorescence images (Figure 3.10).

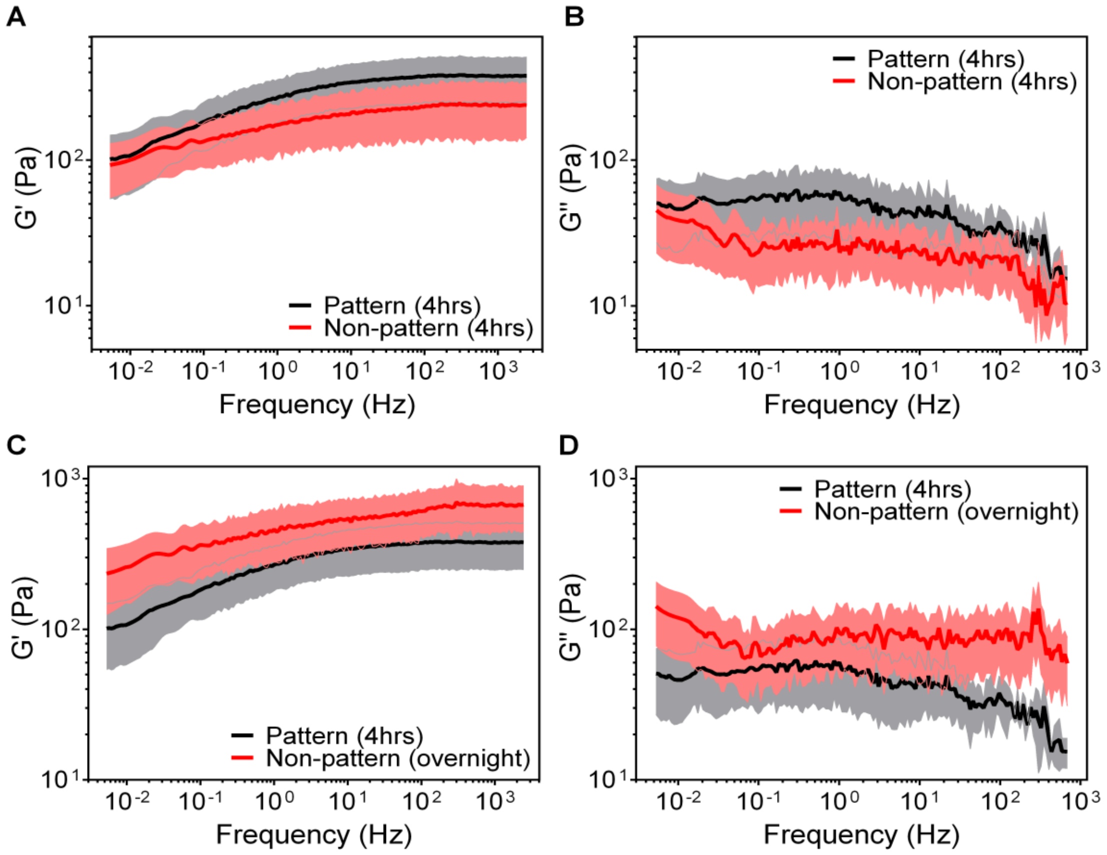

**Figure 3.11│Frequency sweep of the PDAC p53 R172H cells cultured on different surfaces (n = 50 cells), expressed as mean ± SD.** Cells (t = 4 hours) on pattern and non-pattern surfaces were displayed as (A) *G'* and (B) *G''*. At high-end frequencies, the non-patterned cells were softer and fluid-like compared to patterned cells ($p < 0.04$), whilst at low frequencies, both cells exhibit similar properties. Cells on pattern (t = 4 hours) and non-pattern (t > 18 hours) surfaces were displayed as (C) *G'* and (D) *G''*. For t > 18 hours, the non-patterned cells were stiffer and more liquid-like than patterned cells ($p < 0.0001$).

Interestingly, when $f$ < 0.2 Hz, $G''$ for the spreading cells on non-patterned surfaces starts to increase with decreasing frequency, although $G''$ for the rounded cells on patterns remains the same (Figure 3.11C and D). Since the variations of viscosity are related to fluid movement within cytoskeleton network/ organelles and the shape change (Bhat et al., 2012) and/or active dynamics, this observation suggests that the spreading cells might have started to change shape (or migrate) in response to the imposed stress at this time scale (t < 0.76 s). Furthermore, it appears that constraining the cell shape provides an effective means to control cells viscous properties.

The PDAC p53 R172H cells have been shown to be invasive and metastatic (Timpson et al., 2011b). Again, by restricting the cell shape of these cells, we may be able to understand the effect of mechanical behaviour change and its contribution towards cell remodelling and motility. In 2-dimensional culture, cells were stretched out, whereas in 3-dimensional culture, cells were rounder due to restrictions within a matrix (Morton et al., 2010; Timpson et al., 2011b). This change in morphology can modify the mechanical response, as previously discussed. With the change in properties, this in turn could assist cells to move through tissue easily.

### 3.6.3 Effect of deleted p53 gene on viscoelasticity

To address how genetics can affect the viscoelastic behaviour of cells, we investigate the mechanical properties of PDAC mutant p53 (PDAC p53 R172H) and deleted p53 (PDAC p53 fl) using FT-AFM-M. TP53 is a tumour suppressor gene and is also often mutated in human pancreatic cancer through missense mutations (changes by switching one amino acid in the chain for another) (Scarpa et al., 1993). With an increase amount of mutant p53 protein, this could potentially lead to gain-of-function or dominant-negative behaviour within a cell. The PDAC mutant p53 cells were retrieved from genetically engineered mice model for the study of gain-of-function activity.

The aforementioned mutant p53 cells have been shown to exhibit invasive activity in an *in-vitro* assay and demonstrate a prometastatic function, meanwhile deleted p53 does not (Morton et al., 2010). In culture, mutant p53 and deleted p53 cells exhibit stretched and rounded morphologies, as respectively (Figure 3.12). In addition, it was shown that although the F-actin distributions for both cells were similar, the mutant p53 cells dominated a larger surface area. Both morphology and metastatic potential difference could contribute to the overall mechanical behaviour (Pietuch and Janshoff, 2013; Rother et al., 2014).

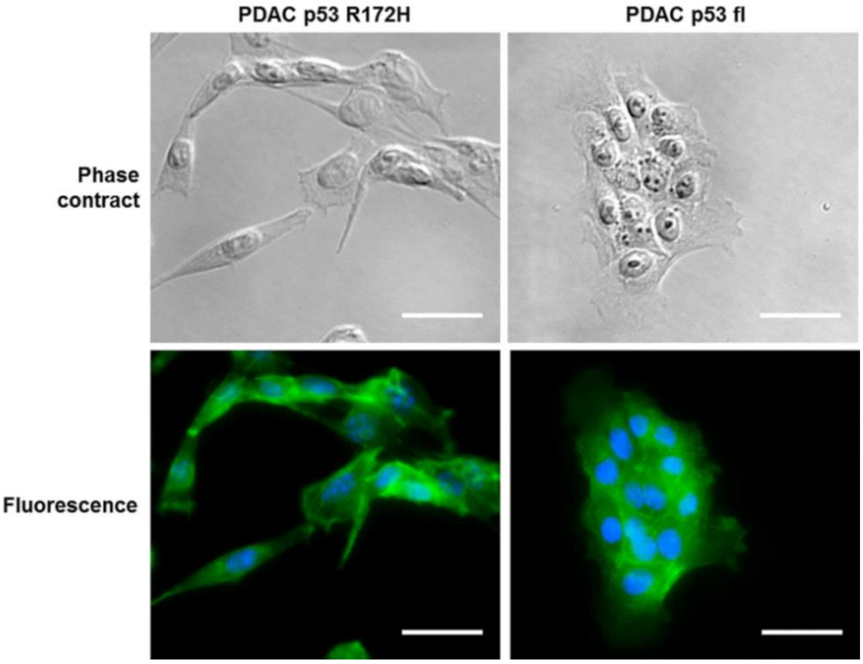

**Figure 3.12│Comparison between the cell morphology of PDAC p53 R172H and PDAC p53 fl cells.** The cells were stained with DAPI to show nucleus (blue) and phalloidin to show F-actin (green). All scale bars are 30 µm.

Over more than five decades of frequency (0.005–2400 Hz), there were significant differences between the elastic properties of mutant p53 and deleted p53 cells ($p < 0.01$; Figure 3.13A). For mutant p53 cells, *G'* data at 0.005 Hz was 234 ± 109 Pa and increased steadily with frequency following a power-law with exponent $\beta = 0.07$. For deleted p53 cells, *G'* data at 0.005 Hz was 117 ± 55 Pa and increased at the same rate with frequency, hence the power-law with exponent were similar, $\beta = 0.08$. Over the five decades of frequency, the mutant p53 cells were 45–50% higher in *G'* compared to deleted p53 cells. The difference in elastic behaviour could be due to a larger spreading area of mutant p53 cells and an increased amount of actin stress fibres (Figure 3.12), which increased contractile tension. As a consequence, the overall properties would be stiffer (Tee et al., 2011).

The data of Figure 3.13B show that there were no obvious differences between the viscous properties of both cell types at high frequencies, though differences shown at low frequencies ($f$ < 0.05 Hz). For both cell lines, *G''* data plateaued at around 70–80 Pa at the high-end frequency, but interestingly, started to increase with decreasing frequency when $f$ < 0.05 Hz - the same phenomenon as observed in Figure 3.11. This indicates cells could experience change in mechanical behaviour from a soft glassy state to a transition viscoelastic state (Kollmannsberger and Fabry, 2009). During long deformation period, the mutant p53 cells have been shown to dissipate more energy within the cell compare to deleted p53 cells. This lost energy could be related to the internal friction induced by cytosol movement between macromolecules.

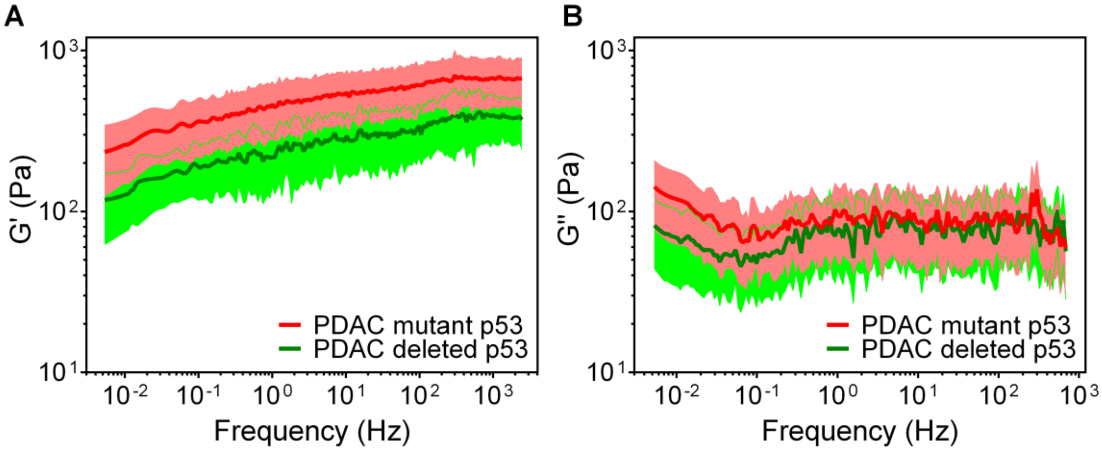

**Figure 3.13│Stress relaxation carried out on PDAC mutant p53 and deleted p53 cells (n = 50 cells), expressed as mean ± SD.** Frequency sweeps of (A) *G'* and (B) *G''*. Over the frequency range, mutant p53 cells displayed stiffer properties compared to deleted p53 cells ($p < 0.01$), while their fluid-like properties remained the same.

The PDAC mutant p53 cells have been known to be invasive and malignant, while deleted p53 cells were non-invasive and benign (Morton et al., 2010). Due to p53 protein deletion, the cell morphology changed; mutant p53 cells were stretched and deleted p53 cells were rounded. The viscoelastic response observed for these cells contradicts other studies regarding invasive and metastatic cells (Rother et al., 2014; Shi and Zhao, 2004). However, the cells within those studies had the same morphologies as each other. Hence, the reason for mutant p53 (stretched) and deleted p53 (semi-rounded) cells to exhibit similar properties when patterned and non-patterned.

The overview of this investigation suggests that for cells that have undergone genetic modification, the overall elastic properties were dominated by morphology changes, whereas the viscous properties were unaffected. With this information in mind, we proceeded to study how overexpression of ROCK activity could affect a cell's mechanical response, when the cell morphologies were kept constant.

### 3.6.4 Effect of ROCK activation on viscoelasticity

Overexpression of Rho kinase in cells was investigated to understand the downstream effect on their viscoelastic behaviour. The PDAC p53 fl cells were tagged with EGFP:ER (control) and two ROCK isoforms; ROCK1:ER and ROCK2:ER. Each cell line was measured with and without 4HT treatment on separate days. These cells have been shown to exhibit invasive activity with ROCK activation, while their cell morphologies were unchanged (Figure 3.14).

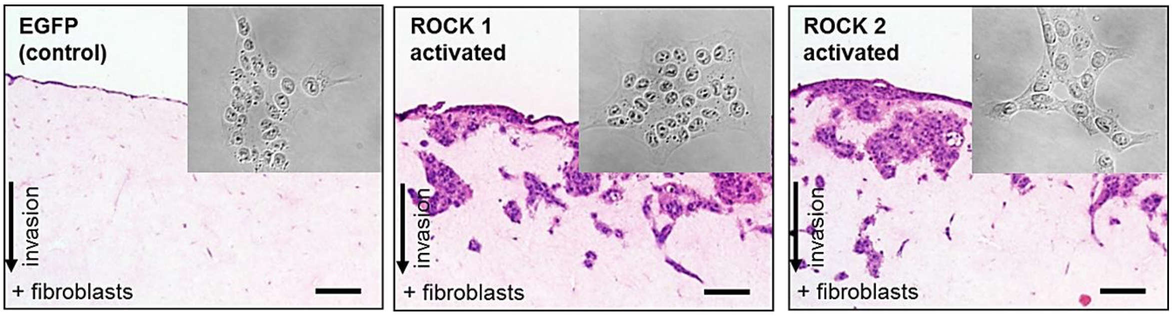

**Figure 3.14│H&E-stained sections of modified PDAC cells with 4HT treatment cultured on organotypic matrix (8 days) and their cell morphologies.** Activated ROCK cells displayed its invasiveness through the matrix whilst the control cells remain on the surface. All scale bars are 100 μm. (Data obtained from Dr. Nicola Rath)

The acquired viscoelastic data for each modified PDAC p53 fl cells were compared against EGFP:ER cells (control), which were measured on the same day. The reason for interpreting the data in this way was so that the experimental errors due to environmental condition could be eliminated (Lanza et al., 2010). Over the frequency range (0.005–2400 Hz), there were significant differences between the elastic property of ROCK1:ER and ROCK2:ER cells against the control, for both treated and untreated conditions ($p < 0.0001$; Figure 3.15A and C). In addition, for the two ROCK isoform cells, no differences in *G'* was observed when they were overexpressed, though the cells were dissimilar when treatment was not applied ($p < 0.04$). Meanwhile the viscous behaviour was consistent for all cells treated or untreated except for EGFP:ER -4HT, over the entire frequency range ($p < 0.04$; Figure 3.15B).

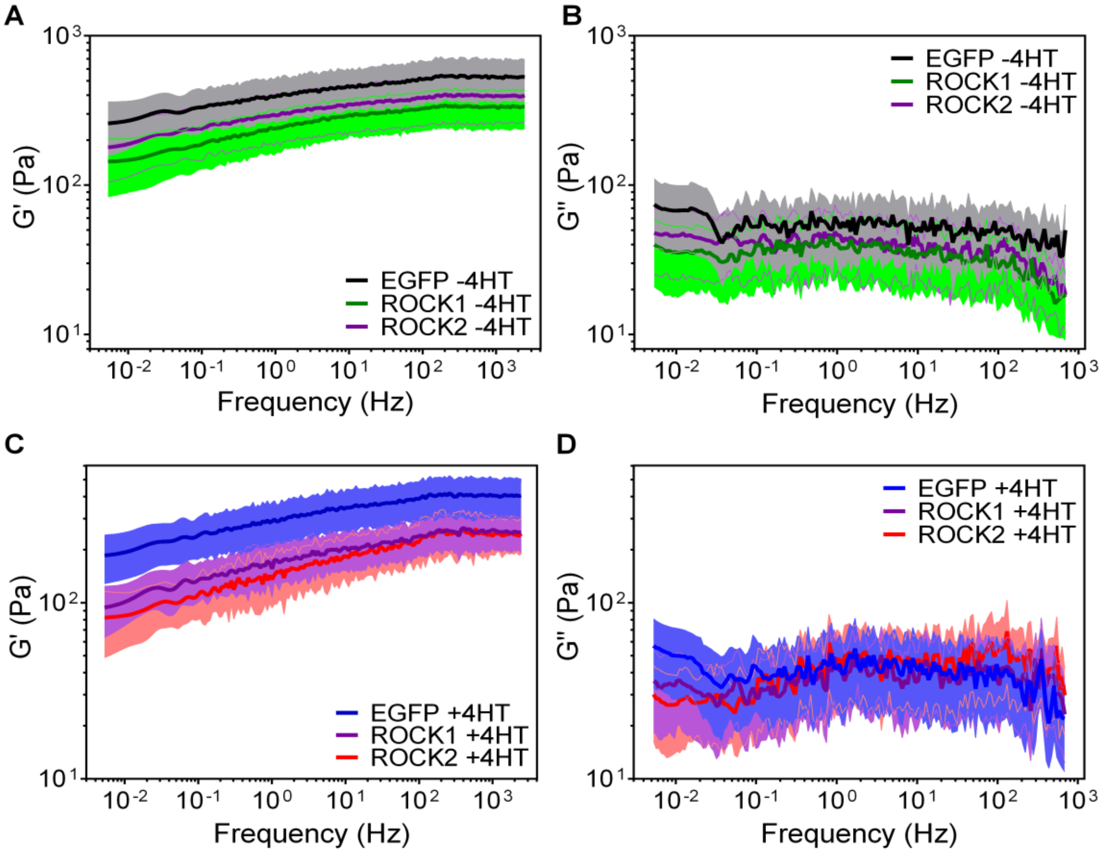

**Figure 3.15│Frequency sweep of the modified PDAC cells following +/- 4HT treatment (n = 50 cells), expressed as mean ± SD.** Over the frequency range, treated ROCK1:ER and ROCK2:ER cells were more compliant relative to EGFP:ER cells ($p < 0.0001$), while their viscous properties were unchanged.

Focusing on untreated cells, *G'* data at 0.005 Hz was 259 ± 101 Pa for EGFP:ER, 143 ± 60 Pa for ROCK1:ER and 179 ± 74 Pa ROCK2:ER cells. Within these cells, *G'* data increased steadily with frequency following a power-law exponent $\beta = 0.06$. *G"* values were lower than *G'* values throughout the frequency spectrum. Given that cells were not treated with 4HT, there should not be a difference between the cells' mechanical response. However, not only was there a difference among the cell lines, these cells exhibited stiffer properties compared to their parental cell line (PDAC p53 fl). The difference in *G'* was most noticeable in EGFP:ER cells, where cells doubled in stiffness. The change in elastic response may be associated with the tagged fluorescent protein, due possibly to an increase in lateral interaction from molecules among phospholipid chains and so increases stiffness (Lulevich et al., 2009).

For treated cells, *G’* data at 0.005 Hz was 185 ± 57 Pa for EGFP:ER, 94 ± 30 Pa for ROCK1:ER and 82 ± 33 Pa ROCK2:ER cells. A power-law exponent was obtained from viscoelastic curves, giving EGFP:ER, ROCK1:ER and ROCK2:ER values of 0.07, 0.08 and 0.09, as respectively. These power-law values were stronger compared to untreated cells, which indicate that these cells display a more fluid-like behaviour. The viscoelastic behaviour of the treated cells followed a similar trend to the untreated cells. This meant that it was difficult to assess whether there was any real reduction in *G’* for overexpressed Rho kinase. Therefore to distinguish between the actual reductions in stiffness, we drew up the table below outlining the percentage of reduction between ROCK1:ER and ROCK2:ER against EGFP:ER cells (with and without treatment), at low-end, mid-range and high-end frequencies (Table 3.2). These frequencies were chosen as this would provide us with exact reduction in elasticity at the initial, during and t = 30 s of stress relaxation.

**Table 3.2│A table to display *G’* values of ROCK activated and inactivated cells at low, mid-range and high frequencies and their differences relative to the control (%).** The values in the brackets display the percentage of reduction relative to the control and inactivated cells.

| | **Frequency (Hz)** | | | | | |
|---|---|---|---|---|---|---|
| **Cell Type** | ***0.005*** | | ***27.24*** | | ***2400*** | |
| *EGFP:ER -4HT* | 259.09 | | 472.06 | | 529.62 | |
| *ROCK1:ER – 4HT* | 143.74 | - 45% | 304.34 | - 36% | 334.49 | - 37% |
| *ROCK2:ER -4HT* | 179.17 | - 31% | 364.66 | - 23% | 397.39 | - 25% |
| *EGFP:ER +4HT* | 185.48 | | 359.25 | | 404.47 | |
| *ROCK1:ER +4HT* | 93.87 | - 49%<br>(**- 4%**) | 212.36 | - 41%<br>(**- 5%**) | 250.61 | - 38%<br>(**- 1%**) |
| *ROCK2:ER +4HT* | 82.32 | - 56%<br>(**- 25%**) | 192.18 | - 47%<br>(**- 24%**) | 246.85 | - 39%<br>(**- 14%**) |

According to the table, the actual reduction in elastic behaviour for overexpressed ROCK1 was between 1–5%, while overexpressed ROCK2 was between 14–25%. Although these findings agree with our previous outcomes, the degree of reduction was different.

The modified PDAC ROCK cells were shown to exhibit invasive properties, when cells were overexpressed with Rho kinase. As the difference in cell morphology was not a contributing factor, it was interesting to observe the change in viscoelastic behaviour between the cells. Although the mechanical behaviour for ROCK1:ER and ROCK2:ER changed relative to EGFP:ER, either with or without treatment, overall the cells were softer with overexpression of Rho kinase. Meanwhile the viscous portion of the cell remains constant. This may be related to the modification of gene expression. As aforementioned in the previous chapter, while ROCK activation promotes stable actomyosin contractile force generation, it was observed that there was a decrease in number of actin bundles when Rho kinase was overexpressed. Therefore even if the force contraction was generated by the filaments present, it would be insufficient compared to the inactivated ROCK cells. The FT-AFM-M findings regarding the viscoelastic properties of cells with differing invasiveness were in agreement with other researchers, and so in turn could provide a possible diagnostic tool in identifying such cells (Rother et al., 2014).

## 3.7 Conclusions

We have developed a novel procedure that only requires a single measurement to obtain the viscoelastic properties of a cell over a wide continuous frequency spectrum ($0.005 < f < 2400$ Hz). By achieving over five frequency decades, we can better understand the mechanical changes occurring with time and in turn details regarding a material's overall structure. Biologically, we have uncovered that predominately pancreatic cancer cells can be described as being in a soft glassy state even when confinement conditions were altered. In addition, we have shown that cell morphology changes both elastic and viscous behaviour within cancer cells, though modification of gene expression only affects the elastic portion. This means that cell morphology is one major factor that contributes towards the mechanical properties. In reality, the mechanical response of cancer cells in its physiological conditions is very complex. Hence, further investigation to understand the influence of conditions such as longer indentation stressing periods (e.g. $t > 1$ minute), different substrate stiffnesses and co-culture between cancer and normal cells, on the cell's viscoelasticity.

# Chapter 4 Cancer Cell Migration

## 4.1 Abstract

Cancer cell migration involves the ability of cells to migrate through 3-dimensional (3D) extracellular matrix tissue and to overcome any steric hindrance imposed upon them. These hindrances may include small spaces that are smaller than the cell itself. In the past decades, there has been usage of microfluidic devices to mimic the physiological environment to study these cell migrations. However, it is still unclear how cell mechanics and cell migration are related to each other, especially when the cells are physically confined or constrained. Here, we developed a high-throughput microfluidic device capable to study single cell migration under physical and chemical stimuli. The device was composed of two chambers separated by an array of microchannels of 3, 4 and 5 μm wide with either abrupt or tapered openings, and together at heights of 5, 8 and 15 μm. Various pancreatic ductal adenocarcinoma (PDAC) cells with different mechanical properties modulated by the deletion of p53 gene or by overexpression of ROCK1 activity were examined using both the microfluidic devices and transwell plates, on their migratory behaviour. For both invasive mutant and non-invasive deleted p53 cells it was found that the ability of them to pass through and their cell length changed with the width of the channels, but remained unchanged with the channel openings. Furthermore, there was no difference between migration speeds and cell lengths within the channel of mutant p53 and deleted p53 cells, which is suggestive that their cellular behaviour was similar under confinement. Overexpression of the ROCK1 activity was also investigated and showed an average reduction of 6–20% in cell length and 45–50% in migration velocity, when cells were under confinement.

## 4.2 Introduction

Cell migration is an important feature for both tissue homeostasis and pathological processes, particularly in wound healing, inflammation and cancer (McGregor et al., 2016). By changing the cell shape and mechanical behaviour to interact with the surrounding tissue structures, cells can migrate. Conventionally, it is thought that cancer cells invade or metastase by individual cells detaching off the primary tumour site, enter the lymphatic vessels or blood stream before developing a seconding tumour site elsewhere (Friedl and Wolf, 2003)(Friedl and Wolf, 2003). However, cells can detach and migrate from primary tumour site either as individual cells or as collectives of cells (Friedl and Wolf, 2003). For single cell migration, there are two types of cells known as mesenchymal and amoeboid, which follow different cancer cell invasion (Lange and Fabry, 2013).

Mesenchymal migration is characterised by an elongated cell morphology, longer protrusions and strong polarity (Huang et al., 2011). The migration process that occurs here involves cells becoming polarised, forming actin-rich protrusions at the front of the cell that then focally attach to the substrate, cell contraction, and then the generation of actomyosin contraction that detaches the rear of the cell (Paňková et al., 2010). This procedure has been stated to be highly associated with the Rac pathway, which is known to regulate actin polymerisation and membrane protrusions (Raftopoulou and Hall, 2004; Sahai and Marshall, 2003).

Amoeboid migration is characterised by cells having a rounded structure, being highly deformable, having low adhesiveness to substrates, and short thin protrusions (Clark and Vignjevic, 2015). Many cancer cells follow this mode of migration. This process consists of cycles of expansion and retraction of the cell body facilitated by contraction of the cortical actin through association with the ROCK pathway (Paňková et al., 2010; Sahai and Marshall, 2003).

A third mode of migration that can be detached from the primary tumour site is known as collective migration. This involves a group of cells that migrate as a sheet/ cluster with constant cell-cell contact (Huang et al., 2011). Individual cells within the group would behave as mesenchymal migration, and so as a collection they would be highly polarised with movements in the direction of high stress.

The mechanical properties of cells and substrate play an important role during migration (Lange and Fabry, 2013). Cells migrate due to the imbalance between transmitted contractile forces generated by the cell and adhesiveness between cell and substrate, which would lead to a net traction force (DiMilla et al., 1991). The contractile forces would increase cytoskeletal pre-stress (pre-existing tension even without external load), and in turn increase cell stiffness (Wang et al., 2002). When cells have high stiffness, this would suggest more spreading and stronger contractions occurs which, overall, along with strong adhesion forces with the matrix would lead to slow migration.

During mesenchymal migration in 3D, cells pull themselves through the matrix and push interfering fibres away by proteolysis (break down of proteins/ peptides into amino acids) (Parri and Chiarugi, 2010). This migration is known to be “path generating”, whereby traction forces, cell polarisation and orientation have to be connected for strong migration (Lange and Fabry, 2013). Meanwhile for amoeboid migration, cells contain low mechanical properties and weak focal adhesions so they can move in between the matrix (Wolf et al., 2003). This is known as “path finding” as these cells squeeze through confined spaces rather than degrading it. Finally collective migration, this is when cell-cell interactions are strong that in turn would lead to weaker cell-matrix adhesions (Al-Kilani et al., 2011). This mode of migration is achieved by the imbalance forces between the cells rather than the forces difference between cell and matrix.

Regulation of Rho GTPases has been shown to be associated with cell migration (Raftopoulou and Hall, 2004). Three members of the family include Rho, Rac and Cdc42, which in turn play a specific role in cell migration. During migration, Rho (ROCK) regulates the actomyosin contraction, Rac regulates the actin polymerisation to form the peripheral lamellipodia, and Cdc42 controls both the actin polymerisation to form filopodial protrusions and establish cell polarity (Morgan-Fisher et al., 2013).

Our study focuses on ROCK activity, which is involved in the assembly of focal adhesions, the regulation of contraction forces in the cell body and retraction forces at the rear of the cell (Raftopoulou and Hall, 2004). Aforementioned, when ROCK is activated, it phosphorylates LIM kinases and in turn inactivates cofilin that leads to actin stabilisation. In parallel, ROCK activation phosphorylates myosin and inactivates myosin phosphatase (hence again activation of phosphorylates myosin), together an increased level of myosin activity that would then combine with actin filaments, to generate actomyosin contractions. This activated pathway is applied to the rear of the cell to promote cell movement via traction forces and detachment at the rear of the cell via retraction forces (Mitchison and Cramer, 1996). Due to its inability to create membrane protrusions, ROCK is ineffective at the front of the cell and could pose issues, thus a counter activity to inhibit ROCK would occur during cell migration (Parri and Chiarugi, 2010).

Within this chapter, I evaluated the effect of cell invasiveness and overexpressed ROCK1 activity on single cell migratory behaviour, and how this is associated with their mechanical properties. This was carried out using a conventional transwell assay and a high-throughput microfluidic device that contained an array of microchannels with different degrees of narrowness. Together, these studies facilitate the understanding of the correlations between cell mechanics and cell migration.

## 4.3 Materials and Methods

### 4.3.1 Cells

The cells under investigation included PDAC mutant p53 (PDAC p53 R172H), deleted p53 (PDAC p53 fl) cells and modified PDAC p53 fl cells tagged with enhanced green fluorescent-estrogen receptor protein (EGFP:ER), and conditionally active ROCK1-estrogen receptor fusion proteins (ROCK1:ER). To overexpress ROCK activity, 1 µM of 4-hyroxytamoxifen (4HT) was added to the culture medium, as shown in Section 2.3.2.2.

### 4.3.2 Transwell assay

Cell migration was assessed using 3 µm, 5 µm and 8 µm transwell plates (Corning Incorporated Transwell® 24 well with polycarbonate membrane inserts. The plates including inserts were rehydrated by adding 50 µl and 200 µl of warm serum-free media to each insert and bottom chamber, respectively. The transwell plate was then incubated at 37°C for 1 hour. After rehydration, all the media was removed from inserts and bottom chambers. For each well, 200 µl of 25000 cells/ ml in serum-free media was added to the transwell inserts, whereas 650 µl of serum media (contains 10% fetal bovine serum) was added to the bottom chambers. In parallel with the transwell plates, 200 µl of cell densities with 5000, 10000, 15000, 20000, and 25000 cells/ ml were seeded into separate wells on a 24 well plate. All plates were cultured at 37°C with 5% $CO_2$ in a humidified incubator for 16 hours. Once incubated for 16 hours, all media were removed from all plates. The migrated cells at the bottom of the inserts and cells from the separate 24 well plate were washed briefly with PBS and fixed with 3.8% formaldehyde, PBS in 2% sucrose for 10 minutes at room temperature. The migrated cells were stained with 0.1% crystal violet for 20 minutes, to stain the cell membrane by detecting the peptidoglycans present. To quantify the stained transmigrated cells, these were dissolved in 10% acetic acid for 20 minutes. A plate reader (BioTek, Synergy HT) was used to measure the absorption (600 nm) of both the migrated cells from the transwell plate and the cells from the separate plate. A plate with known cell densities was used as a standard to convert the absorption values to a cell number.

### 4.3.3 Microfluidics design and fabrication

The microfluidic device was an adaptation of that described by Rao *et al.*, whereby mechanical stresses are imposed on cells when they were chemotactically driven into confined channels (Rao et al., 2014). The device consists of two open chambers with a dimension of 14 mm in length and 10mm in width, one of which holds cells in 200 µl of serum-free media and the other contains 200 µl of serum media alone (Figure 4.1).

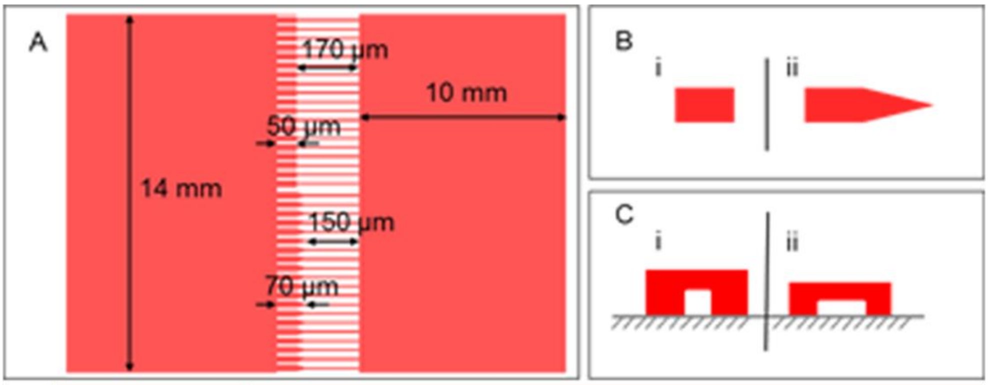

**D**

| | Channel height | | |
|---|---|---|---|
| **Channel width** | 5 µm | 8 µm | 15 µm |
| **3 µm** | 15 $\mu m^2$ | 24 $\mu m^2$ | 45 $\mu m^2$ |
| **4 µm** | 20 $\mu m^2$ | 32 $\mu m^2$ | 60 $\mu m^2$ |
| **5 µm** | 25 $\mu m^2$ | 40 $\mu m^2$ | 75 $\mu m^2$ |
| **15 µm (opening)** | 75 $\mu m^2$ | 120 $\mu m^2$ | 225 $\mu m^2$ |

**Figure 4.1│Schematic drawing of (A) the microfluidic device, (B) plane view of tapered and abrupt channel openings, and (C) the side profiles of the symmetric and asymmetric narrow channels. (D) A table outlined to show the dimensions of the confined channels and including the total area in which cell migrate through.**

The difference in serum composition or concentration will chemotactically drive the cells between the two chambers. These two chambers were connected by 600 microchannels of 3 μm, 4 μm and 5 μm widths with tapered and abrupt channel openings. The heights of the channels were also varied between 5–15 μm. The spacing between the adjacent channels was 15 μm in width, due to the typical cell size used within our studies was 10–15 μm.

The stated design was drawn up in L-Edit program, and printed onto a chrome photomask for photolithography. Contact photolithography was used to generate a patterned SU-8 (MicroChem Corp) layer of 5 μm, 8μm or 15 μm thickness on a silicon (Si) wafer, corresponding to the desired height of the microchannels (Table 4.1). The Si wafer was washed with acetone, methanol and isopropyl alcohol (IPA), each for 5 minutes in an ultrasonic bath; to remove any dust particles that could prevent resist from adhering or to cause any imperfections on the surface once coated with resist of functional chemical species. In between each wash the wafer was fully dried using a nitrogen gun. The SU-8 3000 series negative photoresist was spin-coated onto the Si wafer, and soft-baked at 95°C. The substrate was then placed in the MA6 mask aligner (detailed conditions in Section 3.5.3) along with the photomask, to expose the resist with the desired pattern. Post exposure, the wafer was heated again at 95°C, to accelerate the SU-8 polymerisation and crosslinking process. For development, microposit EC solvent was used, followed by rinsing with IPA. The developed surface was fully dried using nitrogen gun before checked under an optical microscope. To further crosslink the remaining resist and so minimise the risk of damage when used as a PDMS soft lithography mold, the developed pattern wafer was hard-baked at 120°C for 2 hours.

**Table 4.1│A table outlining the pre-bake, exposure, and post-bake parameters used to achieve optimal thickness.**

| Thickness (μm) | SU8 coating | Spin speed (rpm) | Pre-bake | Exposure time (s) | Post-bake |
|---|---|---|---|---|---|
| 5 | 3005 | 4000 | 2 min | 20 | 3 min |
| 7 | 3005 | 2000 | 3 min | 50 | 3 min |
| 8 | 3010 | 4000 | 8 min | 30 | 3 min |
| 15 | 3010 | 1000 | 15 min | 40 | 3 min |

Once the microchannels were created, the remainder of the device was made to be 15 μm in height. This meant that to achieve the final structure, the 5 μm and 8 μm patterned features had to be accurately aligned in several, successive, photolithographic processing steps. For each patterned layer, the surface was observed using profilometer (Dektak), to measure whether the desired thickness had been achieved. The developed silicon wafers were hard baked between processes, and finally baked to be used in soft lithography.

The patterned silicon wafers were silanized by immersion in 1% trichloro(1H,1H,2H,2H-perfluorooctyl)silane in heptane for 10 minutes at room temperature (covered). This procedure was to help with removal of the PDMS off the silicon mold, by creating a hydrophobic surface. The PDMS devices were made using a ratio of 10:1 PDMS oligomer to curing agent (Sylgard 184; Dow Corning). The oligomer and curing agent was evenly mixed, and poured onto the silanized silicon mold. The mixture was degassed under a vacuum and baked for 2 hours at 70°C.

The cured devices were peeled from the silicon mold, and along with glass coverslip slides (Thermo Scientific) were washed with acetone, methanol and IPA, each for 5 minutes in an ultrasonic bath. To complete the microfluidic devices, the two cleaned surfaces were permanently bonded using oxygen plasma treatment for 40 seconds with 80 W RF power (Gala Instruments Plasma Prep 5). The treated surfaces were pressed together and baked for 5 minutes at 70°C, to complete the seal.

### 4.3.4 Cell loading and imaging in microfluidic device

The fabricated devices were oxygen plasma treated (Diener electronic Zepto) for 60 seconds with 80 W, prior to cell seeding. This was done so that the surfaces were hydrophilic enough for capillary action (ability for liquids to flow through narrow spaces without the assistance from any external forces) to take place, when cells were seeded into the devices. A cell density of 200000 cells/ml was made in serum-free media and 50 μl of this suspension was added straight into the plasma treated device. Using an optical microscope, it was possible to observe the cells being positioned at the openings of the channel tapers. Once most of the channels were filled with a single cell, we add 50 μl of 10% serum media to the other chamber; to aid migration. This set-up was cultured at 37°C with 5% $CO_2$ in a humidified incubator for 2 hours for cells to settle and attach.

An additional 150 µl of serum-free and serum media was added to the chamber with cells and the one without respectively. Cell migration in the devices was observed under Zeiss AxioObserver microscope coupled with a DU885 iXon CCD digital camera (Andor Technology). Using AxioVision software (Zeiss), we took images vertically along the device capturing every channel, with 20x, 0.5 NA objective lens. The cells were kept under culturing conditions, whilst time-lapse images were taken every 5 minutes for 10 hours, to observe cell migration.

The captured images were processed using ImageJ software (open source), to analyse the number of cell migrated in to the channels, cell lengths within confined channels at 2, 6 and 10 hour period. In addition the migration velocities were also obtained of cells migrating over the 10 hours.

## 4.4 Results and Discussion

### 4.4.1 Invasiveness versus cell migration ability

A transwell assay is one of the most commonly used methods to study cell migration according to their chemotactic behaviour (Decaestecker et al., 2007). Here, we have used this simple migration technique to evaluate the potential of PDAC cells to migrate through constrained spaces. These results were later compared against the data obtained in the microfluidic devices.

By using PDAC mutant 53 and deleted p53 cells, we measured the number of cells that migrated through 3, 5 and 8 µm pore filters. The main difference between the two cell lines were their morphologies and metastatic potential. The invasive mutant p53 cells have an elongated morphology and tend to be invasive via single cell migration (Figure 4.2A) (Morton et al., 2010). Meanwhile non-invasive deleted p53 cells, their morphologies were semi-rounded and grew in colonies, which meant that these cells could migrate as a collective (Figure 4.2). Prior to quantifying the transwells, DIC images were taken (according to Section 2.3.4 procedure with 20x 0.5 NA objective) so correlation between the cell numbers could be made.

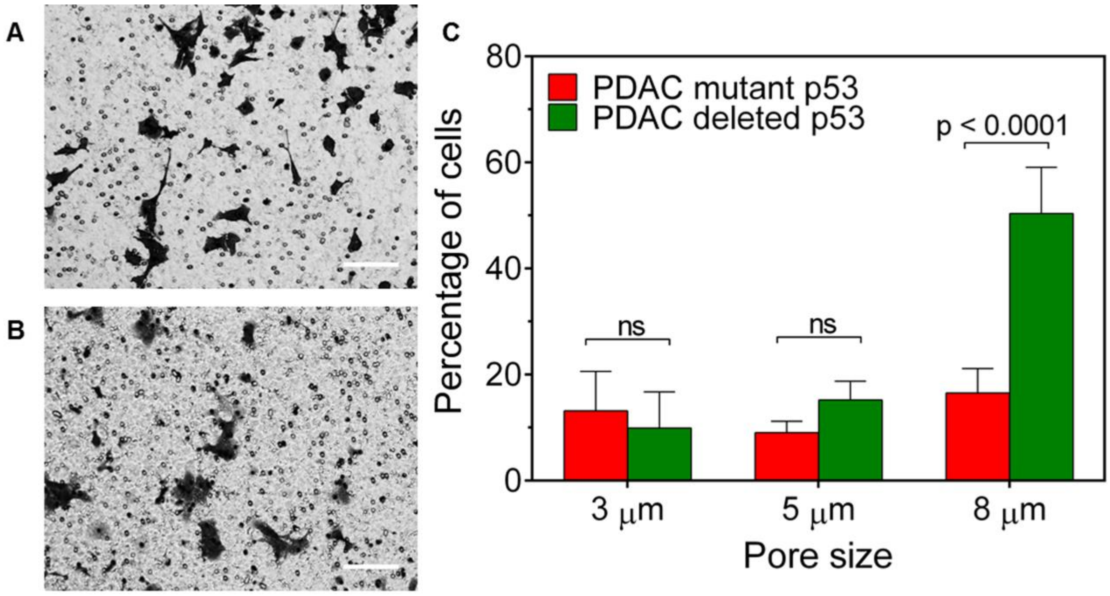

**Figure 4.2│Percentage of migrated cells (PDAC mutant p53 and deleted p53) passed through various pore sizes.** Images displayed of (A) mutant p53 and (B) deleted p53 cells on 8 μm transwell. All scale bars are 50 μm. (C) Percentage of migrated of both cells on 3, 5, and 8 μm transwell (n = 6 wells), expressed as mean ± SD. Less migration was observed with deleted p53 cells compared to its counterpart at 8 μm pore ($p < 0.0001$), though no difference in 3 μm and 5 μm pore sizes.

Using quantitative staining analysis, it was found there was no significant difference between the percentages of migrated cells for mutant p53 cells and deleted p53 cells when using 3 μm and 5 μm transwells. However, for 8 μm transwells more mutant p53 cells migrated compared to deleted p53 cells ($p < 0.0001$; Figure 4.2C).

Percentage of migrated mutant p53 and deleted p53 cells were 13 ± 7% and 9 ± 7% for 3 μm transwells; 9 ± 2% and 15 ± 3% for 5 μm transwells and 16 ± 4% and 50 ± 9% for 8 μm transwells. These trends were also observed with the acquired images of transwell plates (Figure 4.2A and B).

As mutant p53 cells were longer in size and migrate alone, they could pass through the pores easily, whereas deleted p53 cells were rounder and move as a cluster, which could hinder migration. These findings was similar to other studies, whereby single cells were more motile than those involved in sheet/ cluster migration (Clark and Vignjevic, 2015; Friedl and Gilmour, 2009). At smaller pore sizes there were no differences; this might be due to a similarity in nucleus size for both cell lines (measurements later discussed).

The transwell assay was also carried out on modified PDAC cells with EGFP:ER and ROCK1:ER cells, to investigate the effect of overexpression of ROCK1 activity has on cell migration  through confined pores. Increased ROCK1 activity has been shown to increase cell invasion through collagen matrices (see Section 3.6.4). The results showed that overexpression of ROCK1 activity lead to a significant decrease in the percentage of migrated cells through all pore sizes (Figure 4.3).

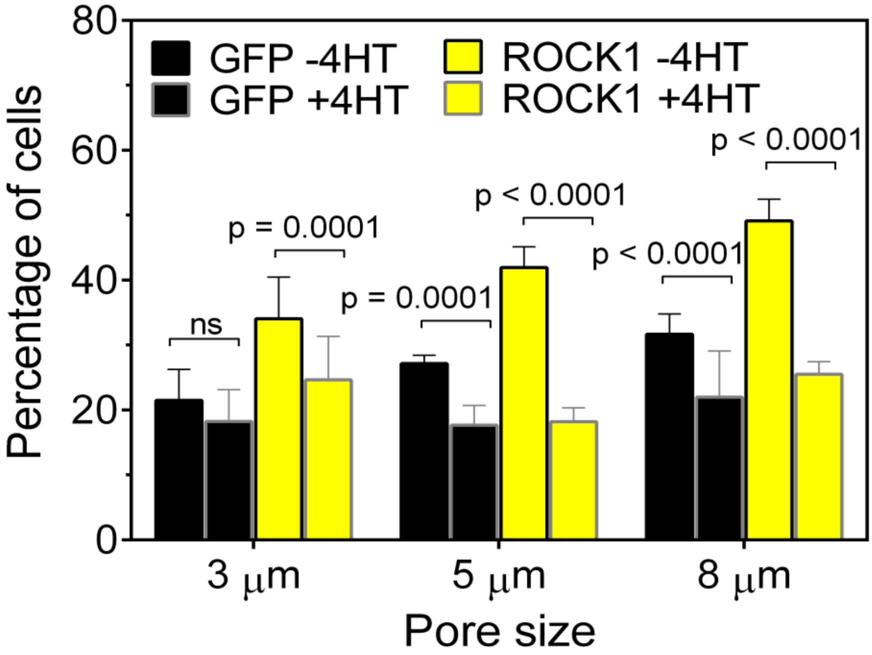

**Figure 4.3│Percentage of migrated cells (EGFP:ER and ROCK1:ER) passed through various pore sizes (n = 6 wells), expressed as mean ± SD.** There was a significant decrease in number of migrated cells when ROCK1 activity was overexpressed, though these were also view in the control.

The percentage of migrated cells decreased from 34% to 25% in the 3 μm transwells, from 42% to 18% in the 5 μm transwells and from 49% to 25% in the 8 μm transwells.  Meanwhile, the EGFP:ER cells exhibited similar tends to the overexpressed ROCK1:ER cells, excluding 3 μm pore size, where only ~ 20% of cells migrated.

These observations regarding ROCK activity were in agreement with other studies that were experimented on the counter argument (Yang and Kim, 2014; Zhang et al., 2011b).  Proliferation and migration increases with ROCK inhibition due to disrupted cell junctions along with a loss of integrins from the membrane.  This means with ROCK activation, actomyosin contraction and the formation of focal adhesions increase, which in turn creates an imbalance between cell-generated forces and the surface (Kole et al., 2004; Lange and Fabry, 2013). Thus, a smaller number of migrated cells would pass through the same pore size.

To summarise, it has been shown that cell migration through restricted pore sizes is dependent on cell morphology and whether isolated or in a group. Overexpressed ROCK1 activity has shown to reduce the number of migrated cells at the same pore size, which may be due to cells undergoing cellular stress along with increased number of focal adhesions, which subsequently impedes on cell movement.

### 4.4.2 Cell migration through microfluidic device

#### 5.4.2.1 *Characterisation of devices*

Microfluidic devices have become a useful tool in cancer research, due to the ability to better control the cellular microenvironment when compared to conventional cell migration assays. Here, we propose a device whereby we observe how cells adapt their shape and migrate through microchannel openings and confined spaces, under a chemotactic gradient.

Prior to cell studies, the device was characterised to see whether a chemical concentration gradient could be established across the microchannels. This was done by investigating the diffusion of 25 μM fluorescein in PBS towards blank PBS, over 10 hours (the duration of the cell migration studies). Fluorescein has been used a fluorescent tracer and can measured using a fluorescence microscope (details in Section 2.3.4; similar to phalloidin stain). The acquired images were processed in ImageJ software, to observe the intensity profile across the microchannels, over the time period.

The intensity profile across the microchannel with 5 μm and 8 μm height showed a steady decrease in profile from the fluorescein solution towards blank PBS, with a gradient of -0.13 arbitrary unit/ μm (Figure 4.4A and B).

Note, although the 15 μm high microchannels did display steady a profile, this was only established after the initial 2 hours (Figure 4.4C). However, this may be due experimental errors as the initial curve is similar to the later acquired curves, excluding 1 hr and 2 hr curves. The gradient in these channels was significantly smaller at -0.06 arbitrary unit/ μm (a.u./ μm).

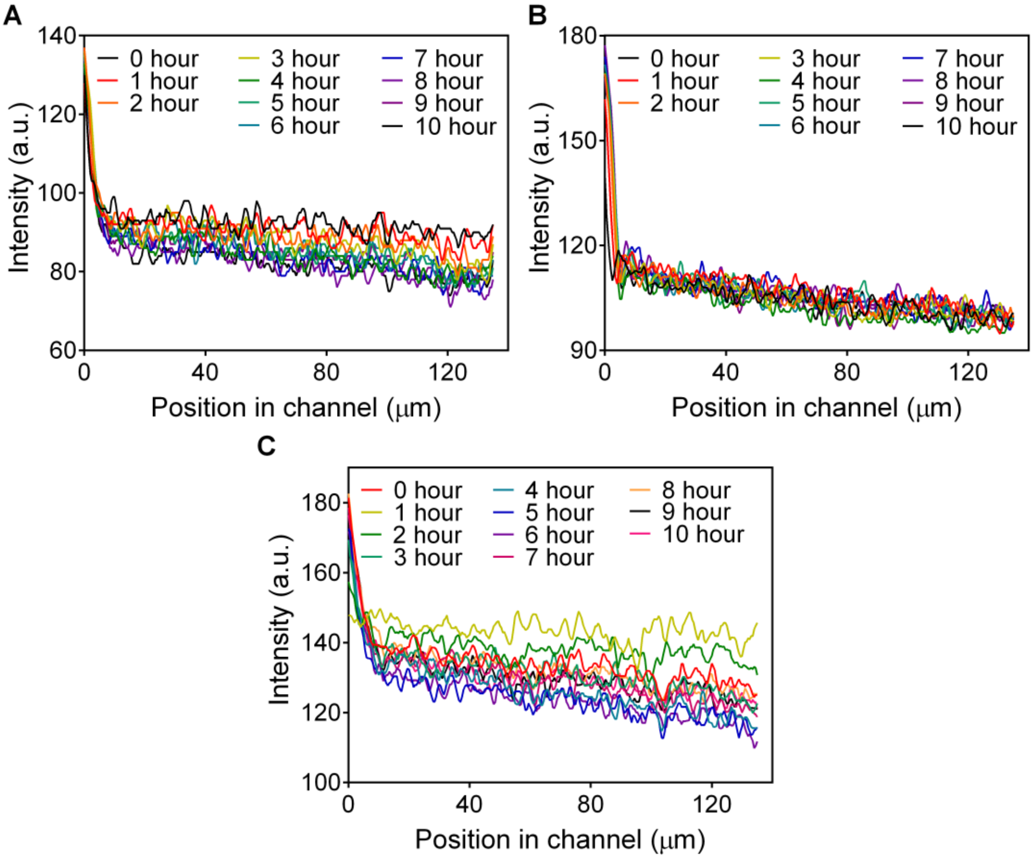

**Figure 4.4│Chemical gradient established over a 4 µm microchannel of various heights using fluorescein and PBS, over 10 hours.** The heights of the microchannels include (A) 5 µm, (B) 8 µm and (C) 15 µm.

Although fluorescein has shown to establish a steady gradient, this is different to the chemoattractant (serum) used. According to Fick's law of diffusion (the diffusion flux is proportional to the concentration gradient) an increase in molecular weight of molecules can increase the diffusion coefficients. Fluorescein has a molecular weight of 332.31 g/mol (Sigma Aldrich datasheet), whilst serum has a molecular weight of 66.12 g/mol (Sigma Aldrich datasheet). Therefore diffusion would occur faster with the chemoattractant compared to our test sample.

Using the calculated gradients above, I can work out whether the channel widths have an effect on the chemical gradient (Figure 4.4 and Table 4.2). According to the table, there is minimal difference between the chemical gradients in different channel widths, for each channel height device. These findings show that the microchannels were clear, however, it is possible that channels can be blocked (i.e. cells). If this occurs, this would cause the chemical gradient to be unbalanced; as the cell would only exhibit no chemical or chemical environments.

**Table 4.2│A table outlining the calculated chemical gradient for each channel dimension.**

| | Chemical gradient (a.u./ µm) | | |
|---|---|---|---|
| | 3 µm | 4 µm | 5 µm |
| 5 µm | -0.10 | -0.13 | -0.17 |
| 8 µm | -0.10 | -0.13 | -0.17 |
| 15 µm | -0.05 | -0.06 | -0.08 |

Once we understood that a chemoattractant gradient could be established, we decided to carry out an initial study on the 15 µm height device, to see whether mutant p53 cells would migrate into the channels via tapered and abrupt openings. As seen from the images recorded over 5 hours, it was a proven success that the cells travelled through the microchannels with both channel openings (Figure 4.5). Although from the images, we was noticed that our cells travelled at a very slow rate, henceforth longer cell migration studies were required in order to understand the cell's migratory behaviour.

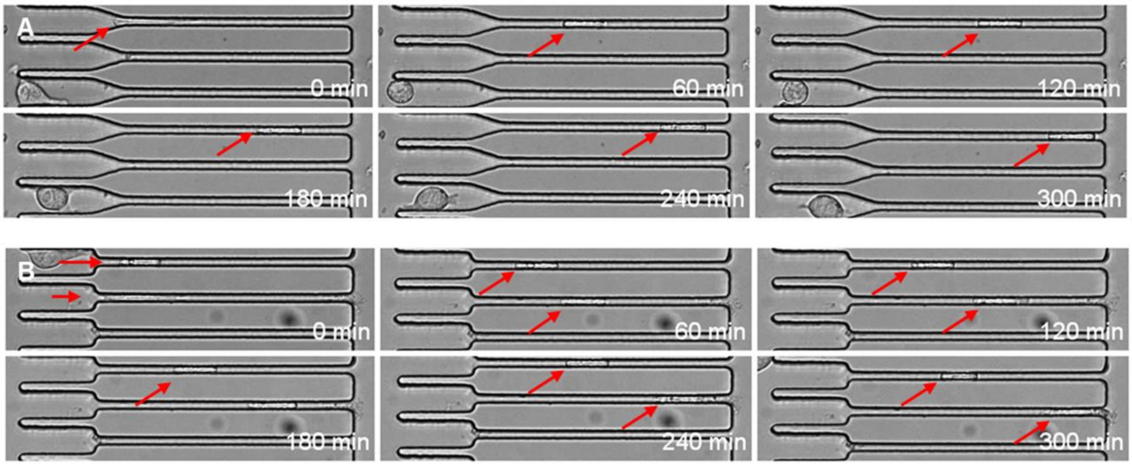

**Figure 4.5│Time-lapse images of PDAC mutant p53 cells travelling through 3 µm x 15 µm microchannels, over 5 hours.** Red arrows indicate the movement of cells through the channel. Cells passed through (A) tapered and (B) abrupt openings.

Here, I have shown that a steady fluorescein gradient was established in all the microfluidic devices for over 10 hours. This indicates that by applying serum-free and serum media to the channel, a chemotactic gradient could be present.

#### 5.4.2.2 *Effect of microchannel openings on cell migration*

The PDAC mutant p53 and deleted p53 cells were placed in the microfluidic devices, to investigate the effect of geometry of the microchannel openings and confined spaces on cell migration. From the cell migration experiments, the number of migrated cells into the channels, the length of cells and the migration velocity were obtained. The cell lengths were measured at 2, 6, and 10 hour intervals. To understand whether the collected measurements at different times had an effect on the final values, we gathered data from the smallest and largest cross sectional area of the channels, for both mutant p53 and deleted p53 cells. The reason to use both cell lines was due to their difference in morphology that could be associated with the cell length measurements (Figure 4.6). The surface area of the cells was measure from optical images using ImageJ software. The average surface area for mutant p53 cells was 430.14 ± 75.20 μm$^2$ (n = 12 cells), whereas 272.88 ± 69.59 μm$^2$ (n = 12 cells) for deleted p53 cells.

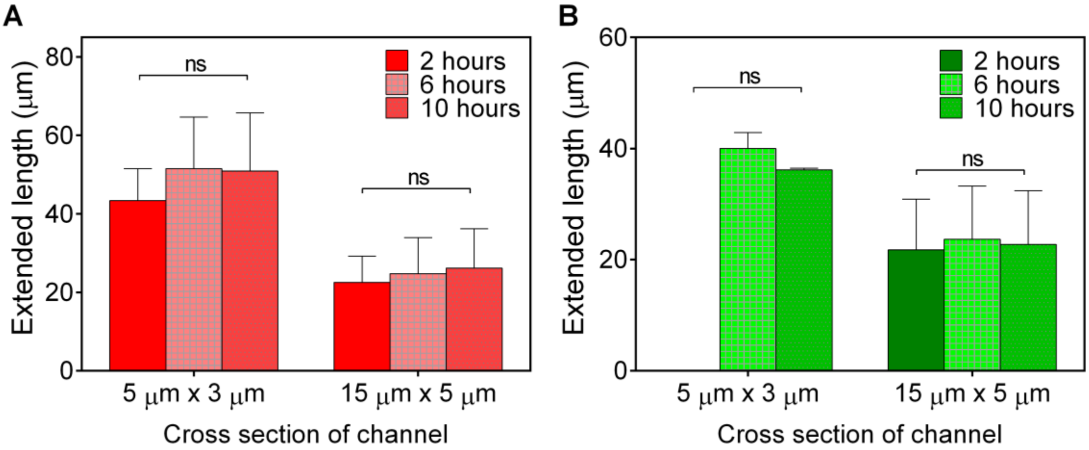

**Figure 4.6│Effect acquired extended length measurements carried out on large and small cross sectional microchannels at different times (n = 3 devices), expressed as mean ± SD.** Two type of cells used; (A) PDAC mutant p53 and (B) deleted p53 cell. Although the measurements for different times were insignificant, a decrease in cross sectional area increases the extended lengths.

According to the results, there was no significant difference between the data collected at different time points from either small or large cross sectional area of the microchannel. This meant that it was not necessary to measure cells at different time points. Henceforth, all the measured cell lengths from the different time points were collected together and discussed as one, in these cell migration studies.

Now, here we can investigate the effect of physical stimuli (microchannel openings) have on cell migration. Tapered and abrupt openings were used, as these two covered the extreme geometries to stimulate cells at the interface of the microchannels. For these discussions, we compare the effect on cells in 5 μm and 15 μm high microchannels; showing both extremes of the dimensions created.

The results showed that there was no significant difference between the openings of microchannel in both cell lines in 15 μm high microchannels (Figure 4.7). In addition, it was noticed that there was no statistical difference between the two cell lines due to the large distributions.

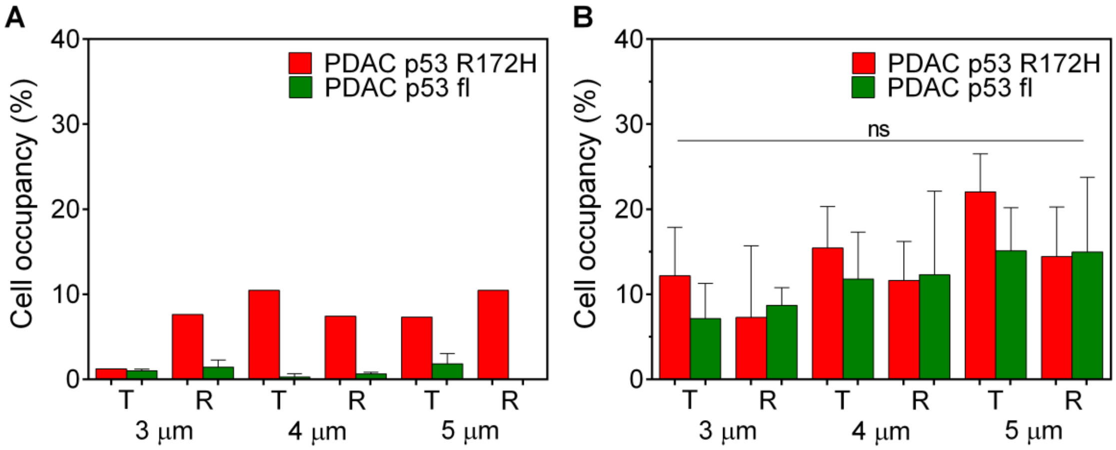

**Figure 4.7│Comparison between PDAC mutant p53 and deleted p53 cells moving into tapered (T) and abrupt (R) channel openings in 5 μm (A) and 15μm (B) height channels with three different channel widths (i.e. 3, 4, and 5 μm), expressed as mean ± SD from n = 3 devices.** On average there are less deleted p53 cells occupied in the microchannel as oppose to its counterpart. No significant difference between the two channel openings against cells.

For 5 μm high microchannels, due to the lack of data collected for this dimension, we were unable to do any statistical analysis. However, more cells migrated into 15 μm high microchannels, as oppose to 5 μm high ones. In the 5 μm high microchannels, the average percentage of cell occupancy was between 1–10% (n = 806 cells) for mutant p53 cells, whereas the average percentage of cell occupancy was between 0–2% (n = 1807 cells) for deleted p53 cells.

In the 15 µm high microchannels, the average percentage of cell occupancy was between 7–22% (n = 1909 cells) for mutant p53 cells, whereas the average percentage of cell occupancy was between 7–15% (n = 2689 cells) for deleted p53 cells. Although there was no statistical difference, the averages of the two cell lines suggest that mutant p53 cells migrate more easily through narrow channels. This can be explained by observations of the cell size and the ability for mutant p53 cells to squeeze through narrow microchannels (Lautscham et al., 2015).

Once cells have entered into the microchannel through the opening provided, we can observe how cell length could have been affected by the geometry of the opening (Figure 4.8).

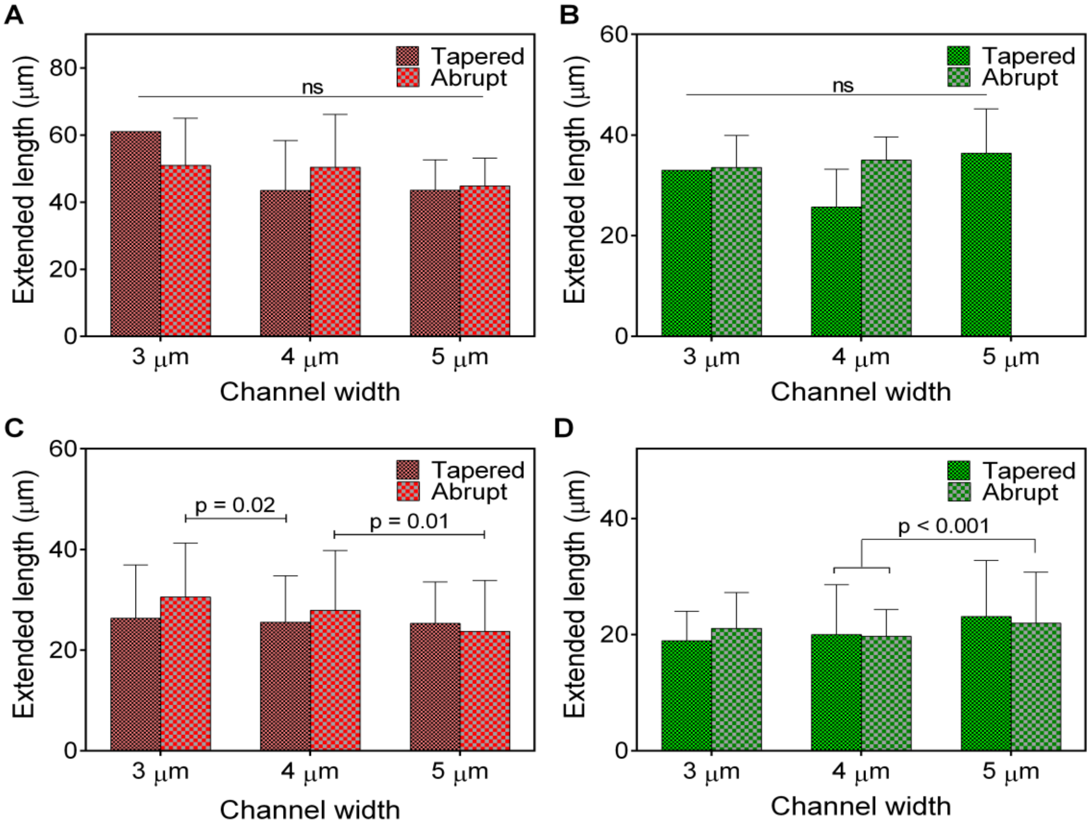

**Figure 4.8│Comparison between channel openings and extended lengths (PDACs) generated within the channel (n = 3 devices), expressed as mean ± SD.** No statistical difference between channel openings and cell length in (A & B) 5 µm and (C & D) 8 µm heights, though there were difference shown in channel widths. The cells used were (A & C) PDAC mutant p53 and (B & D) deleted p53 cells.

According to the data, it showed that there was no statistical difference between the two types of opening, for 5 μm high microchannels. In the 5 μm high microchannels, the average cell length was between 43–61 μm (n = 119 cells) for mutant p53 cells, whereas the average cell length was between 26–36 μm (n = 25 cells) for deleted p53 cells. These results showed that the cell lengths were different between mutant p53 and deleted p53 cells, under confined spaces. This could be explained by the cell's morphology; mutant p53 cells exhibit an elongated shape that contains a larger surface area and hence large cell volume. Therefore, mutant p53 cells would have needed to stretch more to maintain their volume in these confined spaces.

Although there was no difference between the channel openings, there was a significant difference between some of the channel widths for both cells in the 15 μm high channels ($p < 0.02$). These differences were mainly observed in channels with wide dimension; 4 μm and 5 μm. Discussion on the correlation between changes in channel dimensions to cell migratory behaviour will be reviewed later.

The cell migration velocities were calculated based on the overall distance a single cell travelled over a period of time (Figure 4.9). It was observed that cells could have travelled continuously for the entire 10 hours, although majority of the cells were stationary for some of the time. This effect has been shown in breast, prostate and colon carcinoma cells that alternate between motile and stationary phases as they migrate through 3D collagen (Niggemann et al., 2004).

Cell migration velocities were shown to be unaffected by channel openings in both cell lines and microchannel heights. In the 5 μm high microchannels, the average migration velocity was between 0.20–0.30 μm/ min (n = 47 cells) for mutant p53 cells, whereas the average migration was between 0.20– 0.39 μm/ min (n = 17 cells) for deleted p53 cells. Meanwhile, in the 8 μm high microchannels, the average migration velocity was between 0.31–0.42 μm/ min (n = 167 cells) for mutant p53 cells, whereas the average migration velocity was between 0.24–0.40 μm/ min (n = 198 cells) for deleted p53 cells.

The findings here suggest that the migration velocities were not affected so much by channel widths, but more by channel heights. In the literature, it has been shown that cells reduced in cell velocity as dimensions were reduced from 50 μm to 3 μm widths with a channel height of 10 μm (Tong et al., 2012). These trends were also seen when cells had a channel height of 3 μm and the widths reduced from 25 μm to 6 μm (Irimia and Toner, 2009). However, when the channel height was 12 μm, cell motility was not affected by channel width. This suggests that migration velocities are highly dependent on the cross-sectional aspect ratio of the confined space, although it remains unclear whether velocities are dependent on channel height, width or the overall cross sectional area difference. If our data displayed the volume of the cells had filled the different aspect ratio of the microchannels, the migrated velocity could change according to the amount of cell contact to the glass substrate (later discussed in detail).

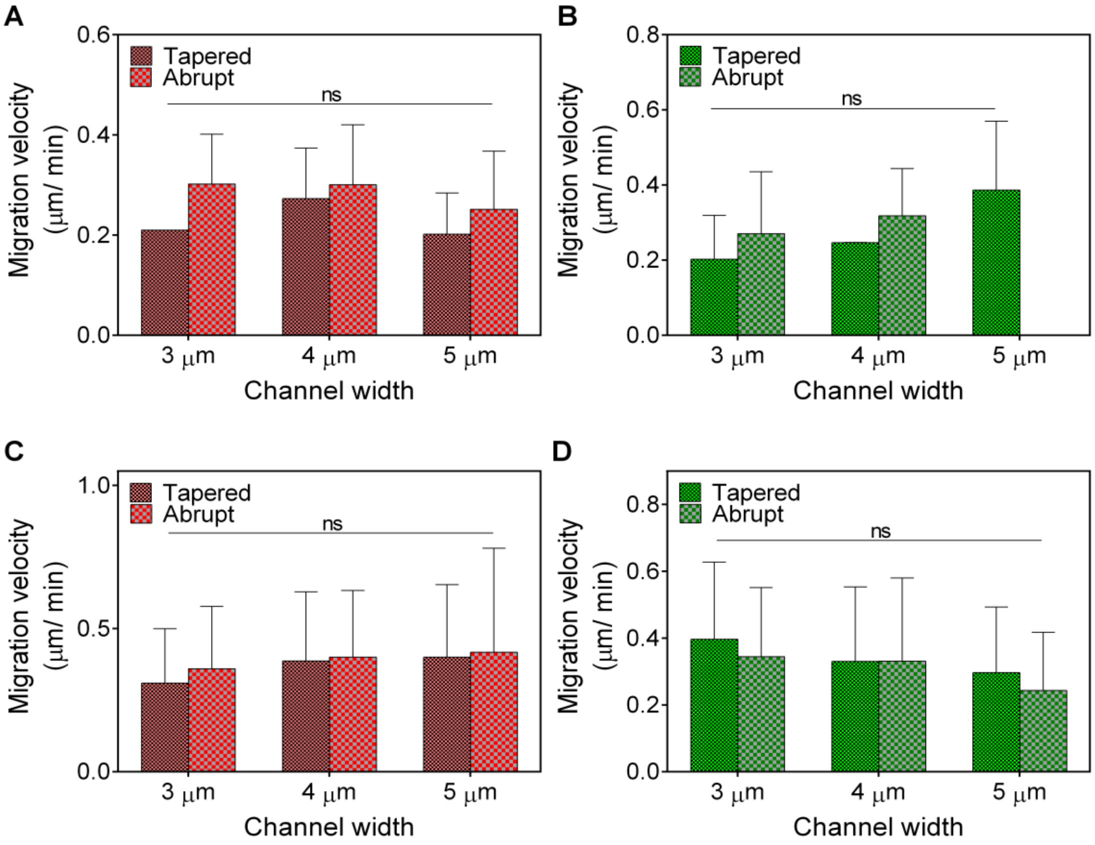

**Figure 4.9│Comparison between channel openings and the cell lengths (PDACs) generated within the channel (n = 3 devices), expressed as mean ± SD.** No statistical difference between channel openings, and widths on cell velocity in (A & B) 5 μm and (C & D) 8 μm heights. The cells used were (A & C) PDAC mutant p53 and (B & D) deleted p53 cells.

Within this subsection, we have shown that channel opening did not affect cell migration properties, though they can inhibit cell migration into the channels. Henceforth, the datasets from the two channel openings were collected together and discussed as one. We have shown that there could be a possible 22% increase in cell migration into the channels for both mutant p53 and deleted p53 cells when going from 5 μm to 15 μm channel heights. This can be explained as migrating properties can be altered according to the cell contact ratio between glass and PDMS (Figure 4.1C). The aspect ratio of the microchannels can be defined by the contact ratio. If the contact area was glass >> PDMS, cells could spread out on the substrate forming stronger focal adhesions, which could lead to slow migration. On the other hand, if contact area was glass << PDMS, cells could not spread onto the surface, hence weaker focal adhesions, which could lead to faster cell migration. Another explanation could be associated with the cell nucleus. There has been an indication that cell nucleus was the main component that undergoes steric hindrance, hence without a change in its mechanical behaviour, it can prevent migration of cells occurring in confined spaces (Lautscham et al., 2015).

#### 5.4.2.3 *Effect of cross sectional area on cell migration*

To address the effect of channel dimensions on cell migration behaviour, we created a range of confined channels with cross sectional areas ranging between 15–75 $\mu m^2$. These dimensions were chosen to provide a difference between confinement and non-confinement both across and above the cell body. As aforementioned, the nucleus is the main component within the cell that has to undergo confinement and hence, prior to cell migration studies, we measured the heights and widths of the nuclei for the various cell types studied.

For nuclei height measurements, both mutant p53 and deleted cells were cultured and measured using atomic force microscopy. This was carried out by observing the difference in piezo movement from the surface to the apex of the nucleus. A sample size of 150 cells was measured for each cell line. The average height was 6.36 ± 2.22 μm for mutant p53 cells and 6.98 ± 1.88 μm for deleted p53 cells.

To measure the width of the nucleus, the cells were fixed and stained with DAPI, so the nucleus can be visible using fluorescence microscopy. The cells were exposed for 0.3 seconds and an image captured at 40x, 0.75 NA objective (details in Section 2.3.4). Five captured images were analysed using ImageJ software, to measure the smallest distance across the span of the nucleus. The average nucleus width measured was 10.97 ± 1.49 μm for mutant p53 cells, whereas it was 9.73 ± 1.15 μm for deleted p53 cells.

Overall this means that the average cross sectional are these cells would be 69.77 ± 3.31 $\mu m^2$ for mutant p53 cells and 67.92 ± 2.16 $\mu m^2$ for the deleted p53 cells. Therefore channel dimensions of 15 μm heights with 4 and 5 μm widths may not strongly confine the cells, although they could be restricted in one or other dimension.

Firstly, we discuss the effect of the channel dimensions on the percentage of migrated cells in the narrow channels. For both cell lines, there was a decrease in number of cells that migrate into the channels as the channels become narrower ($p < 0.004$ for deleted p53 cells and $p < 0.01$ for mutant p53 cells; Figure 4.10).

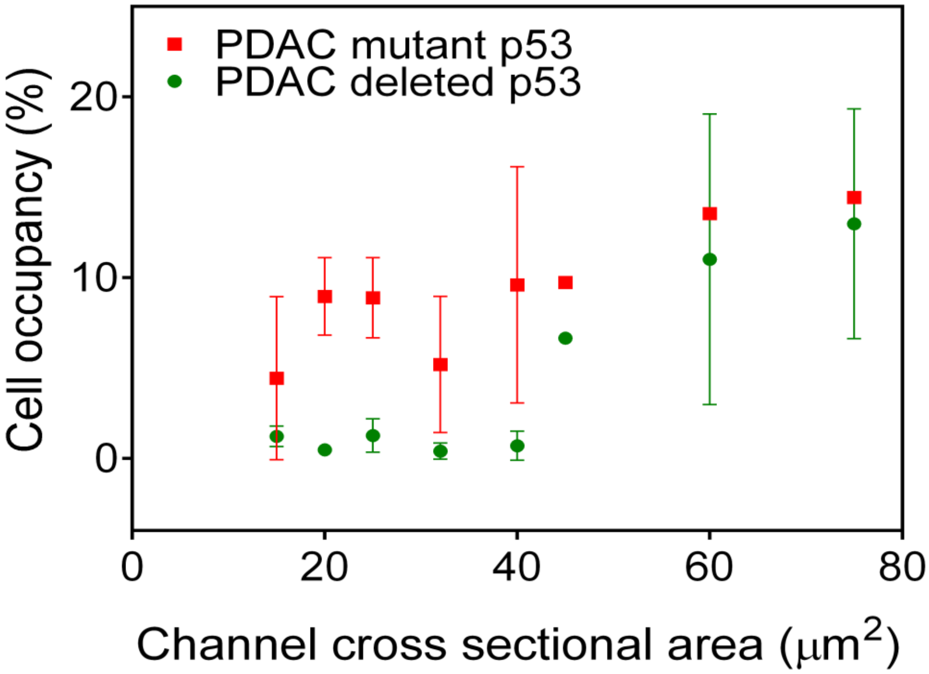

**Figure 4.10│Comparison between cell occupancy (PDAC p53 cells) in microchannels against its cross sectional area (n = 3 devices), expressed as mean ± SD.** A gradual decrease in cell occupancy as channels gets narrower ($p < 0.004$ for deleted p53 and $p < 0.01$ for mutant p53 cells). The mutant p53 cells tend to migrate into the narrow channels more than its counterpart cells.

This has been suggested to be related with the nucleus, whereby it requires deformation in an elongated manner (Lautscham et al., 2015). As the cross sectional area of the channel decreases, the ability for cells to deform in such manner decreases too, thus hindering cells entering the opening of the microchannel.

The mutant p53 cells were shown to migrate into the channels more than the deleted p53 cells ($p < 0.01$). These observations made here were in agreement with the transwell study. However, with use of the microfluidic device and the guided openings, we can detect a difference between the cells here as oppose to the transwell data.

Once the cells have migrated into the channel, it has been shown that the measured cell lengths within the channels were affected by channel size. In both cell lines, an increase in cell lengths was observed when channel sizes were decreased (Figure 4.11). This meant that as the channels became narrower the cells could have sensed the substrate confinement and in turn rearranged their cytoskeleton. This elongated morphology was said to be related to generation of active actomyosin forces to maintain the cytoskeletal structure, through microtubules (Nasrollahi and Pathak, 2016).

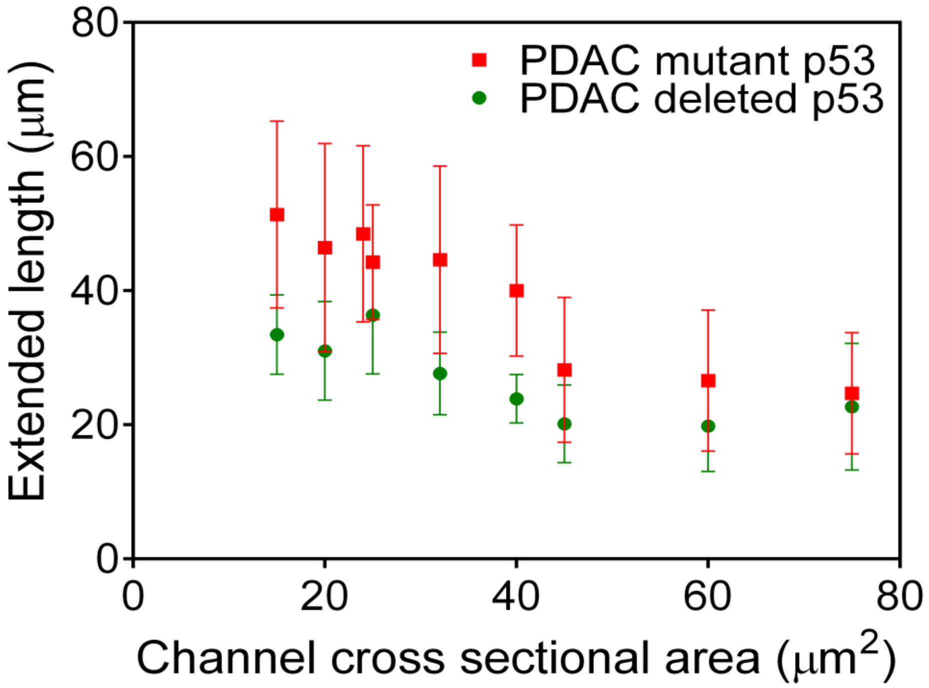

**Figure 4.11│ Comparison between cell length (PDAC p53 cells) in microchannels against its cross sectional area (n = 3 devices), expressed as mean ± SD.** A gradual increase in cell lengths with decrease channel size. The mutant p53 cells tend to elongate along the narrow channels more than deleted p53 cells.

Due to the large distributions between the datasets, there were no statistical differences between the two cell lines. However, from the optical microscopy observations we can see that mutant p53 cells elongate more than the deleted p53 cells. Both statements can be explained by the difference in cell size. If we consider the nucleus alone, both cells have similar dimensions, hence their squeezing ratio (cross section area of non-deformed nucleus against cross sectional area of confinement space) would be the same as the channel sizes were reduced.

On the other hand, if we consider the cell as a whole, mutant p53 cells (surface area = 430.14 ± 75.20 µm$^2$; n = 12 cells) have a cell size larger than deleted p53 cells (surface area = 272.88 ± 69.59 µm$^2$; n = 12 cells). These larger cells require more elongation to enter into narrower confinement compared to smaller cells (Khan and Vanapalli, 2013).

Finally the migration velocities were studied against the channel sizes. From the results, it was shown that there was no difference between the migration velocities of cells as the channel size decreases (Figure 4.12).

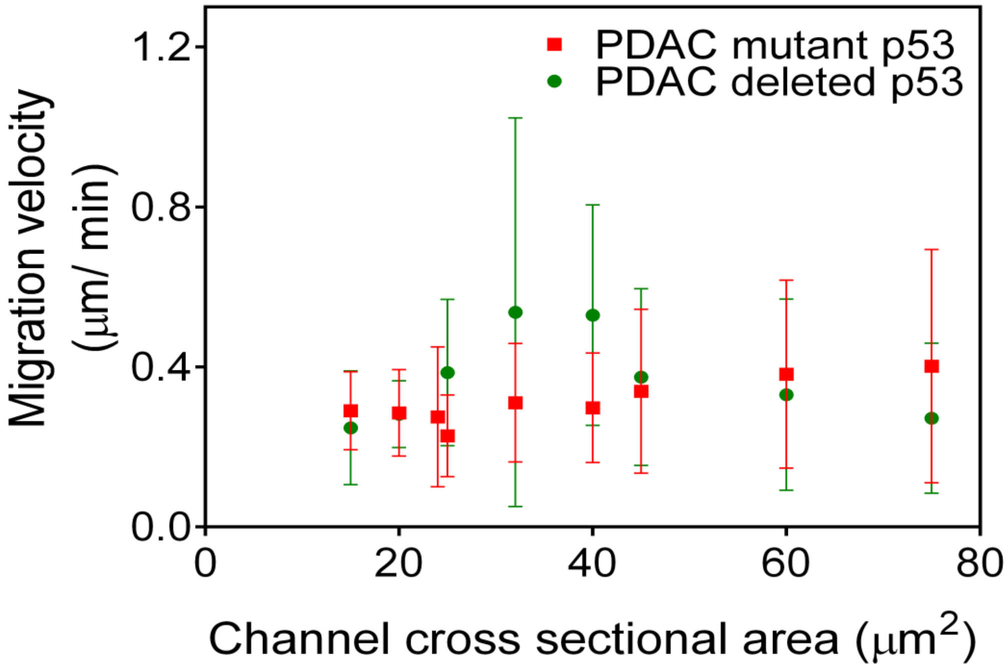

**Figure 4.12│ Comparison between migration velocity of PDAC p53 cells in microchannels against its cross sectional area (n = 3 devices), expressed as mean ± SD.** No statistical difference between migration velocity and the channel size, in both cell lines.

This trend was observed in both cell lines. The migration velocities are said to be dependent on cell stiffness, nuclear volume, cell adhesiveness and contractility (McGregor et al., 2016). With this in mind, our results indicate that both mutant p53 and deleted p53 cells may be exhibiting similar cellular behaviours, under confinement. The average migration velocity for the cell lines were between 0.23–0.53 µm/ min. These low speeds suggests that cells were migrating on stiff substrates (PDMS, E = 1.77 MPa; glass, E = 70 GPa), hence having a larger spreading area and in turn more focal adhesions on the each cell (Lange and Fabry, 2013; Lautscham et al., 2015).

To summarise, I have shown that channel dimensions could affect both the degree of cell movement and elongation through narrow channels. These factors have been shown to be associated with the size of the nucleus and its ability to squeeze through microchannels. As there was no statistical difference between the mutant p53 and deleted p53 cells, it has also been noted that their cellular behaviour could be similar during confinement.

#### 5.4.2.4 *Effect of overexpressed ROCK on cell migration*

Overexpression of ROCK1 activity was investigated to understand its effect on the mechanical and migratory properties when cells undergo confinement. Cells were only examined in 15 µm channel height devices, as it had been found that more cells migrated into these channels. Furthermore, this would provide a larger sample size for the study, and gain a better overview of any differences between the cells. As aforementioned, a cell’s migratory behaviour has been shown to be dependent on the channel size and thus 3, 4 and 5 µm channel widths are also addressed in the discussion.

For ROCK1:ER cells to overexpress ROCK1 activity, estrogen treatment of the cells for more than 18 hours is required. For this reason, cells were cultured in estrogen treatment a day prior to cell migration studies, and kept under treatment during the time-lapse imaging. As a control, this procedure was also carried out in a similar manner for EGFP:ER cells.

Firstly, we observe the effect of overexpression of ROCK1 activity on the number of cells that entered into the channels. It was shown that no significant difference between estrogen treated and untreated cells in both EGFP:ER and ROCK1:ER cells (Figure 4.13). In addition, there was no difference between the channel widths against any of the cells measured. However, there were two statistical differences observed with EGFP:ER -4HT cells at 3 μm channel against ROCK1:ER -4HT cells at 4 μm ($p < 0.04$) and at 5 μm ($p < 0.02$).

The average percentage of cells that occupied a microchannel was 7–13% (n = 1840 cells) for EGFP:ER -4HT cells, whereas the average percentage of cell occupancy was 10–14% (n = 2114 cells) for EGFP:ER +4HT cells. Meanwhile, for ROCK1:ER -4HT cells the average number of cells that occupied a microchannel was 11–16% (n = 1957 cells) and 10–13% (n = 2044 cells) for ROCK1:ER +4HT cells. These values were compared to parental (deleted p53) cells, and it was noticed that the percentage of cells occupying a channel were very similar.

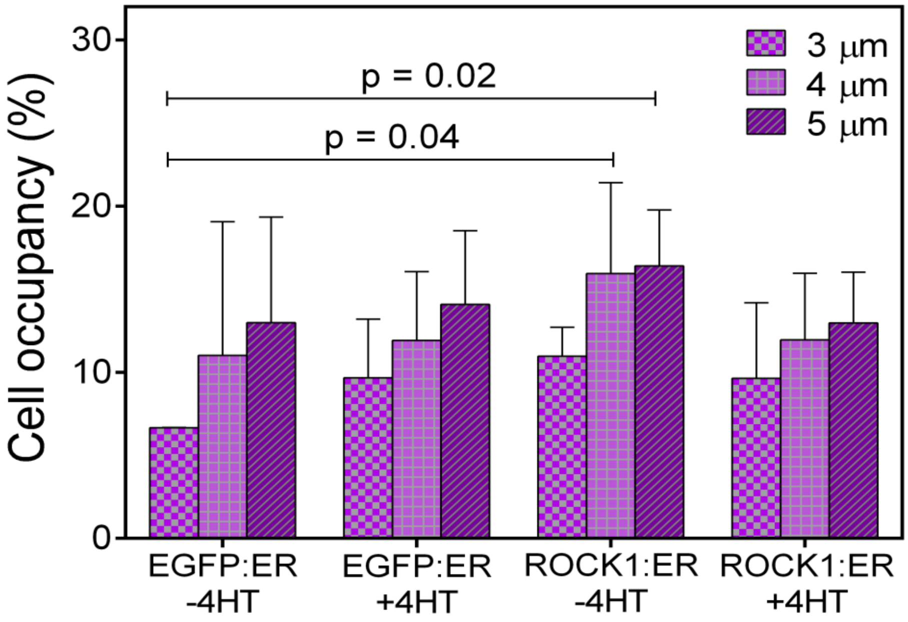

**Figure 4.13││Comparison between EGFP:ER and ROCK1:ER in relation to cell occupancy within a microchannel following estrogen treatment (n = 3 devices), expressed as mean ± SD.** No significant difference between numbers of cells entered into the microchannels and treatment to cells.

These findings contradict the data that was collected in the transwell assay, which indicated a difference between over and normal expression of ROCK1 activity; in particular there was a decrease in the number of migrated cells. This may be due to cell-cell interaction prior to entering the pores in the transwell plates, meanwhile no cell-cell interaction present prior to entering the channels in microfluidic devices (see Figure 4.5) (Lee et al., 2012).

Once cells have entered into the channel, these migrate towards the serum media in the opposite chamber. As the cells fill the channel, measurement of their lengths were obtained. The results showed that for each of the cell lines, there was no significant difference in cell length for different channel widths. However, it was noticed that there was a statistical difference between the estrogen treated and untreated for in both cell lines ($p < 0.0001$; Figure 4.14).

The average cell length was 19–22 μm (n = 734 cells) for EGFP:ER -4HT cells, whereas the average cell length was 14–16 μm (n = 758 cells) for EGFP:ER +4HT cells. Meanwhile, the average cell length was 17–20 μm (n = 793 cells) for ROCK1:ER -4HT cells, whereas the average cell length was 16 μm (n = 725 cells) for ROCK1:ER +4HT cells. It was shown that an average reduction in cell length between untreated and treated cells was ~ 26.5% and 6–20% for EGFP:ER and ROCK1:ER cells, as respectively.

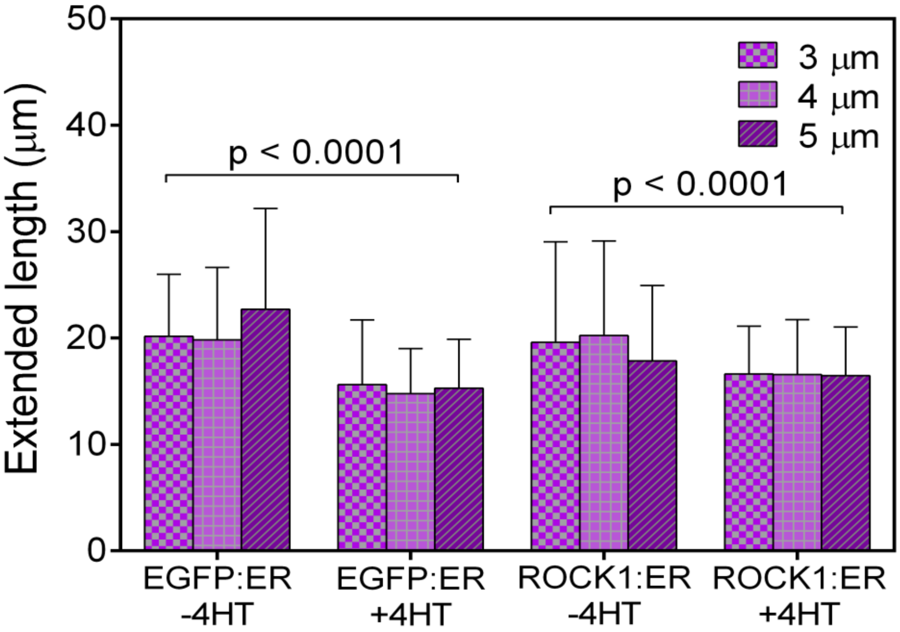

**Figure 4.14│ Comparison between EGFP:ER and ROCK1:ER in relation to cell lengths within a microchannel following estrogen treatment (n = 3 devices), expressed as mean ± SD.** A reduction in cell length in both EGFP:ER and ROCK:ER cells following treatment ($p < 0.0001$).

As aforementioned, ROCK activation in cells leads to actomyosin contraction and in turn causes change in cell morphology to a rounded state (Kole et al., 2004; Lochhead et al., 2010). This is in agreement with the observation seen for overexpressed ROCK1:ER cells, as the morphology changes to a smaller size that in turn would occupy a smaller area (length) within the channel. As EGFP:ER cells followed similar trends to ROCK1:ER cells, it could be thought that EGFP:ER cells may have undergone overexpression too. This was also noticed in viscoelastic measurement of these cells, as EGFP:ER changed its viscoelastic behaviour after estrogen treatment in a similar way to the ROCK1:ER and ROCK2:ER cells (Section 3.6.4).

Overexpression of ROCK1 activity has been shown to significantly decrease migration velocities as they move through confined channels ($p < 0.01$; Figure 4.15). Meanwhile, there was no difference between treated and untreated EGFP:ER cells. Again, the channel widths were not affected by any cell lines.

The average migration velocity was 0.27–0.37 µm/ min (n = 198 cells) for EGFP:ER -4HT cells, whereas the average cell migration velocity was 0.18–0.31 µm/ min (n = 30 cells) for EGFP:ER +4HT cells. Furthermore, the average cell migration velocity was 0.54–0.66 µm/ min (n = 151 cells) for ROCK1:ER -4HT cells, whereas the average cell migration velocity was 0.27–0.36 µm/ min (n = 28 cells) for ROCK1:ER +4HT cells. An average reduction in migration velocity by 45–50% was observed due to overexpression of the ROCK1 activity.

Although our mechanical data showed overexpression of ROCK1 activity leads to a decrease in elastic behaviour, which would suggest enhanced ability for cells to squeeze through confined spaces (Rolli et al., 2010). These observations were not found in our migration studies, as overexpressed ROCK1 has been shown to reduce motility. These findings are in agreement with other studies that showed the counter argument that ROCK inhibition increases cell motility, due to up-regulated Rac1 activity (Kümper et al., 2016; Lange and Fabry, 2013; Yang and Kim, 2014). This has been thought to be associated with the disruption of cell junctions and produce less membrane protrusions; lamellipodia.

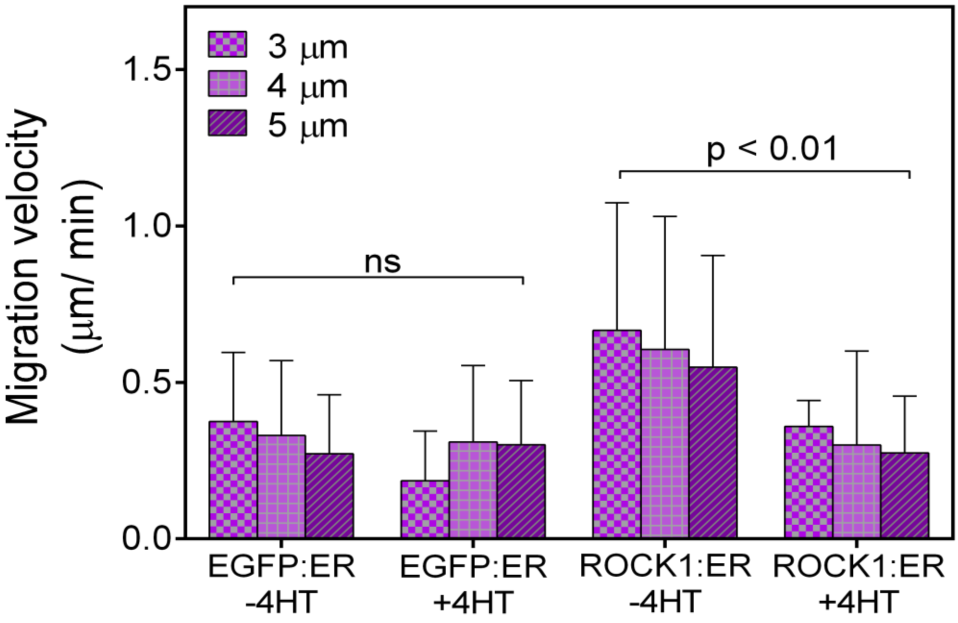

**Figure 4.15│ Comparison between EGFP:ER and ROCK1:ER in relation to migration velocity within a microchannel following estrogen treatment (n = 3 devices), expressed as mean ± SD.** Overexpression of ROCK1 activity displayed a decrease in migration velocities ($p < 0.01$).

Within this subsection, I have shown that overexpression of ROCK1 activity reduces both cell length and migration velocity, under confined space. Overexpression of ROCK1 activity has been shown to lead to cell contraction, thus the reduction in cell size that was observed in the reduction of cell length in the channels. Furthermore ROCK1 activity has been shown to inactivate Rac1 activity and in turn fewer membrane protrusions, leading to a slow migration speed (Yang and Kim, 2014).

## 4.5 Conclusions

We have developed a high-throughput microfluidic platform, to investigate mechanical and migratory behaviour of various cells. The advantages of this device include ability to screen a large sample size, and to acquire real-time imaging of cell migration through chemical and physical stimuli. The results showed that the migratory properties of PDAC mutant p53 and deleted p53 cells were unaffected by the geometry of channel openings, though changed with channel cross-section dimensions. As the channels got narrower, this reduced the cells ability to migrate through the channels, and when in the channels, the cells required more deformation to travel through them. In addition, it was found that there was no difference between the migration properties of mutant p53 and deleted p53 cells, which could indicate that their cellular behaviour was similar under confinement. Alongside, this study, we observed that overexpression of ROCK1 activity showed a reduction in cell motility and size within the microchannels. These findings were in agreement with the transwell assays, although the microfluidic devices provided us with added information regarding the cells. The interest of the studies was to correlate cell mechanics to cell migration and in turn understand how cells invade through tissues. To narrow the gap between the two behaviours in cells, we should further investigate the possible difference in cell mechanics from pre-, during and post- migration, how actin changes during cell migration when cells were overexpressed with ROCK1 activity, and the effect of overexpression of Rac1 and ROCK1 activities on cell migration.

# Chapter 5 Conclusions and Future Work

## 5.1 Abstract

Within this chapter, we will conclude on the overall findings obtained from the studies outlined in this thesis, and discuss future investigations that could be taken.

## 5.2 Overall findings and conclusions

Cell mechanics are one of the fundamental facets of cell behaviour that determine cell migration. The inter-connection between the various mechanical properties could increase our understanding on diseases such as cancer, and offer potential developments in disease diagnostics and therapeutics. These interactions were the motivation of the research described here. This research used several established models, to investigate the elastic and viscoelastic properties of particular cancer cell types and their influence on migratory properties in confined spaces.

Initially, using an established AFM set-up, we took both primary keratinocyte cells and PDAC pancreatic cancer cells that were conditionally active with either ROCK1 or ROCK2 protein, to measure their elastic properties. Measurements were also made on the downstream proteins related to the ROCK pathway: cofilin, LIM kinases, and MLC. It was found that overexpression of ROCK activity led to softening of cells in colonies, due to the possible inward stresses generated by actomyosin contraction that pack the cells (Stroka and Aranda-Espinoza, 2010). Furthermore, the mechanical properties from the downstream proteins suggest that ADF/cofilin activity could contribute to the majority of the cellular response from overexpressed ROCK activity.

Elastic properties of cells provide limited information regarding cell’s mechanical behaviour, and so a new procedure known as FT-AFM-M was developed to measure both the elastic and viscous properties of a cell. The establishment of the procedure was outlined in Chapter 3. The advantages of FT-AFM-M are that with one, simple, time-dependent step-strain measurement, we can extract the viscoelastic properties over a continuous and wide range of frequencies. Furthermore, the extraction of these properties does not rely on the use of preconceived models of the cell response. Biologically, we found that PDAC cells can be described as being in a soft glassy material state, however after long periods (t > 30s) of deformation, they could potentially transform into a viscoelastic material. This meant that cell's viscous properties would become more dominant over time. For the overexpressed ROCK activity cells, only elastic properties changed with expression. Moreover, it was found that cell morphology could be a major contributor towards cell mechanics, as both elastic and viscous properties changed with morphology.

Once the mechanical properties of our cells were well understood, these cells were studied in confined spaces, to observe the effect of confinement on cell migration under chemical stimuli. A microfluidic device was created that had precisely defined channel dimensions through which the cells could, or could not, migrate, as detailed in Chapter 4. It was found that the migratory properties of invasive and non-invasive PDAC cells were affected by confinements. As the microchannels were reduced in size, fewer cells were able to migrate into the channels, though cells that did became more elongated in size. This indicated that cell size could hinder cell migration in confined spaces (Lautscham et al., 2015). In addition, the migratory properties for both types of PDAC cells were similar under confinement, which is suggestive that their cellular behaviour was similar too. An overexpression of ROCK1 activity in cells under confinement showed a reduction in cell size and cell motility. This suggests that migration was not dependent on cell mechanics, as smaller and softer cells tend to be more motile (Trepat et al., 2012). These property changes could be associated with cellular contraction that reduces cell size, and inactivation of Rac activity that would reduce the number of membrane protrusions.

In conclusion, we have shown that ROCK activity affected both mechanical and migratory properties. However, the assumption that softer mechanical properties would aid motility was not found within our studies. This indicates that there are other processes involved in bridging the connection between the mechanical and motility properties.

## 5.3 Future work

### 5.3.1 Mechanical properties

The mechanical properties of cells have been shown to change with its properties according to it surrounding environment (Suresh, 2007). Within our studies, we have only observed the effect of overexpression of ROCK activity on single cell line cultured on polystyrene substrates. Utilising FT-AFM-M procedure, future investigations could include observing the effect of ROCK activity when co-cultured with fibroblast cells (known to be present within the collagen extracellular matrix), and measurement of the cells on softer substrates, to mimic the influence of physiological conditions has on the viscoelastic properties. Furthermore, future work would involve investigating the length of time cells would have to be under deformation, before cells change it viscoelastic properties. This would give us a clearer picture of the cellular behaviour within tumour sites.

Collaborators from Beatson Institute of Cancer Research, Glasgow, UK, have shown that cell morphology of MDA-MB231 D3H2L luc breast cancer cells had changed once re-cultured after undergoing cell migration through 3 μm transwells three times. We investigated the elastic properties of these selected cells that had experienced the effect of continuous confinement. It was found that there was a significant reduction in elastic modulus when going from the parental to the selected cells. This indicated that continuous confinement could potential modify cells without genetic or epigenetic modification. Therefore an investigation could be carried out to observe the mechanical change for overexpressed ROCK activity cells before, during and after confinement with the aid of microfluidic devices. As our cells have a semi-rounded morphology, it would be interesting to understand how the mechanical properties of cells change during migration, and whether properties would revert back.

### 5.3.2 Microfluidic device

For the microfluidic studies, it was thought that although we studied a range of cross sectional areas for the channel size, the height or width dimensions separately could contribute to the difference in migratory properties. Further investigation could answer this question, by creating various channel dimensions though keeping the cross sectional area the same, for cells to migrate through. In addition, to understand the effect of overexpressed ROCK activity during cell migration, investigations could include observations of live actin structures in cells within the microchannels, and surface modification of the microchannels.

The fabricated devices have shown to provide high-throughput data, hence this device could be used to screen cells from a small library of siRNAs that corresponds to various actin cytoskeletal or myosin proteins, and observe cell's migratory behaviour change through confined microchannels.  This could potentially help identify any important proteins that modify motility when ROCK activity is overexpressed.

# Chapter 6 References

Addae-Mensah, K.A., and Wikswo, J.P. (2008). Measurement Techniques for Cellular Biomechanics In Vitro. Exp. Biol. Med. *233*, 792–809.

Alao, A.-R., and Yin, L. (2014). Loading rate effect on the mechanical behavior of zirconia in nanoindentation. Mater. Sci. Eng. A *619*, 247–255.

Alcaraz, J., Buscemi, L., Grabulosa, M., Trepat, X., Fabry, B., Farré, R., and Navajas, D. (2003). Microrheology of Human Lung Epithelial Cells Measured by Atomic Force Microscopy. Biophys. J. *84*, 2071–2079.

Alexopoulos, L.G., Haider, M.A., Vail, T.P., and Guilak, F. (2003). Alterations in the Mechanical Properties of the Human Chondrocyte Pericellular Matrix With Osteoarthritis. J. Biomech. Eng. *125*, 323–333.

Al-Kilani, A., de Freitas, O., Dufour, S., and Gallet, F. (2011). Negative Feedback from Integrins to Cadherins: A Micromechanical Study. Biophys. J. *101*, 336–344.

Ashkin, A. (1970). Acceleration and Trapping of Particles by Radiation Pressure. Phys. Rev. Lett. *24*, 156–159.

Baker, L.A., Tiriac, H., Clevers, H., and Tuveson, D.A. (2016). Modeling pancreatic cancer with organoids. Trends Cancer *2*, 176–190.

Bathe, M., Heussinger, C., Claessens, M.M.A.E., Bausch, A.R., and Frey, E. (2008). Cytoskeletal Bundle Mechanics. Biophys. J. *94*, 2955–2964.

Bausch, A.R., Möller, W., and Sackmann, E. (1999). Measurement of Local Viscoelasticity and Forces in Living Cells by Magnetic Tweezers. Biophys. J. *76*, 573–579.

B. W. Stewart, and C. P. Wild (2014). World Cancer Report.

Ben-Ze'ev, A. (1985). Cell-Cell Interaction and Cell Configuration Related Control of Cytokeratins and Vimentin Expression in Epithelial Cells and in Fibroblastsa. Ann. N. Y. Acad. Sci. *455*, 597–613.

Bhat, S., Jun, D., C., B., and S Dahms, T.E. (2012). Viscoelasticity in Biological Systems: A Special Focus on Microbes. In Viscoelasticity - From Theory to Biological Applications, J. De Vicente, ed. (InTech), p.

Bhushan, B. (1990). Contact between Solid Surfaces. In Tribology and Mechanics of Magnetic Storage Devices, (Springer US), pp. 157–230.

Binnig, G., Quate, C., and Gerber, C. (1986). Atomic Force Microscope. Phys. Rev. Lett. *56*, 930–933.

Boccaccio, A., Lamberti, L., Papi, M., Spirito, M.D., and Pappalettere, C. (2015). Effect of AFM probe geometry on visco-hyperelastic characterization of soft materials. Nanotechnology *26*, 325701.

Boureux, A., Vignal, E., Faure, S., and Fort, P. (2007). Evolution of the Rho Family of Ras-Like GTPases in Eukaryotes. Mol. Biol. Evol. *24*, 203–216.

Boyden, S. (1962). The Chemotactic Effect of Mixtures of Antibody and Antigen on Polymorphonuclear Leucocytes. J. Exp. Med. *115*, 453–466.

Brangwynne, C.P., MacKintosh, F.C., Kumar, S., Geisse, N.A., Talbot, J., Mahadevan, L., Parker, K.K., Ingber, D.E., and Weitz, D.A. (2006). Microtubules can bear enhanced compressive loads in living cells because of lateral reinforcement. J Cell Biol *173*, 733–741.

Brekhman, V., and Neufeld, G. (2009). A novel asymmetric 3D in-vitro assay for the study of tumor cell invasion. BMC Cancer *9*, 415.

Brodland, G.W., Veldhuis, J.H., Kim, S., Perrone, M., Mashburn, D., and Hutson, M.S. (2014). CellFIT: A Cellular Force-Inference Toolkit Using Curvilinear Cell Boundaries. PLOS ONE *9*, e99116.

Byfield, F.J., Reen, R.K., Shentu, T.-P., Levitan, I., and Gooch, K.J. (2009). Endothelial actin and cell stiffness is modulated by substrate stiffness in 2D and 3D. J. Biomech. *42*, 1114–1119.

Cameron, J.M., Gabrielsen, M., Chim, Y.H., Munro, J., McGhee, E.J., Sumpton, D., Eaton, P., Anderson, K.I., Yin, H., and Olson, M.F. (2015). Polarized Cell Motility Induces Hydrogen Peroxide to Inhibit Cofilin via Cysteine Oxidation. Curr. Biol. *25*, 1520–1525.

Carl, P., and Schillers, H. (2008). Elasticity measurement of living cells with an atomic force microscope: data acquisition and processing. Pflüg. Arch. - Eur. J. Physiol. *457*, 551–559.

Chaw, K.C., Manimaran, M., Tay, F.E.H., and Swaminathan, S. (2007). Matrigel coated polydimethylsiloxane based microfluidic devices for studying metastatic and non-metastatic cancer cell invasion and migration. Biomed. Microdevices *9*, 597–602.

Chawla, G., and Solares, S.D. (2011). Mapping of conservative and dissipative interactions in bimodal atomic force microscopy using open-loop and phase-locked-loop control of the higher eigenmode. Appl. Phys. Lett. *99*, 74103.

Chen, J. (2014). Nanobiomechanics of living cells: a review. Interface Focus *4*, 20130055.

Chester, S.A. (2012). A constitutive model for coupled fluid permeation and large viscoelastic deformation in polymeric gels. Soft Matter *8*, 8223.

Chien, S., Sung, K.L., Skalak, R., Usami, S., and Tözeren, A. (1978). Theoretical and experimental studies on viscoelastic properties of erythrocyte membrane. Biophys. J. *24*, 463–487.

Chiou, Y.-W., Lin, H.-K., Tang, M.-J., Lin, H.-H., and Yeh, M.-L. (2013). The Influence of Physical and Physiological Cues on Atomic Force Microscopy-Based Cell Stiffness Assessment. PLoS ONE *8*, e77384.

Chu, Y.-S., Thomas, W.A., Eder, O., Pincet, F., Perez, E., Thiery, J.P., and Dufour, S. (2004). Force measurements in E-cadherin–mediated cell doublets reveal rapid adhesion strengthened by actin cytoskeleton remodeling through Rac and Cdc42. J. Cell Biol. *167*, 1183–1194.

Churnside, A.B., Tung, R.C., and Killgore, J.P. (2015). Quantitative Contact Resonance Force Microscopy for Viscoelastic Measurement of Soft Materials at the Solid–Liquid Interface. Langmuir *31*, 11143–11149.

Chyasnavichyus, M., Young, S.L., and Tsukruk, V.V. (2015). Recent advances in micromechanical characterization of polymer, biomaterial, and cell surfaces with atomic force microscopy. Jpn. J. Appl. Phys. *54*, 08LA02.

Cicuta, P., and Donald, A.M. (2007). Microrheology: a review of the method and applications. Soft Matter *3*, 1449–1455.

Clark, A.G., and Vignjevic, D.M. (2015). Modes of cancer cell invasion and the role of the microenvironment. Curr. Opin. Cell Biol. *36*, 13–22.

Connell, L.E., and Helfman, D.M. (2006). Myosin light chain kinase plays a role in the regulation of epithelial cell survival. J. Cell Sci. *119*, 2269–2281.

Cooper, G.M. (2000). The Cell (Sinauer Associates).

Crick, F.H.C., and Hughes, A.F.W. (1950). The physical properties of cytoplasm. Exp. Cell Res. *1*, 37–80.

Crick, S.L., and Yin, F.C.-P. (2007). Assessing Micromechanical Properties of Cells with Atomic Force Microscopy: Importance of the Contact Point. Biomech. Model. Mechanobiol. *6*, 199–210.

Cuestas-Ayllon, C., Xiao, Q., Glidle, A., Riehle, M.O., M. Cooper, J., de la Fuente, J.M., and B. Yin, H. (2012). A Robust Lithographic Method for Multiplex Surface Pattering. Curr. Anal. Chem. *9*, 29–36.

Dao, M., Lim, C.T., and Suresh, S. (2003). Mechanics of the human red blood cell deformed by optical tweezers. J. Mech. Phys. Solids *51*, 2259–2280.

Decaestecker, C., Debeir, O., Van Ham, P., and Kiss, R. (2007). Can anti-migratory drugs be screened in vitro? A review of 2D and 3D assays for the quantitative analysis of cell migration. Med. Res. Rev. *27*, 149–176.

Desprat, N., Richert, A., Simeon, J., and Asnacios, A. (2005). Creep Function of a Single Living Cell. Biophys. J. *88*, 2224–2233.

DiMilla, P.A., Barbee, K., and Lauffenburger, D.A. (1991). Mathematical model for the effects of adhesion and mechanics on cell migration speed. Biophys. J. *60*, 15–37.

Discher, D.E., Mohandas, N., and Evans, E.A. (1994). Molecular maps of red cell deformation: hidden elasticity and in situ connectivity. Science *266*, 1032–1035.

Discher, D.E., Janmey, P., and Wang, Y. (2005). Tissue Cells Feel and Respond to the Stiffness of Their Substrate. Science *310*, 1139–1143.

Doyle, A.D., Wang, F.W., Matsumoto, K., and Yamada, K.M. (2009). One-dimensional topography underlies three-dimensional fibrillar cell migration. J. Cell Biol. *184*, 481–490.

Étienne, J., and Duperray, A. (2011). Initial Dynamics of Cell Spreading Are Governed by Dissipation in the Actin Cortex. Biophys. J. *101*, 611–621.

Ferry, J.D. (1980). Viscoelastic Properties of Polymers (John Wiley & Sons).

Friedbacher, G., and Fuchs, H. (2009). Classification of Scanning Probe Microscopies. Pure Appl. Chem. *71*, 1337–1357.

Friedl, P., and Gilmour, D. (2009). Collective cell migration in morphogenesis, regeneration and cancer. Nat. Rev. Mol. Cell Biol. *10*, 445–457.

Friedl, P., and Wolf, K. (2003). Tumour-cell invasion and migration: diversity and escape mechanisms. Nat. Rev. Cancer *3*, 362–374.

Fuard, D., Tzvetkova-Chevolleau, T., Decossas, S., Tracqui, P., and Schiavone, P. (2008). Optimization of Poly-di-methyl-siloxane (PDMS) Substrates for Studying Cellular Adhesion and Motility. Microelectron Eng *85*, 1289–1293.

Fung, Y.-C. (1993). Biomechanics: Mechanical Properties of Living Tissues (New York, NY: Springer New York).

Fusenig, N.E., Breitkreutz, D., Dzarlieva, R.T., Boukamp, P., Bohnert, A., and Tilgen, W. (1983). Growth and differentiation characteristics of transformed keratinocytes from mouse and human skin in vitro and in vivo. J. Invest. Dermatol. *81*, 168s–75s.

Gartland, A., Erler, J.T., and Cox, T.R. The role of lysyl oxidase, the extracellular matrix and the pre-metastatic niche in bone metastasis. J. Bone Oncol.

Goldmann, W.H., Galneder, R., Ludwig, M., Xu, W., Adamson, E.D., Wang, N., and Ezzell, R.M. (1998). Differences in Elasticity of Vinculin-Deficient F9 Cells Measured by Magnetometry and Atomic Force Microscopy. Exp. Cell Res. *239*, 235–242.

Good, N.E., Winget, G.D., Winter, W., Connolly, T.N., Izawa, S., and Singh, R.M.M. (1966). Hydrogen Ion Buffers for Biological Research. Biochemistry (Mosc.) *5*, 467–477.

Gossett, D.R., Tse, H.T.K., Lee, S.A., Ying, Y., Lindgren, A.G., Yang, O.O., Rao, J., Clark, A.T., and Carlo, D.D. (2012). Hydrodynamic stretching of single cells for large population mechanical phenotyping. Proc. Natl. Acad. Sci. *109*, 7630–7635.

Grant, C.A., Alfouzan, A., Gough, T., Twigg, P.C., and Coates, P.D. (2013). Nano-scale temperature dependent visco-elastic properties of polyethylene terephthalate (PET) using atomic force microscope (AFM). Micron *44*, 174–178.

Guck, J., Schinkinger, S., Lincoln, B., Wottawah, F., Ebert, S., Romeyke, M., Lenz, D., Erickson, H.M., Ananthakrishnan, R., Mitchell, D., et al. (2005). Optical Deformability as an Inherent Cell Marker for Testing Malignant Transformation and Metastatic Competence. Biophys. J. *88*, 3689–3698.

Guo, X., Bonin, K., Scarpinato, K., and Guthold, M. (2014). The effect of neighboring cells on the stiffness of cancerous and non-cancerous human mammary epithelial cells. New J. Phys. *16*, 105002.

H G Hansma, and Hoh,  and J.H. (1994). Biomolecular Imaging with the Atomic Force Microscope. Annu. Rev. Biophys. Biomol. Struct. *23*, 115–140.

Hall, A. (2009). The cytoskeleton and cancer. Cancer Metastasis Rev. *28*, 5–14.

Halldorsson, S., Lucumi, E., Gómez-Sjöberg, R., and Fleming, R.M.T. (2015). Advantages and challenges of microfluidic cell culture in polydimethylsiloxane devices. Biosens. Bioelectron. *63*, 218–231.

Hénon, S., Lenormand, G., Richert, A., and Gallet, F. (1999). A new determination of the shear modulus of the human erythrocyte membrane using optical tweezers. Biophys. J. *76*, 1145–1151.

Hiratsuka, S., Mizutani, Y., Toda, A., Fukushima, N., Kawahara, K., Tokumoto, H., and Okajima, T. (2009). Power-Law Stress and Creep Relaxations of Single Cells Measured by Colloidal Probe Atomic Force Microscopy. Jpn. J. Appl. Phys. *48*, 08JB17.

Hoffman, B.D., and Crocker, J.C. (2009). Cell Mechanics: Dissecting the Physical Responses of Cells to Force. Annu. Rev. Biomed. Eng. *11*, 259–288.

Hooper, S., Marshall, J.F., and Sahai, E. (2006). Tumor Cell Migration in Three Dimensions. B.-M. in Enzymology, ed. (Academic Press), pp. 625–643.

Huang, S., and Ingber, D.E. (2005). Cell tension, matrix mechanics, and cancer development. Cancer Cell *8*, 175–176.

Huang, Y., Agrawal, B., Sun, D., Kuo, J.S., and Williams, J.C. (2011). Microfluidics-based devices: New tools for studying cancer and cancer stem cell migration. Biomicrofluidics *5*.

Hulkower, K.I., and Herber, R.L. (2011). Cell Migration and Invasion Assays as Tools for Drug Discovery. Pharmaceutics *3*, 107–124.

Hung, W.-C., Chen, S.-H., Paul, C.D., Stroka, K.M., Lo, Y.-C., Yang, J.T., and Konstantopoulos, K. (2013). Distinct signaling mechanisms regulate migration in unconfined versus confined spaces. J. Cell Biol. *202*, 807–824.

Hutter, J.L., and Bechhoefer, J. (1993). Calibration of atomic-force microscope tips. Rev. Sci. Instrum. *64*, 1868–1873.

Irimia, D., and Toner, M. (2009). Spontaneous migration of cancer cells under conditions of mechanical confinement. Integr. Biol. Quant. Biosci. Nano Macro *1*, 506–512.

Itoh, K., Yoshioka, K., Akedo, H., Uehata, M., Ishizaki, T., and Narumiya, S. (1999). An essential part for Rho–associated kinase in the transcellular invasion of tumor cells. Nat. Med. *5*, 221–225.

Iyer, S., Woodworth, C.D., Gaikwad, R.M., Kievsky, Y.Y., and Sokolov, I. (2009). Towards nonspecific detection of malignant cervical cells with fluorescent silica beads**. Small Weinh. Bergstr. Ger. *5*, 2277–2284.

Jaishankar, A., and McKinley, G.H. (2013). Power-law rheology in the bulk and at the interface: quasi-properties and fractional constitutive equations. Proc R Soc A *469*, 20120284.

Jonas, O., Mierke, C.T., and Käs, J.A. (2011). Invasive cancer cell lines exhibit biomechanical properties that are distinct from their noninvasive counterparts. Soft Matter *7*, 11488–11495.

Jones, W.R., Ping Ting-Beall, H., Lee, G.M., Kelley, S.S., Hochmuth, R.M., and Guilak, F. (1999). Alterations in the Young’s modulus and volumetric properties of chondrocytes isolated from normal and osteoarthritic human cartilage. J. Biomech. *32*, 119–127.

Kamm, R., Lammerding, J., and Mofrad, M. (2010). Cellular Nanomechanics. In Springer Handbook of Nanotechnology, P.B. Bhushan, ed. (Springer Berlin Heidelberg), pp. 1171–1200.

Kaneko, K., Satoh, K., Masamune, A., Satoh, A., and Shimosegawa, T. (2002). Expression of ROCK-1 in human pancreatic cancer: its down-regulation by morpholino oligo antisense can reduce the migration of pancreatic cancer cells in vitro. Pancreas *24*, 251–257.

Katira, P., Bonnecaze, R.T., and Zaman, M.H. (2013). Modeling the Mechanics of Cancer: Effect of Changes in Cellular and Extra-Cellular Mechanical Properties. Front. Oncol. *3*.

Katt, M.E., Placone, A.L., Wong, A.D., Xu, Z.S., and Searson, P.C. (2016). In Vitro Tumor Models: Advantages, Disadvantages, Variables, and Selecting the Right Platform. Front. Bioeng. Biotechnol. *4*.

Keenan, T.M., and Folch, A. (2007). Biomolecular gradients in cell culture systems. Lab. Chip *8*, 34–57.

Ketene, A.N., Schmelz, E.M., Roberts, P.C., and Agah, M. (2012). The effects of cancer progression on the viscoelasticity of ovarian cell cytoskeleton structures. Nanomedicine Nanotechnol. Biol. Med. *8*, 93–102.

Khan, Z.S., and Vanapalli, S.A. (2013). Probing the mechanical properties of brain cancer cells using a microfluidic cell squeezer device. Biomicrofluidics *7*.

Kidoaki, S., and Matsuda, T. (2008). Microelastic gradient gelatinous gels to induce cellular mechanotaxis. J. Biotechnol. *133*, 225–230.

Kole, T.P., Tseng, Y., Huang, L., Katz, J.L., and Wirtz, D. (2004). Rho Kinase Regulates the Intracellular Micromechanical Response of Adherent Cells to Rho Activation. Mol. Biol. Cell *15*, 3475–3484.

Kollmannsberger, P., and Fabry, B. (2009). Active soft glassy rheology of adherent cells. Soft Matter *5*, 1771.

Kollmannsberger, P., and Fabry, B. (2011). Linear and Nonlinear Rheology of Living Cells. Annu. Rev. Mater. Res. *41*, 75–97.

Kollmannsberger, P., Mierke, C.T., and Fabry, B. (2011). Nonlinear viscoelasticity of adherent cells is controlled by cytoskeletal tension. Soft Matter *7*, 3127–3132.

Kramer, N., Walzl, A., Unger, C., Rosner, M., Krupitza, G., Hengstschläger, M., and Dolznig, H. (2013). In vitro cell migration and invasion assays. Mutat. Res. Mutat. Res. *752*, 10–24.

Kraning-Rush, C.M., Califano, J.P., and Reinhart-King, C.A. (2012). Cellular Traction Stresses Increase with Increasing Metastatic Potential. PLoS ONE *7*.

Kumar, S., and Weaver, V.M. (2009). Mechanics, malignancy, and metastasis: The force journey of a tumor cell. Cancer Metastasis Rev. *28*, 113–127.

Kümper, S., Mardakheh, F.K., McCarthy, A., Yeo, M., Stamp, G.W., Paul, A., Worboys, J., Sadok, A., Jørgensen, C., Guichard, S., et al. (2016). Rho-associated kinase (ROCK) function is essential for cell cycle progression, senescence and tumorigenesis. eLife *5*, e12203.

Kuznetsova, T.G., Starodubtseva, M.N., Yegorenkov, N.I., Chizhik, S.A., and Zhdanov, R.I. (2007). Atomic force microscopy probing of cell elasticity. Micron *38*, 824–833.

Lämmermann, T., Bader, B.L., Monkley, S.J., Worbs, T., Wedlich-Söldner, R., Hirsch, K., Keller, M., Förster, R., Critchley, D.R., Fässler, R., et al. (2008). Rapid leukocyte migration by integrin-independent flowing and squeezing. Nature *453*, 51–55.

Landau, L.D., Kosevich, A.M., Pitaevskii, L.P., and Lifshitz, E.M. (1986). Theory of elasticity.

Lange, J.R., and Fabry, B. (2013). Cell and tissue mechanics in cell migration. Exp. Cell Res. *319*, 2418–2423.

Lanza, M., Porti, M., Nafría, M., Aymerich, X., Whittaker, E., and Hamilton, B. (2010). Note: Electrical resolution during conductive atomic force microscopy measurements under different environmental conditions and contact forces. Rev. Sci. Instrum. *81*, 106110.

Lau, A.W.C., Hoffman, B.D., Davies, A., Crocker, J.C., and Lubensky, T.C. (2003). Microrheology, Stress Fluctuations, and Active Behavior of Living Cells. Phys. Rev. Lett. *91*, 198101.

Lautscham, L.A., Kämmerer, C., Lange, J.R., Kolb, T., Mark, C., Schilling, A., Strissel, P.L., Strick, R., Gluth, C., Rowat, A.C., et al. (2015). Migration in Confined

3D Environments Is Determined by a Combination of Adhesiveness, Nuclear Volume, Contractility, and Cell Stiffness. Biophys. J. *109*, 900–913.

Lee, Y.J. (2011). Local Rheology of Human Neutrophils Investigated Using Atomic Force Microscopy. Int. J. Biol. Sci. 102–111.

Lee, M.-H., Wu, P.-H., Staunton, J.R., Ros, R., Longmore, G.D., and Wirtz, D. (2012). Mismatch in Mechanical and Adhesive Properties Induces Pulsating Cancer Cell Migration in Epithelial Monolayer. Biophys. J. *102*, 2731–2741.

Lekka, M., Laidler, P., Gil, D., Lekki, J., Stachura, Z., and Hrynkiewicz, A.Z. (1999). Elasticity of normal and cancerous human bladder cells studied by scanning force microscopy. Eur. Biophys. J. *28*, 312–316.

Lekka, M., Pogoda, K., Gostek, J., Klymenko, O., Prauzner-Bechcicki, S., Wiltowska-Zuber, J., Jaczewska, J., Lekki, J., and Stachura, Z. (2012). Cancer cell recognition – Mechanical phenotype. Micron *43*, 1259–1266.

Li, Q.S., Lee, G.Y.H., Ong, C.N., and Lim, C.T. (2008). AFM indentation study of breast cancer cells. Biochem. Biophys. Res. Commun. *374*, 609–613.

Lieber, S.C., Aubry, N., Pain, J., Diaz, G., Kim, S.-J., and Vatner, S.F. (2004). Aging increases stiffness of cardiac myocytes measured by atomic force microscopy nanoindentation. Am. J. Physiol. - Heart Circ. Physiol. *287*, H645–H651.

Lieleg, O., Claessens, M.M. a. E., Luan, Y., and Bausch, A.R. (2008). Transient binding and dissipation in cross-linked actin networks. Phys. Rev. Lett. *101*, 108101.

Lim, C.T., Zhou, E.H., and Quek, S.T. (2006). Mechanical models for living cells—a review. J. Biomech. *39*, 195–216.

Lim, S.-O., Kim, H., and Jung, G. (2010). p53 inhibits tumor cell invasion via the degradation of snail protein in hepatocellular carcinoma. FEBS Lett. *584*, 2231–2236.

Lin, D.C., Dimitriadis, E.K., and Horkay, F. (2006). Robust Strategies for Automated AFM Force Curve Analysis—I. Non-adhesive Indentation of Soft, Inhomogeneous Materials. J. Biomech. Eng. *129*, 430–440.

Liu, H., Wen, J., Xiao, Y., Liu, J., Hopyan, S., Radisic, M., Simmons, C.A., and Sun, Y. (2014). In Situ Mechanical Characterization of the Cell Nucleus by Atomic Force Microscopy. ACS Nano *8*, 3821–3828.

Lo, C.-M., Wang, H.-B., Dembo, M., and Wang, Y. (2000). Cell Movement Is Guided by the Rigidity of the Substrate. Biophys. J. *79*, 144–152.

Lochhead, P.A., Wickman, G., Mezna, M., and Olson, M.F. (2010). Activating ROCK1 somatic mutations in human cancer. Oncogene *29*, 2591–2598.

López-Guerra, E.A., and Solares, S.D. (2014). Modeling viscoelasticity through spring–dashpot models in intermittent-contact atomic force microscopy. Beilstein J. Nanotechnol. *5*, 2149–2163.

Lulevich, V., Shih, Y.-P., Lo, S.H., and Liu, G. (2009). Cell tracing dyes significantly change single cell mechanics. J. Phys. Chem. B *113*, 6511–6519.

Mahaffy, R.E., Park, S., Gerde, E., Käs, J., and Shih, C.K. (2004). Quantitative Analysis of the Viscoelastic Properties of Thin Regions of Fibroblasts Using Atomic Force Microscopy. Biophys. J. *86*, 1777–1793.

Mak, M., Reinhart-King, C.A., and Erickson, D. (2011). Microfabricated Physical Spatial Gradients for Investigating Cell Migration and Invasion Dynamics. PLoS ONE *6*, e20825.

Mak, M., Reinhart-King, C.A., and Erickson, D. (2013). Elucidating mechanical transition effects of invading cancer cells with a subnucleus-scaled microfluidic serial dimensional modulation device. Lab. Chip *13*, 340–348.

Martens, J.C., and Radmacher, M. (2008). Softening of the actin cytoskeleton by inhibition of myosin II. Pflüg. Arch. - Eur. J. Physiol. *456*, 95–100.

Mason, T.G., Ganesan, K., van Zanten, J.H., Wirtz, D., and Kuo, S.C. (1997). Particle Tracking Microrheology of Complex Fluids. Phys. Rev. Lett. *79*, 3282–3285.

McGregor, A.L., Hsia, C.-R., and Lammerding, J. (2016). Squish and squeeze — the nucleus as a physical barrier during migration in confined environments. Curr. Opin. Cell Biol. *40*, 32–40.

McPhee, G., Dalby, M.J., Riehle, M., and Yin, H. (2010). Can common adhesion molecules and microtopography affect cellular elasticity? A combined atomic force microscopy and optical study. Med. Biol. Eng. Comput. *48*, 1043–1053.

Mertz, A.F., Banerjee, S., Che, Y., German, G.K., Xu, Y., Hyland, C., Marchetti, M.C., Horsley, V., and Dufresne, E.R. (2012). Scaling of Traction Forces with the Size of Cohesive Cell Colonies. Phys. Rev. Lett. *108*, 198101.

Meyers, M.A., and Chawla, K.K. (1999). Mechanical behavior of materials (Prentice-Hall, Upper Saddle River, NJ).

Mitchison, J.M., and Swann, M.M. (1954). The Mechanical Properties of the cell Surface. J. Exp. Biol. *31*, 461–472.

Mitchison, T.J., and Cramer, L.P. (1996). Actin-Based Cell Motility and Cell Locomotion. Cell *84*, 371–379.

Mitrossilis, D., Fouchard, J., Pereira, D., Postic, F., Richert, A., Saint-Jean, M., and Asnacios, A. (2010). Real-time single-cell response to stiffness. Proc. Natl. Acad. Sci. U. S. A. *107*, 16518–16523.

Moeendarbary, E., and Harris, A.R. (2014). Cell mechanics: principles, practices, and prospects. Wiley Interdiscip. Rev. Syst. Biol. Med. *6*, 371–388.

Moreno-Flores, S., Benitez, R., Vivanco, M. dM, and Toca-Herrera, J.L. (2010). Stress relaxation and creep on living cells with the atomic force microscope: a means to calculate elastic moduli and viscosities of cell components. Nanotechnology *21*, 445101.

Morgan-Fisher, M., Wewer, U.M., and Yoneda, A. (2013). Regulation of ROCK Activity in Cancer. J. Histochem. Cytochem. *61*, 185–198.

Morton, J.P., Timpson, P., Karim, S.A., Ridgway, R.A., Athineos, D., Doyle, B., Jamieson, N.B., Oien, K.A., Lowy, A.M., Brunton, V.G., et al. (2010). Mutant p53 drives metastasis and overcomes growth arrest/senescence in pancreatic cancer. Proc. Natl. Acad. Sci. *107*, 246–251.

Mueller-Klieser, W. (1987). Multicellular spheroids. A review on cellular aggregates in cancer research. J. Cancer Res. Clin. Oncol. *113*, 101–122.

Nasrollahi, S., and Pathak, A. (2016). Topographic confinement of epithelial clusters induces epithelial-to-mesenchymal transition in compliant matrices. Sci. Rep. *6*.

Neuman, K.C., Chadd, E.H., Liou, G.F., Bergman, K., and Block, S.M. (1999). Characterization of Photodamage to Escherichia coli in Optical Traps. Biophys. J. *77*, 2856–2863.

Niggemann, B., Drell IV, T.L., Joseph, J., Weidt, C., Lang, K., Zaenker, K.S., and Entschladen, F. (2004). Tumor cell locomotion: differential dynamics of spontaneous and induced migration in a 3D collagen matrix. Exp. Cell Res. *298*, 178–187.

Oh, M.-J., Kuhr, F., Byfield, F., and Levitan, I. (2012). Micropipette Aspiration of Substrate-attached Cells to Estimate Cell Stiffness. J. Vis. Exp.

Okajima, T., Tanaka, M., Tsukiyama, S., Kadowaki, T., Yamamoto, S., Shimomura, M., and Tokumoto, H. (2007). Stress relaxation of HepG2 cells measured by atomic force microscopy. Nanotechnology *18*, 84010.

Paňková, K., Rösel, D., Novotný, M., and Brábek, J. (2010). The molecular mechanisms of transition between mesenchymal and amoeboid invasiveness in tumor cells. Cell. Mol. Life Sci. *67*, 63–71.

Paredes, J., Albergaria, A., Oliveira, J.T., Jerónimo, C., Milanezi, F., and Schmitt, F.C. (2005). P-cadherin overexpression is an indicator of clinical outcome in invasive breast carcinomas and is associated with CDH3 promoter hypomethylation. Clin. Cancer Res. Off. J. Am. Assoc. Cancer Res. *11*, 5869–5877.

Parri, M., and Chiarugi, P. (2010). Rac and Rho GTPases in cancer cell motility control. Cell Commun. Signal. CCS *8*, 23.

Pelling, A.E., Nicholls, B.M., Silberberg, Y.R., and Horton, M.A. (2007). Approaches for Investigating Mechanobiological Dynamics in Living Cells with Fluorescence and Atomic Force Microscopies. In Modern Research and Educational Topics in Microscopy, (Formatex), pp. 3–10.

Pietuch, A., and Janshoff, A. (2013). Mechanics of spreading cells probed by atomic force microscopy. Open Biol. *3*, 130084.

Popow-Woźniak, A., Mazur, A.J., Mannherz, H.G., Malicka-Błaszkiewicz, M., and Nowak, D. (2012). Cofilin overexpression affects actin cytoskeleton organization and migration of human colon adenocarcinoma cells. Histochem. Cell Biol. *138*, 725–736.

Pravincumar, P., Bader, D.L., and Knight, M.M. (2012). Viscoelastic Cell Mechanics and Actin Remodelling Are Dependent on the Rate of Applied Pressure. PLOS ONE *7*, e43938.

Puttock, M.J., and Thwaite, E.G. (1969). Elastic Compression of Spheres and Cylinders at Point and Line Contact (Melbourne: Commonwealth Scientific and Industrial Research Organization).

Radmacher, M., Tillmann, R.W., and Gaub, H.E. (1993). Imaging viscoelasticity by force modulation with the atomic force microscope. Biophys. J. *64*, 735–742.

Raftopoulou, M., and Hall, A. (2004). Cell migration: Rho GTPases lead the way. Dev. Biol. *265*, 23–32.

Rao, S.M.N., Tata, U., Lin, V.K., and Chiao, J.-C. (2014). The Migration of Cancer Cells in Gradually Varying Chemical Gradients and Mechanical Constraints. Micromachines *5*, 13–26.

Rath, N., and Olson, M.F. (2012). Rho-associated kinases in tumorigenesis: re-considering ROCK inhibition for cancer therapy. EMBO Rep. *13*, 900–908.

Rebelo, L.M., Sousa, J.S. de, Filho, J.M., and Radmacher, M. (2013). Comparison of the viscoelastic properties of cells from different kidney cancer phenotypes measured with atomic force microscopy. Nanotechnology *24*, 55102.

Ribeiro, A.S., Albergaria, A., Sousa, B., Correia, A.L., Bracke, M., Seruca, R., Schmitt, F.C., and Paredes, J. (2010). Extracellular cleavage and shedding of P-cadherin: a mechanism underlying the invasive behaviour of breast cancer cells. Oncogene *29*, 392–402.

Riento, K., and Ridley, A.J. (2003). ROCKs: multifunctional kinases in cell behaviour. Nat. Rev. Mol. Cell Biol. *4*, 446–456.

Roca-Cusachs, P., Almendros, I., Sunyer, R., Gavara, N., Farré, R., and Navajas, D. (2006). Rheology of Passive and Adhesion-Activated Neutrophils Probed by Atomic Force Microscopy. Biophys. J. *91*, 3508–3518.

Rodriguez-Menocal, L., Salgado, M., Ford, D., and Van Badiavas, E. (2012). Stimulation of Skin and Wound Fibroblast Migration by Mesenchymal Stem Cells Derived from Normal Donors and Chronic Wound Patients. Stem Cells Transl. Med. *1*, 221–229.

Rolli, C.G., Seufferlein, T., Kemkemer, R., and Spatz, J.P. (2010). Impact of Tumor Cell Cytoskeleton Organization on Invasiveness and Migration: A Microchannel-Based Approach. PLoS ONE *5*.

Rother, J., Nöding, H., Mey, I., and Janshoff, A. (2014). Atomic force microscopy-based microrheology reveals significant differences in the viscoelastic response between malign and benign cell lines. Open Biol. *4*.

Sahai, E., and Marshall, C.J. (2003). Differing modes of tumour cell invasion have distinct requirements for Rho/ROCK signalling and extracellular proteolysis. Nat. Cell Biol. *5*, 711–719.

Saito, K., Oku, T., Ata, N., Miyashiro, H., Hattori, M., and Saiki, I. (1997). A Modified and Convenient Method for Assessing Tumor Cell Invasion and Migration and Its Application to Screening for Inhibitors. Biol. Pharm. Bull. *20*, 345–348.

Samuel, M.S., Lopez, J.I., McGhee, E.J., Croft, D.R., Strachan, D., Timpson, P., Munro, J., Schröder, E., Zhou, J., Brunton, V.G., et al. (2011). Actomyosin-Mediated Cellular Tension Drives Increased Tissue Stiffness and β-Catenin Activation to Induce Epidermal Hyperplasia and Tumor Growth. Cancer Cell *19*, 776–791.

Sant, S., Hancock, M.J., Donnelly, J.P., Iyer, D., and Khademhosseini, A. (2010). Biomimetic gradient hydrogels for tissue engineering. Can. J. Chem. Eng. *88*, 899–911.

Scarpa, A., Capelli, P., Mukai, K., Zamboni, G., Oda, T., Iacono, C., and Hirohashi, S. (1993). Pancreatic adenocarcinomas frequently show p53 gene mutations. Am. J. Pathol. *142*, 1534–1543.

Scheffer, L., Bitler, A., Ben-Jacob, E., and Korenstein, R. (2001). Atomic force pulling: probing the local elasticity of the cell membrane. Eur. Biophys. J. EBJ *30*, 83–90.

Schmid-Schönbein, G.W., Sung, K.L., Tözeren, H., Skalak, R., and Chien, S. (1981). Passive mechanical properties of human leukocytes. Biophys. J. *36*, 243–256.

Shi, X., and Zhao, Y.-P. (2004). Comparison of various adhesion contact theories and the influence of dimensionless load parameter. J. Adhes. Sci. Technol. *18*, 55–68.

Shin, D., and Athanasiou, K. (1999). Cytoindentation for obtaining cell biomechanical properties. J. Orthop. Res. Off. Publ. Orthop. Res. Soc. *17*, 880–890.

Sokolov, I. (2007). Atomic Force Microscopy in Cancer Cell Research. In Cancer Nanotechnology – Nanomaterials for Cancer Diagnosis and Therapy, (American Scientific Publishers' Inc.), pp. 43–59.

Solares, S.D. (2014). Probing viscoelastic surfaces with bimodal tapping-mode atomic force microscopy: Underlying physics and observables for a standard linear solid model. Beilstein J. Nanotechnol. *5*, 1649–1663.

Sraj, I., Eggleton, C.D., Jimenez, R., Hoover, E., Squier, J., Chichester, J., and Marr, D.W.M. (2010). Cell deformation cytometry using diode-bar optical stretchers. J. Biomed. Opt. *15*, 47010-047010–047017.

Stroka, K.M., and Aranda-Espinoza, H. (2010). Effects of Morphology vs. Cell–Cell Interactions on Endothelial Cell Stiffness. Cell. Mol. Bioeng. *4*, 9–27.

Sunyer, R., Trepat, X., Fredberg, J.J., Farré, R., and Navajas, D. (2009). The temperature dependence of cell mechanics measured by atomic force microscopy. Phys. Biol. *6*, 25009.

Suresh, S. (2007). Biomechanics and biophysics of cancer cells. Acta Biomater. *3*, 413–438.

Tassieri, M. (2015). Linear microrheology with optical tweezers of living cells "is not an option"! Soft Matter *11*, 5792–5798.

Tassieri, M., Evans, R.M.L., Warren, R.L., Bailey, N.J., and Cooper, J.M. (2012). Microrheology with optical tweezers: data analysis. New J. Phys. *14*, 115032.

Tassieri, M., Laurati, M., Curtis, D.J., Auhl, D.W., Coppola, S., Scalfati, A., Hawkins, K., Williams, P.R., and Cooper, J.M. (2016). i-Rheo: Measuring the materials' linear viscoelastic properties "in a step"! J. Rheol. 1978-Present *60*, 649–660.

Taylor, A.C. (1962). Responses of cells to pH changes in the medium. J. Cell Biol. *15*, 201–209.

Tee, S.-Y., Fu, J., Chen, C.S., and Janmey, P.A. (2011). Cell Shape and Substrate Rigidity Both Regulate Cell Stiffness. Biophys. J. *100*, L25–L27.

Timpson, P., Mcghee, E.J., Erami, Z., Nobis, M., Quinn, J.A., Edward, M., and Anderson, K.I. (2011a). Organotypic Collagen I Assay: A Malleable Platform to Assess Cell Behaviour in a 3-Dimensional Context. J. Vis. Exp. JoVE.

Timpson, P., McGhee, E.J., Morton, J.P., Kriegsheim, A. von, Schwarz, J.P., Karim, S.A., Doyle, B., Quinn, J.A., Carragher, N.O., Edward, M., et al. (2011b). Spatial Regulation of RhoA Activity during Pancreatic Cancer Cell Invasion Driven by Mutant p53. Cancer Res. *71*, 747–757.

Tong, Z., Balzer, E.M., Dallas, M.R., Hung, W.-C., Stebe, K.J., and Konstantopoulos, K. (2012). Chemotaxis of Cell Populations through Confined Spaces at Single-Cell Resolution. PLOS ONE *7*, e29211.

Trepat, X., Chen, Z., and Jacobson, K. (2012). Cell Migration. Compr. Physiol. *2*, 2369–2392.

Tripathy, S., and Berger, E.J. (2009). Measuring Viscoelasticity of Soft Samples Using Atomic Force Microscopy. J. Biomech. Eng. *131*, 094507–094507.

Tu, Y.-O., and Gazis, D.C. (1964). The Contact Problem of a Plate Pressed Between Two Spheres. J. Appl. Mech. *31*, 659–666.

Vadillo-Rodríguez, V., and Dutcher, J.R. (2011). Viscoelasticity of the bacterial cell envelope. Soft Matter *7*, 4101.

Vadillo-Rodriguez, V., Beveridge, T.J., and Dutcher, J.R. (2008). Surface Viscoelasticity of Individual Gram-Negative Bacterial Cells Measured Using Atomic Force Microscopy. J. Bacteriol. *190*, 4225–4232.

Vahabi, S., Nazemi Salman, B., and Javanmard, A. (2013). Atomic Force Microscopy Application in Biological Research: A Review Study. Iran. J. Med. Sci. *38*, 76–83.

Vincent, J. (2012). Structural Biomaterials: Third Edition (Princeton University Press).

Vinci, M., Box, C., and Eccles, S.A. (2015). Three-Dimensional (3D) Tumor Spheroid Invasion Assay. J. Vis. Exp. JoVE.

Wang, N., Butler, J.P., and Ingber, D.E. (1993). Mechanotransduction across the cell surface and through the cytoskeleton. Science *260*, 1124–1127.

Wang, N., Tolić-Nørrelykke, I.M., Chen, J., Mijailovich, S.M., Butler, J.P., Fredberg, J.J., and Stamenović, D. (2002). Cell prestress. I. Stiffness and prestress are closely associated in adherent contractile cells. Am. J. Physiol. - Cell Physiol. *282*, C606–C616.

Weisenhorn, A.L., Khorsandi, M., Kasas, S., Gotzos, V., and Butt, H.-J. (1993). Deformation and height anomaly of soft surfaces studied with an AFM. Nanotechnology *4*, 106.

Wilhelm, K.R., Roan, E., Ghosh, M.C., Parthasarathi, K., and Waters, C.M. (2014). Hyperoxia Increases the Elastic Modulus of Alveolar Epithelial Cells Through Rho Kinase. FEBS J. *281*, 957–969.

Wirtz, D. (2009). Particle-Tracking Microrheology of Living Cells: Principles and Applications. Annu. Rev. Biophys. *38*, 301–326.

Wolf, K., Mazo, I., Leung, H., Engelke, K., von Andrian, U.H., Deryugina, E.I., Strongin, A.Y., Bröcker, E.-B., and Friedl, P. (2003). Compensation mechanism in tumor cell migration. J. Cell Biol. *160*, 267–277.

Wong, J.Y., Velasco, A., Rajagopalan, P., and Pham, Q. (2003). Directed Movement of Vascular Smooth Muscle Cells on Gradient-Compliant Hydrogels. Langmuir *19*, 1908–1913.

Wu, H.W., Kuhn, T., and Moy, V.T. (1998). Mechanical properties of L929 cells measured by atomic force microscopy: Effects of anticytoskeletal drugs and membrane crosslinking. Scanning *20*, 389–397.

Xu, J., Palmer, A., and Wirtz, D. (1998). Rheology and Microrheology of Semiflexible Polymer Solutions: Actin Filament Networks. Macromolecules *31*, 6486–6492.

Xu, X.-T., Song, Q.-B., Yao, Y., Ruan, P., and Tao, Z.-Z. (2012). Inhibition of RhoA/ROCK signaling pathway promotes the apoptosis of gastric cancer cells. Hepatogastroenterology. *59*, 2523–2526.

Yallapu, M.M., Katti, K.S., Katti, D.R., Mishra, S.R., Khan, S., Jaggi, M., and Chauhan, S.C. (2015). The Roles of Cellular Nanomechanics in Cancer. Med. Res. Rev. *35*, 198–223.

Yang, S., and Kim, H.-M. (2014). ROCK Inhibition Activates MCF-7 Cells. PLOS ONE *9*, e88489.

Yoneda, A., Multhaupt, H.A.B., and Couchman, J.R. (2005). The Rho kinases I and II regulate different aspects of myosin II activity. J. Cell Biol. *170*, 443–453.

Yuya, P.A., Hurley, D.C., and Turner, J.A. (2008). Contact-resonance atomic force microscopy for viscoelasticity. J. Appl. Phys. *104*, 74916.

Zhang, L., Luo, J., Wan, P., Wu, J., Laski, F., and Chen, J. (2011a). Regulation of cofilin phosphorylation and asymmetry in collective cell migration during morphogenesis. Development *138*, 455–464.

Zhang, X., Li, C., Gao, H., Nabeka, H., Shimokawa, T., Wakisaka, H., Matsuda, S., and Kobayashi, N. (2011b). Rho kinase inhibitors stimulate the migration of human cultured osteoblastic cells by regulating actomyosin activity. Cell. Mol. Biol. Lett. *16*, 279–295.

Zhao, M., Srinivasan, C., Burgess, D.J., and Huey, B.D. (2006). Rate- and depth-dependent nanomechanical behavior of individual living Chinese hamster ovary cells probed by atomic force microscopy. J. Mater. Res. *21*, 1906–1912.

Zhu, C., Bao, G., and Wang, N. (2000). CELL MECHANICS: Mechanical Response, Cell Adhesion, and Molecular Deformation. Annu. Rev. Biomed. Eng. *2*, 189–226.

Ziemann, F., Rädler, J., and Sackmann, E. (1994). Local measurements of viscoelastic moduli of entangled actin networks using an oscillating magnetic bead micro-rheometer. Biophys. J. *66*, 2210–2216.